ETH Zürich Series in Electromagnetic Fields, Vol. 7

Andrej Titus Marculescu

Semiconductor Optical Amplifiers
Modeling, Signal Regeneration and Conversion

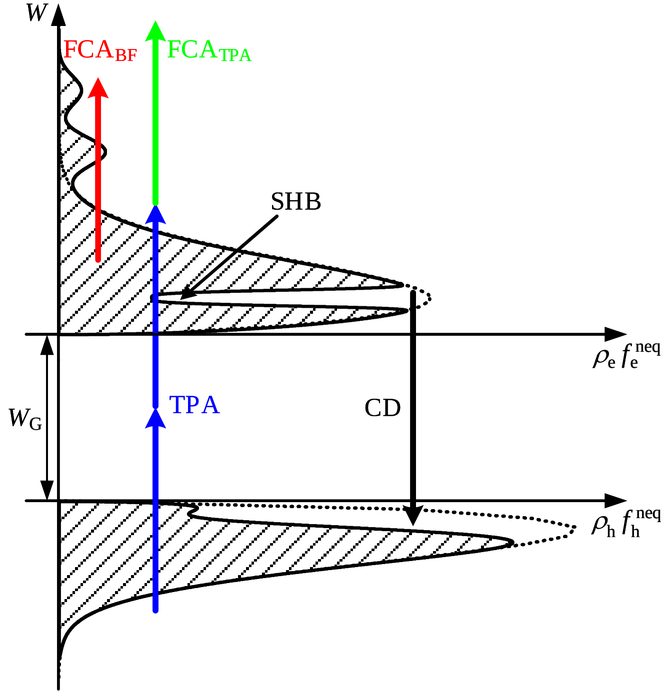

Diss.-No. ETH 25051

ETH zürich

DISS. ETH NO. 25051

SEMICONDUCTOR OPTICAL AMPLIFIERS:
MODELING, SIGNAL REGENERATION AND CONVERSION

A thesis submitted to attain the degree of
DOCTOR OF SCIENCES of ETH ZURICH

(Dr. sc. ETH Zurich)

presented by

ANDREJ TITUS MARCULESCU
Dipl.-Ing., Universität Karlsruhe
born on 20.06.1978
citizen of Germany

accepted on the recommendation of

Prof. Dr. Juerg Leuthold
Prof. Dr.-Ing. Dr. h. c. Wolfgang Freude
Prof. Dr. Andreas Schenk

Zurich, Switzerland, 22.03.2018

Contents

Preface

Technological innovations in single mode optical fibers and semiconductor devices, advance the research in the field of optical communications. Millions of kilometers of single mode fibers have been deployed throughout the world. The exponential growth of the internet traffic, voice communication and video-on-demand services require more and more network capacity.

It is expected that the totally available bandwidth of single mode fibers, will be exploited by new technologies operating in time division multiplexing (TDM), wavelength division multiplexing (WDM) and orthogonal frequency division multiplexing (OFDM). In recent years, we have witnessed the introduction of many new technologies for optical transmission, helping to expand the capacity of global telecommunication networks.

In order to achieve a spectrally efficient high capacity transmission, many advanced all-optical signal processing functions have to be realized, such as all-optical switching, wavelength conversion, logic gates, flip-flop memories, the use of different modulation formats, signal regeneration, etc.

All-optical signal processing functions are usually implemented by exploiting nonlinear optical effects in a device. In all-optical signal processing systems, which aim at applications in telecommunication networks, the nonlinearities are mainly based on optical fibers, semiconductor materials (InGaAsP/GaAs) and solid-state crystals, such as lithium niobate ($LiNbO_3$). The semiconductor material is attractive in all-optical signal processing systems, especially in semiconductor optical amplifier (SOA) based devices. SOAs have several striking advantages: First, the optical power of the input signal can be low due to inherent amplification in the device, leading to high power efficiency. Second, the device dimensions are small compared to devices based on other materials, and third they have the potential to be integrated with other photonic devices. SOAs can be integrated monolithically with laser diodes, optical modulators, photodiodes and passive waveguides including multi-mode-interference couplers. Integrated devices can provide more complex functionalities, for example all-optical wavelength converters, all-optical switches, wavelength and signal regenerators. Lastly, the wide gain bandwidth and the flexible choice of operation wavelengths are another attractive feature offered by SOAs.

A drawback of SOA-based signal processing systems limiting the maximum usable bit rate is the long carrier recovery time of the SOA device which leads to a significant patterning effect in the signal. This challenge can be met by optical filtering schemes, allowing to achieve high operation bit rates resulting in patterning-free (error-free and pattern independent) output signals.

In transparent optical networks, wavelength blocking can occur when two signals at identical wavelengths need to be transmitted in the same fiber. Wavelength conversion helps changing the wavelength of one of the two signals. SOA-based wavelength and modulation format converters utilize optical filtering techniques on the converted signal. This method can be systematically employed when – based on the knowledge of the full refractive index dynamics – it is possible to assign different spectral components of the probe light to certain physical effects in the SOA.

In this thesis several solutions to the challenges of wavelength conversion at high bit rates, signal quality improvement, and modulation format conversion are described and experimentally investigated. For instance, an experiment based on a single SOA followed by a filter for patterning-free wavelength conversion at 40 Gbit/s with simultaneous change of return-to-zero (RZ) to vestigial sideband (VSB) and carrier-suppressed-return-to-zero (CSRZ) modulation formats, and its regenerative properties has been realized. Advanced modulation formats, especially VSB and CSRZ, show good tolerance to linear and nonlinear impairments that accumulate along fiber-optic transmission lines. These formats are good candidates for ultra-long-haul transmission since they offer the possibility to make better use of the spectral bandwidth of the fiber, allowing to reduce the channel spacing and to increase therefore the transmission capacity. Also, the inter-symbol interference (ISI) is reduced due to a progressive phase shift (PPS) for both VSB (PPS= $\pi/2$) and CSRZ (PPS= π) formats.

This thesis is organized as follows:

In chapter 1 provides a short overview on nonlinear parametric and non-parametric processes in nonlinear materials.

Chapter 2 presents the gain and the refractive index nonlinearities in the SOA.

Chapter 3 describes the physical effects in an SOA arising from its interaction with short optical pulses. The resulting time evolution of the SOA gain and refractive index is depicted.

Chapter 4 focuses on the analysis of the spectral signature of nonlinear effects in an SOA. Starting with an analytical model of the gain and refractive index dynamics, one aims to fit calculated spectra to measured ones for the output pump pulse and for the probe light. Besides describing the known SOA gain-saturating mechanisms, the model introduces for the first time a delayed absorption effect, termed as two-photon induced free carrier absorption. This effect was indicated from a frequency resolved electro-absorption gating (FREAG) modulator measurement on an output pump pulse. The nonlinearity parameters of the model have been determined by fitting the calculated spectra for the output pump and probe signals to the measured spectra. We have further investigated the dependency of the pump and the probe light spectra with respect to the operating parameters in order to optimally apply the optical filtering for selecting or suppressing certain spectral components. We make use of this spectral shaping in subsequent chapters. We conclude 4 by showing how optical filtering serves to establish the operating parameters in logic gates.

In chapter 5, SOA-based wavelength conversion and regeneration using optical filtering techniques are presented. We examine the changes in gain and refractive index of the SOA, and the polarization-rotation and the chirp (the time dependence of the instantaneous frequency) of the probe light due to incomplete carrier recovery between consecutive mark bits in saturated SOAs. Conversion techniques based upon above-mentioned changes are then reported. We have used optical filtering techniques suitably designed for the chirp dynamics of the probe light. Since the red chirp is decreasing and the blue one is increasing with a growing degree of saturation of the SOA, the wavelength converted signal after the amplifier can be considerably improved by a filter of appropriate shape. Based upon the frequency-to-amplitude conversion on the filter slope, we have obtained a patterning-free converted non-inverted signal at 40 Gbit/s with a red-shifted optical filter (RSOF). By using a specially designed filter system, named pulse reformatting optical filter (PROF), we were able to get a converted non-inverted signal as a superposition of a red-shifted and a blue-shifted spectral component having a complementary patterning effect on the different spectral signal components.

Chapter 6 deals with the generation of certain modulation formats after the SOA and the filter. In this case, the filter after the SOA has to re-invert the converted signal to mitigate the patterning effect, and to improve the signal quality besides generating a suitable format. Starting with a 33% RZ data signal and using different filter systems, the conversion of RZ to VSB and RZ to CSRZ modulation formats for the wavelength converted optical signal have been realized.

In Appendix A the temporal effects between pulse dynamics on the one side and refractive index dynamics and SOA gain on the other side are analyzed. Appendix B is devoted to the calculation of integrals being relevant for the developed analytical model. The subsequent appendix, Appendix C, contains a short overview on the degenerated and nondegenerated two-photon absorption coefficients.

Vorwort (German preface)

Technologische Innovationen in Einmoden-Lichtwellenleitern und Halbleiterbauteilen fördern die Forschung auf dem Gebiet der optischen Kommunikation. Millionen von Kilometern von Einmodenfasern sind heutzutage bereits verlegt und werden für Datenkommunikation genutzt. Das exponentielle Wachstum von Internetverkehr, Sprachübertragung und Video-on-Demand-Diensten erfordert mehr und mehr Netzwerkkapazität.

Es wird erwartet, dass die verfügbare Gesamtbandbreite von Einmodenfasern von neuen Technologien im Zeitmultiplex (TDM), im Wellenlängenmultiplex (WDM) und Orthogonal Frequency Division Multiplexing (OFDM) Verfahren immer effizienter ausgenutzt wird. In den letzten Jahren hat man die Einführung vieler neuer Technologien für die optische Übertragung beobachten können, bei der die Kapazität des globalen Telekommunikationsnetzes enorm erweitert wurde.

Um eine spektral-effiziente Übertragung bei hoher Datenkapazität zu erreichen, müssen fortschrittliche, voll-optische Signalverarbeitungsfunktionen umgesetzt werden, wie z. B. Schaltfunktionen, Wellenlängenkonverter, Logikgatter, Flip-Flop-Speicher, Signalregeneratoren und Modulationskonverter.

Voll-optische Signalverarbeitungsfunktionen werden in der Regel durch Ausnutzung nichtlinearer optischer Effekte, die in einem Halbleiterbauteil auftreten, umgesetzt. In voll-optischen Signalverarbeitungssystemen, die auf Anwendungen in Telekommunikationsnetzwerken zielen, werden nichtlineare Effekte hauptsächlich in optischen Fasern, Halbleitermaterialien (InGaAsP/GaAs) und Festkörper-Kristallen, wie Lithiumniobat ($LiNbO_3$), genutzt. Halbleitermaterialien sind vorteilhaft für die Nutzung in voll-optischen Signalverarbeitungssystemen, insbesondere für optische Halbleiterverstärker (SOA). SOAs haben mehrere markante Vorteile: Erstens kann die optische Leistung des Eingangssignals aufgrund der inhärenten Verstärkung im Bauteil niedrig sein, was zu hoher Energieeffizienz führt. Zweitens sind die Abmessungen des SOAs klein, im Vergleich zu Bauteilen auf der Basis anderer Materialien, und drittens können SOAs mit anderen photonischen Bauelementen integriert werden. SOAs können monolithisch mit Laserdioden, optischen Modulatoren, Photodioden und passiven Wellenleitern, einschließlich Multimoden-Interferenz-Kopplern integriert werden. Integrierte Bauelemente können komplexere Funktionalitäten bereitstellen, wie beispielsweise voll-optische Wellenlängenumsetzer, voll-optische Schalter, sowie Signalregeneratoren. Schließlich ist die große Verstärkungsbandbreite und die flexible Wahl der Wellenlänge eine weitere attraktive Eigenschaft von SOAs.

Ein Nachteil der SOA-basierten Signalverarbeitungssysteme ist die lange Erholungszeit der Ladungsträger. Dieser Effekt, der zu einer signifikanten Bitmusterabhängigkeit (Patterning) im Signal führt, begrenzt die maximal nutzbare Bitrate. Eine Minderung des Patterning-Effekts von SOAs bei hohen Bitraten kann durch optische Filtersysteme erzielt werden.

Zwei Signale gleicher Wellenlänge, die durch dieselbe optische Glasfaser transmittiert werden, können sich gegenseitig blockieren. Eine Blockierung kann verhindert werden, wenn durch eine Wellenlängenkonversion eine der beiden Wellenlängen geändert wird. Eine SOA-basierte Wellenlängenkonversion beruht auf der Gewinn- und Brechzahländerung des aktiven Materials des optischen Halbleiterverstärkers. Während der Wechselwirkung mit dem Lichtimpuls finden eine Vielzahl dynamischer Prozesse im Verstärker statt. Die nichtlinearen Inter- und Intraband-Prozesse beeinflussen sowohl den Pump-Lichtimpuls als auch die optische Probe-Welle, die beide gleichzeitig durch den Verstärker propagieren. Dabei werden Veränderungen der Amplitude, Phase und Frequenz des Probe-Licht bei der Wellenlängenkonversion genutzt.

Zusätzlich lassen sich optische Wellenlängenumsetzer auch zur Konvertierung des Modulationsformats und zur Signalregeneration nutzen. Beide Vorteile lassen sich durch eine geeignete optische Filterung des wellenlängenkonvertierten Signals erreichen. Da sich die optimalen Filtereigenschaften aus dem Spektrum des wellenlängenkonvertierten Signals ergeben, ist – basierend auf der Kenntnis der Gewinn- und Brechzahldynamik – eine Zuordnung der spektralen Komponenten zu physikalischen Effekten im SOA möglich.

Die vorliegende Arbeit befasst sich mit den grundlegenden Eigenschaften von nichtlinearen Effekten in SOAs. Dabei werden sowohl die Gewinn- und Brechzahlmodulation, als auch die spektralen Bestandteile des Ausgangssignals identifiziert und den physikalischen Effekten zugeordnet.

In dieser Dissertation werden Methoden der Wellenlängen- und Modulationsformatkonversion bei höheren Bitraten beschrieben und experimentell untersucht.

Mit den gewonnenen Erkenntnissen kann auch die Signalqualität verbessert werden, wozu ein Experiment erläutert wird, bei dem ein Filter für eine bitmusterunabhängige Wellenlängenkonversion mit gleichzeitigem Wechsel des Modulationsformats von return-to-zero (RZ) zu vestigial sideband (VSB) und von RZ zu carrier-suppressed-return-to-zero (CSRZ) verwendet wird.

Fortgeschrittene Modulationsformate, wie VSB und CSRZ, zeigen eine gute Toleranz gegenüber linearen und nichtlinearen Beeinträchtigungen, die entlang der optischen Übertragungsstrecke auftreten können. Durch die progressive Phasenverschiebung von $\pi/2$ und π für VSB bzw. CSRZ Formate, wird die Intersymbol-Interferenz (ISI) reduziert. Da VSB zudem eine hohe spektrale Effizienz besitzt, ist dieses Format für transparente Netzwerke geeignet.

Die Dissertation ist wie folgt strukturiert:

Kapitel 1 enthält eine kurze Einleitung zu den linearen und nichtlinearen optischen Prozessen.

In Kapitel 2 werden der Gewinnkoeffizient und die nichtlineare Brechzahl im Halbleiterverstärker eingeführt.

Die dynamischen Prozesse während der Wechselwirkung zwischen Lichtimpuls und Verstärker und die daraus resultierenden Nichtlinearitäten werden im Kapitel 3 analysiert. Zeitabhängige Änderungen des Gewinnkoeffizienten und der Brechzahl spiegeln sich in den optischen Pump- und Probe-Spektren wieder.

Kapitel 4 stellt gemessene und berechnete optische Spektren vor. Mit Hilfe eines analytischen Modells für Gewinn- und Phasenmodulation werden die Entstehung und die Dynamik der Spektralkomponenten erklärt. Dabei wird jeder Spektralkomponente des wellenlängenkonvertierten Probe-Lichts ein bestimmter Effekt zugeschrieben. Diese grundlegende Erkenntnis bestimmt daher sowohl den, für eine geeignete Wellenlängen-Konversion optimalen, optischen Filter als auch die passenden Signal-Leistungen und den Injektionsstrom.

Kapitel 5 gibt einen Überblick über die verschiedenen Aufbauten der auf optischer Filterung basierenden Wellenlängen-Konverter, mit dem Ziel einer Minderung des Patterning-Effekts im Ausgangssignal.

Experimentelle Aufbauten für Wellenlängen- und Modulationsformat-Konverter werden im Kapitel 6 vorgestellt.

Die Dynamik der infolge der Wechselwirkung des Pumppulses mit dem SOA auftretenden Nichtlinearitäten werden in Appendix A erläutert.

In Appendix B wird die Durchführung der für das Modell erforderlichen Integrale beschrieben.

Die Beschreibung der Zwei-Photonen-Übergänge, in denen das absorbierte Photonenpaar von beiden Lichtquellen, Pump- und Probe-Licht, stammt, nimmt eine besondere Rolle im analytischen Modell von Kapitel 4 an. Diese sogenannte nicht-degenerierte Zwei-Photonen-Absorption und der einfachere Fall von Absorption, degenerierter (d.h. identischer) Photonen, werden in Appendix C ausführlich erklärt.

1 Linear and nonlinear optics

The underlying cause of all linear and nonlinear optical effects is the interaction of electromagnetic radiation with matter (an insulator or a semiconductor) and the response of matter to the radiation. The response of matter provides information about the reaction of the material system and its physical characteristics. In Fig. 1.1 an optical input beam, light beam 1, enters the material and interacts with it. The optical output beam, light beam 2, carries information about the changes in optical properties of the material.

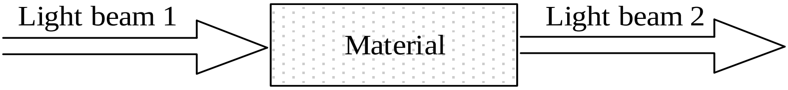

Fig. 1.1. Interaction of light with matter.

By considering the “degree of alteration” of the material after the interaction with the radiation, the optical processes are classified into linear and nonlinear ones [1, 2].

We describe the response of the material to the electric field by the polarization vector $\vec{P}(x,y,z,t)$. We assume a spatially local response to the field and omit in the following the spatial coordinates. The relation between the components $P_i(t)$ of the electric polarization vector and the components $E_i(t)$ of the electric field can be represented by the Volterra series [3]

$$P_i(t) = \varepsilon_0 \sum_{N=1}^{\infty} \int_{-\infty}^{\infty} \ldots \int_{-\infty}^{\infty} \chi^{(N)}_{i\,j_1 \ldots j_N}(t_1,\ldots,t_N) E_{j_1}(t-t_1) \ldots E_{j_N}(t-t_N)\, \mathrm{d}t_1 \ldots \mathrm{d}t_N \,, \quad (1.1)$$

with $\varepsilon_0 = 8.85419 \times 10^{-12}\ \mathrm{As}/(\mathrm{Vm})$ being the electric permittivity of the vacuum. The functions $\chi^{(N)}_{i\,j_1 \ldots j_N}(t_1,\ldots,t_N)$ form the components of a symmetric tensor of rank $N+1$, are fully symmetric in the time variables $t_1,\ldots,t_N$, and are called influence functions of order N. The indices $i, j_1, \ldots, j_N$ take on the values 1,2,3. We adopt the Einstein summation convention over repeated indices. Causality states that the effect cannot precede the cause. This implies that $\chi^{(N)}_{i\,j_1 \ldots j_N}(t_1,\ldots,t_N)$ vanishes for at least one negative time argument.

1.1 Linear optics

The effect of a weak light beam on a transparent material leads to the formation of dipoles in the material which oscillate at the same frequency as the incident light. An electromagnetic field (light beam 2) will be reemitted by a linear material as long as light beam 1 influences the material. Light beam 2 might be identical to light beam 1 for linear transparent material, or attenuated through absorption with a constant absorption coefficient, if the light frequency is near the medium resonance.

The dominant contribution in Eq. (1.1), $P_{Li}(t)$, is due to the term linear in the components of the electric field,

$$P_{Li}(t) = \varepsilon_0 \int_0^{\infty} \chi^{(1)}_{i\,j}(t')\, E_j(t-t')\, \mathrm{d}t' \,, \tag{1.2}$$

where we already made use of the causality principle. Upon Fourier-transforming both sides of Eq. (1.2) the linear polarization becomes

$$\breve{P}_{Li}(\omega) = \varepsilon_0\; \underline{\chi}^{(1)}_{i\,j}(\omega)\, \breve{E}_j(\omega) \,, \tag{1.3}$$

where $\breve{P}_{Li}(\omega)$, $\underline{\chi}^{(1)}_{i\,j}(\omega)$ and $\breve{E}_i(\omega)$ are the Fourier transforms of $P_{Li}(t)$, $\chi^{(1)}_{i\,j}(t)$ and $E_i(t)$, respectively. The components $\underline{\chi}^{(1)}_{i\,j}(\omega)$ defined by

$$\underline{\chi}^{(1)}_{i\,j}(\omega) = \int_{-\infty}^{\infty} \exp(-\mathrm{j}\omega t)\, \chi^{(1)}_{i\,j}(t)\, \mathrm{d}t = \int_0^{\infty} \exp(-\mathrm{j}\omega t)\, \chi^{(1)}_{i\,j}(t)\, \mathrm{d}t \,, \tag{1.4}$$

also form a symmetric tensor of rank 2, called the linear susceptibility tensor. Being the Fourier transform of a real-valued function, $\underline{\chi}^{(1)}_{i\,j}(\omega)$ fulfills the relation

$$\underline{\chi}^{(1)*}_{i\,j}(\omega) = \underline{\chi}^{(1)}_{i\,j}(-\omega) \,. \tag{1.5}$$

The second equality in Eq. (1.4) follows from the causality of the polarization response and allows, together with Eq. (1.5), to connect the real and imaginary parts of $\underline{\chi}^{(1)}_{i\,j}(\omega)$ by the Kramers-Kronig relations. As a consequence, real and imaginary parts of the linear complex susceptibility cannot be chosen independently for all positive values of the angular frequency ω.

In non-transparent materials resonant excitations of dipoles occur. As a consequence, one might detect absorption and/or emission of light. For isotropic media, $\underline{\chi}_{i\,j}^{(1)}(\omega)$ reduces to a single complex scalar $\underline{\chi}^{(1)}(\omega)$. One can relate the linear susceptibility $\underline{\chi}^{(1)}(\omega)$ with the complex-valued dielectric constant $\underline{\varepsilon}_\mathrm{r}$ by Fourier-transforming the relation between electric displacement and electric field

$$\breve{D}_i(\omega)=\varepsilon_0\breve{E}_i(\omega)+\breve{P}_i(\omega)=\varepsilon_0\underline{\varepsilon}_\mathrm{r}(\omega)\breve{E}_i(\omega),\quad \underline{\varepsilon}_\mathrm{r}(\omega)=1+\underline{\chi}^{(1)}(\omega). \tag{1.6}$$

Here $\breve{D}_i(\omega)$ is the Fourier-transform of the i-th component of the electric displacement vector. The complex refractive index $\underline{n}(\omega)$ is defined by

$$\underline{n}^2(\omega)=\underline{\varepsilon}_\mathrm{r}(\omega)=1+\underline{\chi}^{(1)}(\omega). \tag{1.7}$$

The real and imaginary parts of $\underline{n}(\omega)$ define the refractive index $n(\omega)$ and the power absorption coefficient $a(\omega)$ according to

$$\underline{n}(\omega)=n(\omega)-\mathrm{j}\frac{c}{2\omega}a(\omega), \tag{1.8}$$

where $c=299792458\,\mathrm{m/s}$ is the vacuum speed of light. Combining Eqs. (1.7) and (1.8), one can express $\underline{\chi}^{(1)}(\omega)$ in terms of $n(\omega)$ and $a(\omega)$. Obviously, the refractive index and the absorption coefficient do not depend on the light power.

1.2 Nonlinear optics

Under the influence of a strong electromagnetic field, a material changes its physical properties. The “degree of alteration” of the material is a measure of the nonlinearity.

The influence functions $\chi_{i\,j_1\cdots j_N}^{(N)}(t_1,\ldots,t_N)$ of order N with $N\geq 2$ occurring in Eq. (1.1), uniquely characterize the nonlinearities of order N because they are fully symmetric in the time variables [4]. Indeed, the i-the component of the N-th order polarization $P_i^{(N)}(t)$, defined as

$$P_i^{(N)}(t)=\varepsilon_0\int_0^\infty\ldots\int_0^\infty\chi_{i\,j_1\cdots j_N}^{(N)}(t_1,\ldots,t_N)E_{j_1}(t-t_1)\ldots E_{j_N}(t-t_N)\,\mathrm{d}t_1\ldots\mathrm{d}t_N\,, \tag{1.9}$$

does not change by using Volterra kernels of N-th order obeying causality but being unsymmetrical in the time arguments.

1.2.1 Role of the material in nonlinear processes

Nonlinear processes can be classified being non-resonant (also known as parametric) and resonant (also known as non-parametric) processes. The parametric processes are mainly concerning phenomena in which the material plays a passive role. The time-varying polarization of the material $\vec{P}(t)$ acts as a source of new frequency components of the electromagnetic field.

In contrast, the material response in non-parametric processes is active due to the significant modifications of its optical properties, caused by the energy exchange with a light beam. This modification can be also experienced by another, time delayed light beam.

1.2.2 Parametric processes

Parametric or passive processes are those in which the material acts essentially as a catalyst and in which it serves as an intermediate medium for the interaction between several coherent light beams. There is no net energy exchange between light and matter, and the material response is almost instantaneous with the consequence that energy is conserved among the light beams (Manley-Rowe relation), see Fig. 1.2.

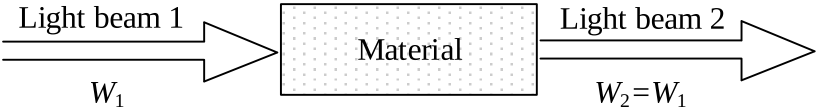

Fig. 1.2. Parametric processes.

This almost instantaneous response occurs as the light-matter interaction induces only transitions to virtual energy eigenstates of the material system. Parametric processes are described by real susceptibilities.

In parametric processes the initial and the final quantum mechanical states of the material are identical. Examples of parametric processes are: second and third harmonic generation, sum and difference frequency generation, optical parametric oscillations, and light intensity dependent refractive index.

1.2.3 Non-parametric processes

In a non-parametric process, real excitations are involved in the dynamics, giving rise to energy dissipation. For most processes, the transient regime of optical nonlinearities occurs when the material response to an intense light field is slower than the rate of variations of the light intensity. This is the case, when light causes a material excitation due to an energy transfer between the light beam and the material (Fig. 1.3) [5].

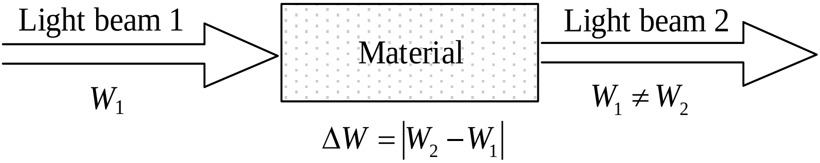

Fig. 1.3. Non-parametric processes.

A part of the energy of the light, ΔW, may be transferred to or from the material which gets changed, e.g., by the generation of phonons observed by stimulated Brillouin and Raman scattering, molecular reorientation, and changes of the occupation of states in the semiconductor conduction and valence band.

If the degree of perturbation is sufficiently large, the perturbation gives rise to a sizeable change of the optical properties. An observer would measure transmission changes, refractive index changes, induced birefringence and light scattering. Some non-parametric processes are the saturated absorption and gain in direct gap semiconductors, the two-photon absorption (TPA) and the stimulated Brillouin and Raman scattering in which frequencies of incident photon and material phonons add up to give the resulting photon frequencies. Non-parametric processes are described by the complex susceptibility. Both parts of this susceptibility, the nonlinear gain or absorption due to saturation and the nonlinear refractive index are dependent on the radiation intensity.

The nonlinearities in direct gap semiconductors and especially the saturation observed in band-to-band transitions, will be reported on in chapter 2.

Note, that there is not always a clear-cut separation between the two classes of optical nonlinearities [1, 2, 5, 6]. There are pure parametric and non-parametric processes, but also mixed processes with different weights for their resonant and non-resonant components.

Pump-probe experiments for non-parametric processes

One of the basic configurations used to experimentally study the temporal response of non-parametric optical nonlinearities, is shown in Fig. 1.4.

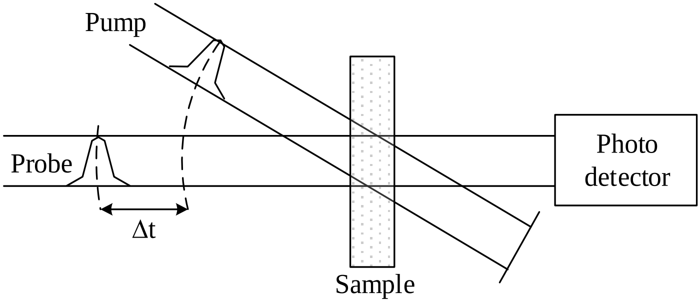

Fig. 1.4. Pump-probe experiment.

The pump-and-probe configuration consists of one beam exciting the material from the equilibrium and a second (low-power) beam probing the changes of the optical material properties. These changes are observed in transmission, in phase because of a nonlinear refractive index, or in the polarization state of the probe beam. Due to a slow reaction of the material on the pump light excitation, a variation of the delay (Δt) of the probe with respect to the pump will show the temporal evolution of the optical properties of the sample. The probe can be a single pulse (see Fig. 1.4) or a continuous wave (CW).

1.3 Summary

Within the framework of nonlinear optics, one light beam can influence another one and the superposition principle is no longer valid. A first beam induces modifications in the optical properties of the material acting thus on a second beam. In the latter case the output pulse shows a modified shape and a different spectrum due to self-phase modulation.

2 Nonlinearities in semiconductor optical amplifiers

2.1 Basic description of travelling-wave semiconductor optical amplifiers

Semiconductor optical amplifiers (SOAs) are optoelectronic devices similar to semiconductor lasers which are specially designed to amplify light. In contrast to semiconductor lasers, SOA amplify light in a single pass and have, therefore, no optical cavity. The nonlinear behavior of the semiconductor material with respect to the light power, is very often used to perform wavelength conversion and switching functionalities.

A schematic diagram of an SOA is shown in Fig. 2.1.

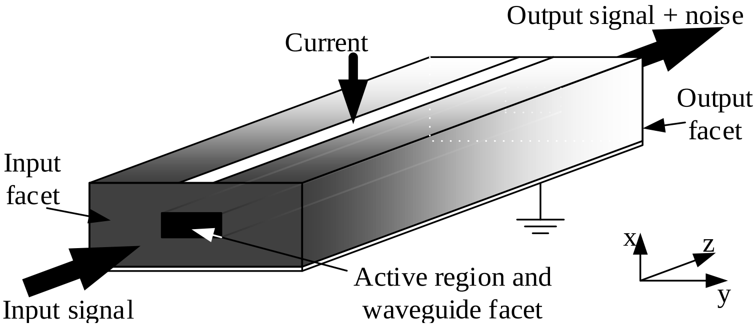

Fig. 2.1. Schematic diagram of an SOA with a buried active region.

An electric current is injected into the active region of the device, realizing the population inversion necessary for the amplification by stimulated emission. The active region is a thin layer between a p-type and a n-type semiconductor layer [7] such that its bandgap is smaller than those of the layers surrounding it (Fig. 2.2). This helps to confine electrons and holes to the middle layer. Only a single waveguide mode exists in the active region of the travelling-wave amplifier.

The bias current is assumed to pass through the active region. Only a fraction, called field confinement factor, of the input signal extends into the active region.

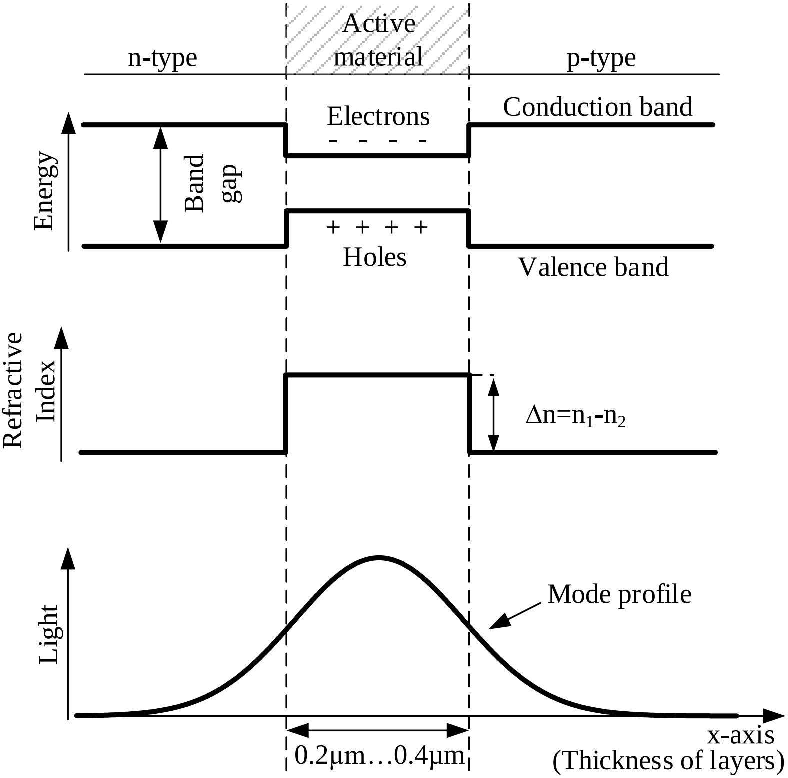

Fig. 2.2. Schematic representation of electrical and optical confinement in a double heterostructure SOA design.

About 70% from the mode is spread outside the active region of the SOA. The role of the active layer is to confine the injected carriers inside the material under a forward bias. The carrier confinement occurs because of the bandgap discontinuity at the junction between the semiconductor materials of same lattice constant but of different bandgaps (double heterostructure). In this central region, electrons and holes recombine and generate light. To realize an optical waveguide, the active region has a larger refractive index than the surrounding p-type and n-type cladding layers.

Different theoretical models have been developed to determine the relation between the bandgap energy and the refractive index, see, e.g., [8]. All of them have in common that with increasing bandgap the refractive index decreases.

2.2 The optical amplification process in SOAs

SOAs amplify incident light using stimulated emission like semiconductor lasers, but without optical feedback. The main condition for amplification is the existence of a population inversion which means that the Fermi-level separation (FLS) exceeds the bandgap. The principle of optical amplification can be easily explained using the simple band structure consisting of a conduction band (CB) and a valence band (VB), both of parabolic form in the energy-wave vector plane (Fig. 2.3) [9-12].

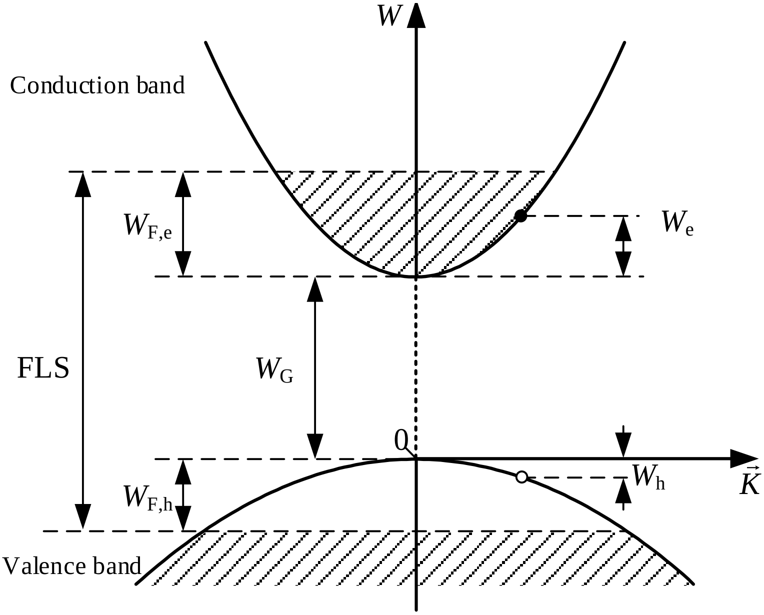

Fig. 2.3. Two band model of a direct bandgap semiconductor. The quasi-Fermi level energies $W_{F,e}$ *,* $W_{F,h}$ *for electrons and holes, as well as their kinetic energies* W_e *and* W_h *are positive. The separation between the Fermi levels, denoted with FLS, is also positive.* $\vec{K}$ *represents the wave vector of the electron.*

The carriers, electrons (e) and holes (h), are in thermal equilibrium within each band. Therefore, they are described by distinct Fermi-Dirac distributions. Denoting with $W_{F,e}$ ($W_{F,h}$) the quasi-Fermi level energy of the electron (hole) measured from the CB (VB) edge, the occupation probability $f_\mathrm{e}(W_\mathrm{e})$ $\left(f_\mathrm{h}(W_\mathrm{h})\right)$ of a state of kinetic energy W_e (W_h) at absolute temperature T is

$$f_\mathrm{e}(W_\mathrm{e}) = \left[1+\exp\left(\frac{W_\mathrm{e}-W_\mathrm{F,e}}{k_\mathrm{B}T}\right)\right]^{-1} \tag{2.1}$$

for an electron, and

$$f_\mathrm{h}(W_\mathrm{h}) = \left[1+\exp\left(\frac{W_\mathrm{h}-W_\mathrm{F,h}}{k_\mathrm{B}T}\right)\right]^{-1} \tag{2.2}$$

for a hole. Here $k_\mathrm{B} = 1.38065\times10^{-23}\ \mathrm{J/K}$ denotes the Bolzmann constant.

Fermi level energies are determined by the temperature and the carrier densities. In case of free carriers, the density of energy states is given by

$$\rho_\mathrm{e}\left(W_\mathrm{e}\right) = \frac{1}{2\pi^2}\left(\frac{2m_\mathrm{e}}{\hbar^2}\right)^{3/2}\sqrt{W_\mathrm{e}} \tag{2.3}$$

for electrons, and

$$\rho_\mathrm{h}\left(W_\mathrm{h}\right) = \frac{1}{2\pi^2}\left(\frac{2\left|m_\mathrm{h}\right|}{\hbar^2}\right)^{3/2}\sqrt{W_\mathrm{h}} \tag{2.4}$$

for holes. Here m_e (m_h) is the effective mass of the electron (hole) and $\hbar$ is the reduced Plank constant, $\hbar = 1.05457\times10^{-34}\ \mathrm{Js}$. In the absence of doping, the densities of electrons

$$N_\mathrm{e} = \int_0^\infty f_\mathrm{e}\left(W_\mathrm{e}\right)\rho_\mathrm{e}\left(W_\mathrm{e}\right)\mathrm{d}W_\mathrm{e} \tag{2.5}$$

and of holes

$$N_\mathrm{h} = \int_0^\infty f_\mathrm{h}\left(W_\mathrm{h}\right)\rho_\mathrm{h}\left(W_\mathrm{h}\right)\mathrm{d}W_\mathrm{h} \tag{2.6}$$

are the same and their common value will be denoted by N, i.e., $N_{\mathrm{e}} = N_{\mathrm{h}} = N$ holds. From now on we will use N to indicate the carrier density since the active medium is always undoped.

Carrier pairs recombine radiatively (yielding spontaneous or stimulated emission) or non-radiatively (e.g., Auger and Shockley-Read-Hall recombinations).

If a photon with an energy $\hbar\omega$ situated in the range between W_{G} and the FLS is injected into the SOA, it causes the stimulated recombination of a carrier pair. The stimulated recombination of the electron-hole pair leads to a new photon, identical in all aspects to the incident photon. This new photon is coherent to the incident photon, i.e., it has the same frequency, direction, polarization and phase.

For a direct bandgap semiconductor, it is convenient to work with the effective reduced mass, $m_{\mathrm{r}} = m_{\mathrm{e}} \left| m_{\mathrm{h}} \right| / \left(m_{\mathrm{e}} + \left| m_{\mathrm{h}} \right| \right)$, and with the sum of electron and hole kinetic energies, hereafter called kinetic energy of the reduced mass, $W = W_{\mathrm{e}} + W_{\mathrm{h}}$. The following equalities hold:

$$\rho_{\mathrm{e}}\left(W_{\mathrm{e}}\right)\mathrm{d}W_{\mathrm{e}} = \rho_{\mathrm{h}}\left(W_{\mathrm{h}}\right)\mathrm{d}W_{\mathrm{h}} = \rho_{\mathrm{r}}\left(W\right)\mathrm{d}W \tag{2.7}$$

where $\rho_{\mathrm{r}}\left(W\right)$ is the reduced density of energy states

$$\rho_{\mathrm{r}}\left(W\right) = \frac{1}{2\pi^2}\left(\frac{2m_r}{\hbar^2}\right)^{3/2}\sqrt{W}\ . \tag{2.8}$$

By denoting the dipole matrix element by $M\left(W\right)$ and the Lorentzian line shape by $\mathscr{L}\left(W\right)$, the dependency on the kinetic energy of the reduced mass W is given by

$$M\left(W\right) = \frac{M\left(0\right)}{\left(1+\dfrac{W}{W_{\mathrm{G}}}\right)}\ , \tag{2.9}$$

and

$$\mathscr{L}\left(W\right) = \left\{\pi\hbar T_2\left[\left(\omega-\left(W_{\mathrm{G}}+W\right)/\hbar\right)^2+\left(1/T_2\right)^2\right]\right\}^{-1}\ , \tag{2.10}$$

with T_2 as the dipole relaxation time. The unsaturated material gain coefficient $\bar{g}_0$ is a measure for the linear amplification. It can be expressed at an angular frequency ω as [10]

$$\bar{g}_0(\omega)=\frac{\pi\omega^2}{\varepsilon_0 c n_0 \omega_0}\int_0^\infty \left\{ f_\mathrm{e}\left(\tfrac{m_\mathrm{r}W}{m_\mathrm{e}}\right)-\left[1-f_\mathrm{h}\left(\tfrac{m_\mathrm{r}W}{|m_\mathrm{h}|}\right)\right]\right\} \left|M(W)\right|^2 \rho_\mathrm{r}(W)\mathscr{L}(W)\,\mathrm{d}W, \qquad (2.11)$$

with ω_0 the central angular frequency of the input light and $n_0 = n(\omega_0)$ the refractive index of the SOA, see Eq. (1.8).

Photons with energies greater than the FLS can only be absorbed. On the other hand, the material of the active region is transparent for photons with energies below the gap energy W_G. The process of the two-photon absorption (TPA) allows an interband transition via photons with energies below the gap energy. This effect has a low probability, so TPA is mostly seen at high optical input powers.

During the radiative process of spontaneous emission, carriers recombine and emit uncorrelated photons of random phases and direction. Spontaneously emitted photons have a wide variety of frequencies. While propagating through an active material, these photons induce a stimulated amplification process called amplified spontaneous emission (ASE). ASE is essentially responsible for the noise induced into an SOA. Since ASE cannot be avoided in optical amplifiers, optical band pass filters are commonly employed to reduce the noise of a noise-impaired signal to a minimum value.

2.3 Gain

The optical gain G (known also as amplifier gain or SOA gain) is defined as the ratio of the output power P^out after an SOA with respect to the input power P_in being launched into the SOA,

$$G = \frac{P^\mathrm{out}}{P_\mathrm{in}}. \qquad (2.12)$$

The optical gain value is usually expressed in logarithmic decibel units, $G_\mathrm{dB} = 10\log_{10} G$. The gain spectrum of an SOA depends on the material structure and the operating conditions. In the range of $W_G < \hbar\omega < \mathrm{FLS}$, the gain is positive and has a peak that increases in magnitude and shifts towards higher energies with growing carrier density N, i.e., with increasing current

[11]. The transparency point energy (stimulated absorption and emission are balanced) depends on temperature T and carrier density N, while the bandgap energy W_{G} essentially depends on the material composition.

We can obtain the expression for the gain G from the equation describing the light power $P(z)$ along the propagation axis z,

$$\frac{\mathrm{d}P(z)}{\mathrm{d}z} = \left[\Gamma g_{\mathrm{m}}(z) - \alpha_{\mathrm{int}}\right] P(z) . \tag{2.13}$$

Here α_{int} is the internal power loss coefficient and $g_{\mathrm{m}}(z)$ the material power gain coefficient. The confinement factor Γ represents the fraction of light power confined in the active material. Internal loss is mainly due to light scattering at the heterostructure interfaces.

Noting that $P(0) = P_{\mathrm{in}}$ and $P(L) = P^{\mathrm{out}}$ for an SOA of length L, the SOA gain is obtained by integrating $P(z)$ in Eq. (2.13),

$$G = \exp\left\{ \int_0^L \left[\Gamma g_{\mathrm{m}}(z) - \alpha_{\mathrm{int}}\right] \mathrm{d}z \right\} . \tag{2.14}$$

For a constant material gain coefficient g_{m}, e.g., $g_{\mathrm{m}} = \overline{g}_0$ from Eq. (2.11), and with negligible internal loss $\alpha_{\mathrm{int}} = 0$, Eq. (2.14) can be further reduced to

$$G_0 = \exp\left(L \Gamma \overline{g}_0\right) . \tag{2.15}$$

Optical gain is realized when the injected carrier density N exceeds a certain value, known as the transparency value N_{tr} which represents the number of carriers lost by non-radiative recombination and scattering.

The peak gain g_{m} increases linearly with the carrier population N and can be approximately expressed as

$$g_{\mathrm{m}}(N) = a_0 \left(N - N_{\mathrm{tr}}\right) \tag{2.16}$$

with $a_0 = \mathrm{d}g_{\mathrm{m}} / \mathrm{d}N$ being the differential gain. The optical gain coefficient, depending only on the carrier density N, is called the band filling gain $g_{\mathrm{BF}} = \Gamma g_{\mathrm{m}}(N)$.

The material gain also depends on the angular frequency ω of the incident light. Since carrier density N and temperature T are related by the Fermi-

Dirac distribution, the material power gain depends on temperature. Therefore, we write $g_\mathrm{m} = g_\mathrm{m}\left(N, T, \omega\right)$.

The carrier concentration N changes with the signal power $P\left(z,t\right)$ according to the carrier density rate equation [9-11]

$$\frac{\partial N\left(z,t\right)}{\partial t} = \frac{I}{eV} - \frac{N\left(z,t\right)}{\tau_s} - \frac{g_\mathrm{m}\left(z,t\right)P\left(z,t\right)}{\hbar\omega A_\mathrm{eff}}, \qquad (2.17)$$

where V is the active volume, I the injection current, τ_s the spontaneous carrier lifetime including spontaneous emission and non-radiative recombination, and $A_\mathrm{eff} = A/\Gamma$ the effective cross-section of the SOA (A as cross-section area of the active region). Since the response of the nonlinear medium depends on the signal power $P\left(z,t\right)$, the material gain coefficient g_m becomes coordinate and time dependent. The three terms indicate the rates at which carrier pairs are created and recombine inside the active region. The last term corresponds to the rate of electron-hole recombination by stimulated emission.

2.4 Nonlinearities in SOAs

Nonlinearities caused by an excitation in the gain region become noticeable in the gain and in the refractive index of an active material. Both nonlinearities have their origin in the change of carrier density and energy distribution in the CB and the VB.

The change of carrier density may occur fast, as with carrier depletion (CD) due to stimulated recombination, or significantly slower, as with carrier recovery (CR). The gain contribution associated with CD or CR follows the carrier dependence Eq. (2.16), and is usually referred to as band filling (BF) contribution.

The change of carrier energy distribution is influenced by several effects such as free carrier absorption (FCA), two-photon absorption (TPA), and removal of cool carriers through stimulated emission, which gives rise to spectral hole burning (SHB) as well as to carrier heating (CH). Due to FCA, a carrier is excited in a higher energetic state within the same band by absorbing a photon. The carrier energy distribution is changed with the absorbed photon energy.

Free carrier absorption accompanying band filling (FCA$_{\text{BF}}$) is an interaction of electrons and holes with photons, a so-called plasma-effect. Since the absorption coefficient is proportional to the concentration of carriers N, this plasma-effect can be included in the BF effect. To see this, let us assume that the local gain contribution as defined in the right-hand side of Eq. (2.13) is entirely due to band filling, i.e., $\Gamma g_{\text{m}} = g_{\text{BF}}$ and to internal loss α_{int}. By using Eq. (2.16) for g_{m} one finds

$$\Gamma g_{\text{m}} - \alpha_{\text{int}} = \Gamma a_0 \left(N - N_{\text{tr}}\right) - \alpha_{\text{int}} . \tag{2.18}$$

The absorption coefficient due to FCA$_{\text{BF}}$ can be expressed in terms of the absorption cross-section σ_β as $\sigma_\beta N$ where β denotes the band index β =CB or VB. By taking into account the FCA$_{\text{BF}}$ effect in both CB and VB, one can write

$$\Gamma g_{\text{m}} - \alpha_{\text{int}} - \sum_\beta \sigma_\beta N = \left(\Gamma a_0 - \sum_\beta \sigma_\beta\right)\left(N - N_{\text{tr}}\right) - \left(\alpha_{\text{int}} + \sum_\beta \sigma_\beta N_{\text{tr}}\right). \tag{2.19}$$

Therefore, including the FCA$_{\text{BF}}$ effect in the BF amounts to redefinitions of the differential gain $a_0 \to a_0 - \sum \sigma_\beta / \Gamma$ and internal loss $\alpha_{\text{int}} \to \alpha_{\text{int}} + N_{\text{tr}} \sum \sigma_\beta$. To represent a differential gain, the difference $a_0 - \sum \sigma_\beta / \Gamma$ must be positive, otherwise the FCA$_{\text{BF}}$ effect has to be treated independently of BF.

TPA is an interband effect where a VB electron absorbs two photons to reach the CB. A TPA-created electron can be further excited by direct absorption of another photon. This TPA-induced FCA, denoted in the following as FCA$_{\text{TPA}}$, is different from FCA$_{\text{BF}}$ since it does not depend on the total carrier density N, but only on the density of TPA-produced electrons in the CB, N_{ex}.

A dip within the distribution of the carriers characterizes the SHB effect. This dip arises due to an excessive recombination of carriers within the energy domain, where stimulated emission occurs.

A qualitative illustration of the induced transitions in an SOA, including stimulated emission, FCA and TPA as well as subsequent changes in the distribution of the CB electrons is shown in Fig. 2.4. These effects are responsible for altering the Fermi-Dirac distributions and for nonequilibrium distributions in the bands. Note that the nonequilibrium occupation probabilities $f_\mathrm{e}^\mathrm{neq}$ and $f_\mathrm{h}^\mathrm{neq}$ are different from f_e and f_h introduced in Eqs. (2.1) and (2.2), respectively.

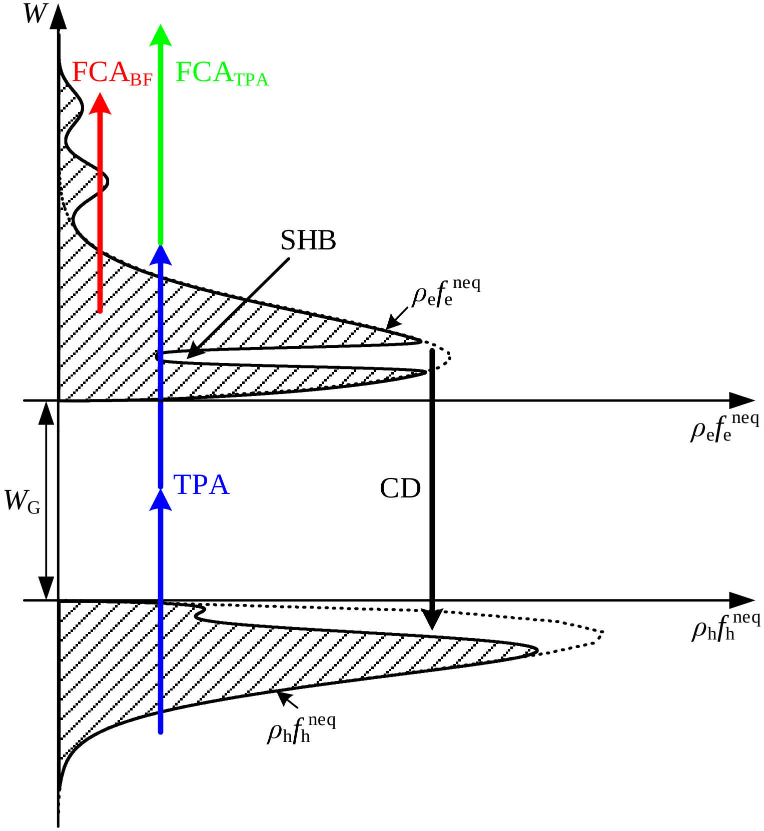

Fig. 2.4. *Schematic representation of the radiative transitions in SOAs and the change of the carrier distribution. The product* $\rho_\mathrm{e} f_\mathrm{e}^\mathrm{neq}$ $\left(\rho_\mathrm{h} f_\mathrm{h}^\mathrm{neq}\right)$ *with* ρ_e $\left(\rho_\mathrm{h}\right)$, *defined in Eq. (2.3) (Eq. (2.4)), is the electron (hole) spectral density.*

All these processes increase the total energy of the carrier distribution, resulting in carrier heating (CH). Since carriers get higher kinetic energies, they acquire a temperature larger than the lattice temperature.

The sum of the effects of CD, SHB, TPA, FCA and CH leads to the nonlinearities of gain and refractive index in an SOA.

2.4.1 Gain saturation and nonlinear gain compression

If the power of the input signal is such that the signal has negligible influence on the SOA gain, the signal is called a “small-signal”. For small input signals with powers which do not saturate the SOA gain, the SOA works as a linear amplifier. As the signal power increases, the carriers in the active region deplete, leading to a decrease in the gain, known as gain saturation effect. The saturation of the amplification is mainly a band filling nonlinearity. It can be regarded as a limitation of the number of states that can participate in transitions giving rise to optical gain.

In case of a CW beam the steady state value of the carrier density N can be obtained by setting $\partial N/\partial t = 0$ in Eq. (2.17). Both carrier density and material power gain coefficient depend only on the coordinate z, as the CW power $P(z)$ is time independent. By using Eq. (2.16) one can eliminate the carrier density $N(z)$ in the steady state form of the rate equation Eq. (2.17), and find

$$0 = \frac{I}{eV} - \frac{1}{\tau_s}\left[N_{\mathrm{tr}} + \frac{g_{\mathrm{m}}(z)}{a_0}\right] - \frac{g_{\mathrm{m}}(z)P(z)}{\hbar\omega A_{\mathrm{eff}}}\,. \tag{2.20}$$

In absence of the light $P(z) = 0$, Eq. (2.20) provides the unsaturated value of the gain coefficient

$$\bar{g}_0 = a_0\left(N_{\mathrm{st}} - N_{\mathrm{tr}}\right), \quad N_{\mathrm{st}} = \frac{I\tau_s}{eV}\,. \tag{2.21}$$

From Eqs. (2.20) and (2.21) one obtains the material power gain g_{m} in the saturation regime at a distance z from the SOA input as [11]

$$g_{\mathrm{m}}(z) = \frac{\bar{g}_0}{1 + \dfrac{P(z)}{P_{\mathrm{sat}}}}\,, \tag{2.22}$$

where the saturation power P_{sat} is given by

$$P_{\mathrm{sat}} = \frac{\hbar\omega}{\tau_s}\frac{A_{\mathrm{eff}}}{a_0}\,. \tag{2.23}$$

By substituting Eq. (2.22) in Eq. (2.13), one finds a differential equation for the power $P(z)$ obeying the boundary condition $P(0)=P_{\text{in}}$. After eliminating P_{in} with the help of Eq. (2.12), the output power can be expressed as

$$\frac{P^{\text{out}}}{P_{\text{sat}}}=\frac{\ln\left(\frac{G_0}{G}\right)G}{G-1}. \tag{2.24}$$

In the saturation regime ($G<G_0$) the output power P^{out} is comparable to P_{sat} [11]. If G approaches the unsaturated value G_0, the ratio $P^{\text{out}}/P_{\text{sat}}$ becomes negligible. This conclusion can also be reached by setting $G=G_0$ in Eq. (2.24).

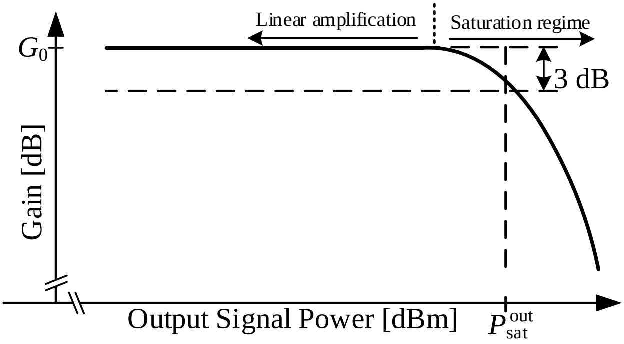

Fig. 2.5. Typical SOA gain versus output signal power.

Fig. 2.5 shows the SOA gain versus the output signal power. $P_{\text{sat}}^{\text{out}}$ represents the output power at which the amplifier gain is suppressed by 3 dB with respect to the unsaturated gain G_0 [7] and can be calculated by setting $G=G_0/2$ in Eq. (2.24),

$$P_{\text{sat}}^{\text{out}}=\frac{G_0\ln 2}{G_0-2}P_{\text{sat}}. \tag{2.25}$$

The carriers in the saturation regime have a shorter lifetime τ_{eff} depending on the signal power P^{out} [9, 11],

$$\frac{1}{\tau_{\text{eff}}} = \frac{1}{\tau_{\text{s}}}\left(1 + \frac{P^{\text{out}}}{P_{\text{sat}}}\right). \tag{2.26}$$

The behavior of the gain depends on the signal power, on the signal type (continuous wave or pulsed), and on the pulse width [11]. Gain saturation implies a gain compression depending on the light power. The material gain includes now both CH and SHB compression coefficients. It can be related to the linear material gain g_{BF} (band filling contribution defined in Eq. (2.16)) by

$$\Gamma g_{\text{m}} = \frac{g_{\text{BF}}}{1 + \varepsilon P}. \tag{2.27}$$

$\varepsilon = \varepsilon_{\text{CH}} + \varepsilon_{\text{SHB}}$ is the nonlinear gain compression parameter measured in W^{-1}. The signal power P relates to the photon density S by

$$S = P\Big/\left(\hbar\omega v_{\text{g}} A_{\text{eff}}\right), \tag{2.28}$$

where v_{g} is the group velocity within the SOA. In this case the denominator in Eq. (2.27) becomes $1 + \overline{\varepsilon} S$ with the gain compression parameter $\overline{\varepsilon}$ measured in m^3.

In an active medium, light of a certain wavelength causes stimulated transitions between specific energy levels but not across the entire gain spectrum. This means that stimulated transitions tend to modify the carrier density in a specific energy region within the conduction (CB) and valence band (VB) of the SOA. Such localized non-uniformities or dips in the carrier distribution, resulting from SHB as well as CH, are responsible for the nonlinear gain suppression (see Fig. 2.4). A strong optical field will cause a “hot” carrier distribution originating from a depletion of the low energy carriers, and through direct photon absorption [10, 13]. Both, SHB and CH, significantly reduce the SOA gain.

2.4.2 Carrier-induced change in refractive index

The dominant effects leading to changes of the refractive index in the active material of an SOA are band filling, bandgap shrinkage, carrier heating through stimulated emission, FCA$_{\text{TPA}}$ and TPA. The change in the refractive index is described by

$$\Delta n(N,\omega) = n(N,\omega) - n_0(\omega), \tag{2.29}$$

with $n_0(\omega)$ the background refractive index of the semiconductor material, and $n(N,\omega)$ the refractive index of a semiconductor at population inversion [13].

Band filling (Burstein-Moss) effect

A change of the carrier density as a result of current injection, stimulated absorption or stimulated emission is called the band filling effect. The band filling determines the absorption energy, the FLS, the gain peak and the refractive index of the SOA. The increase of the absorption energy depending on the carrier density is known as the Burstein-Moss effect.

In [13] the imaginary part of the complex index of refraction, $-c/(2\omega)\ a(\omega,N)$, see Eq. (1.8), is calculated and fitted with experimental data. Alternatively, instead of finding the absorption coefficient $a(\omega,N)$, it is possible to exploit an expression for the material gain g_m with $g_\mathrm{m} = -a$, which is calculated using Fermi's golden rule (quantum-mechanical probability for the dipole transition between CB and VB) [10]. Having now the imaginary part of the complex index of refraction, one can use the Kramers-Kronig theorem to calculate the real part. In this way one can find the change of the refractive index Δn, i.e., the real part which accompanies the change Δa (or $-\Delta g_\mathrm{m}$) in the absorption coefficient.

In the publications [13] and [14], it is shown that the increase of refractive index Δn can be considered as linear with the decrease of the carrier density $\Delta N < 0$. If carrier pairs are created, i.e., $\Delta N > 0$ holds, the refractive index will get smaller ($\Delta n < 0$). It increases ($\Delta n > 0$), if carriers recombine $\Delta N < 0$. It has been calculated that the refractive index change per carrier pair is about $\Delta n_\mathrm{e,h} = 2\times10^{-20}\ \mathrm{cm}^{-3}$ [15] for SOAs based on InGaAsP.

Bandgap shrinkage

The basic mechanism of the bandgap shrinkage is the occupation of states at the bottom of the conduction band by injected electrons. If the concentration is large enough, the electrons form a gas of interacting particles. The electrons will repel one another by Coulomb forces and electrons with same spin will avoid each other because of the Pauli exclusion principle. The net result is a screening of electrons and a decrease of their energy leading to a lower energy for the conduction band edge. A similar correlation effect for holes leads to an energy increase in the valence band. The sum of these effects is the bandgap shrinkage.

This effect causes a translation (red shift) of the absorption curve. The change in absorption is accompanied by a change in refractive index.

Carrier heating, free carrier absorption, two-photon absorption and spectral hole burning

Hot carriers are created because of three different processes, namely stimulated recombination (which eliminates cool carriers with energies close to the band edges), free carrier absorption and two-photon absorption, resulting in a perturbed distribution. An intraband carrier-carrier scattering relaxes the nonequilibrium distribution to a “hot” Fermi-Dirac distribution. The “hot” Fermi-Dirac distribution is a Fermi-Dirac distribution at a temperature higher than the lattice temperature. The intraband process is called carrier heating. The refractive index Δn increases because both spectral densities, $\rho_\mathrm{e} f_\mathrm{e}$ and $\rho_\mathrm{h} f_\mathrm{h}$, and the bandgap energy W_G decrease with increasing temperature. Under thermal equilibrium conditions, the temperature-related refractive index change is $\mathrm{d}n/\mathrm{d}T \leq 10^{-3}\,\mathrm{K}^{-1}$ [10].

In FCA the electron moves to a higher energy state within the same band by absorbing one photon. The corresponding calculated change in the refractive index, due to the carrier concentration in the conduction (CB) and valence band (VB), is described by the plasma-effect within the Drude model [13] of free electrons and holes as

$$\Delta n = -\left(\frac{e^2\lambda^2}{8\pi^2 c^2 \varepsilon_0 n_0}\right)\left(\frac{N_\mathrm{e}}{m_\mathrm{e}} + \frac{N_\mathrm{h}}{|m_\mathrm{h}|}\right), \tag{2.30}$$

where $e = 1.6\times 10^{-19}\,\mathrm{As}$, λ is the vacuum wavelength of light producing carrier absorption, and N_e and N_h are the densities of the quasi-free electrons and holes, respectively. In an SOA, $N_\mathrm{e} = N_\mathrm{h} = N$ holds. Obviously, Δn takes on negative values. Because of the λ-dependency, the absolute value plasma-effect index change, $|\Delta n|$, increases as the photon energy decreases. The carrier concentration depends on the light power.

Two-photon absorption (TPA) is a nonlinear effect that occurs when an electron in the valence band (VB) performs a transition from the ground state to a higher state in the conduction band (CB) by the simultaneous absorption of two photons [16]. This corresponds to the generation of a carrier with an energy higher than the transparency point energy. The refractive index change is negative $\Delta n < 0$ due to a small carrier generation $\Delta N > 0$ and, more importantly, because of the high kinetic energy of these carriers.

The photon absorption by carriers in the bands is called $\mathrm{FCA}_{\mathrm{BF}}$. This effect contributes to both, gain and refractive index change (called free carrier index change FCI). The impact of this effect can be included in the band filling contribution to gain and refractive index.

Spectral hole burning does not affect the change of refractive index due to the symmetry of the material gain change Δg_{m} around the central frequency. The integrand in the Kramers-Kronig relation will be nearly anti-symmetric and thus its contribution vanishes.

The dynamics of these processes will be discussed in-depth in chapter 3.

Combination of effects

All the above discussed carrier effects are independent, and the total change in refractive index corresponds to the sum of the contributions of these effects. As a consequence of the interaction of light with the active material of an SOA, the changes in refractive index Δn are produced by the change of carrier density ΔN (interband effects) and of the energy distribution of carriers in the corresponding bands (intraband effects), effects that all depend on the light intensity.

2.5 Summary

Nonlinear effects in SOAs manifest themselves as refractive index and gain changes. Both, gain and refractive index, depend on the carrier density N and carrier energy distribution, on the wavelength, on the shape (pulse or CW), and on the power of the injected light.

While material gain changes Δg_{m} take place within spectrally narrow regions, where stimulated emission occurs, refractive index changes Δn depend on a wide spectral region. The effect of TPA does not significantly change the total number of carriers in the bands, but it changes their energy distribution. This change in energy distribution of carriers has a smaller effect on the gain as on the refractive index.

3 Dynamics in SOAs

3.1 Introduction

To realize switching devices based on SOAs for high-speed all-optical communications, the nonlinearities of SOAs have to follow the intensity change of the signal closely. Gain and refractive index nonlinearities depend on the input pulse properties in terms of pulse width and input power, on the characteristics of the SOA, and on the applied bias current. Gain and refractive index of the SOA have quite different dynamics regarding their interaction with short optical pulses. When knowing both dynamics, it is possible to choose the proper operating parameters to improve the bandwidth for an SOA based signal processing system.

3.2 Basics of the dynamics in an SOA

3.2.1 Radiative transitions

When an optical pump pulse with frequencies in the gain spectrum is injected into the active region of an SOA, it mainly produces three kinds of radiative transitions [17-19] during the light-matter interaction (see Fig. 3.1):

- stimulated emission (carrier depletion (CD)),
- free carrier absorption (FCA), and
- two-photon absorption (TPA).

Stimulated emission results from of an electron-hole recombination in the presence of a stimulating photon. The emitted photon is identical with the stimulating photon in all aspects, i.e., wavelength, direction, polarization and phase. A stimulated recombination in an active material can only occur, if a population inversion is realized. Both, the initial photon as well as the secondarily generated photon give rise to adjacent stimulated carrier recombination, resulting in an amplification of the light injected into the active material.

Since FCABF is a direct interaction of carriers in the bands with the optical wave (plasma-effect), its magnitude is proportional to the concentration of the carriers N and to the photon density S [19].

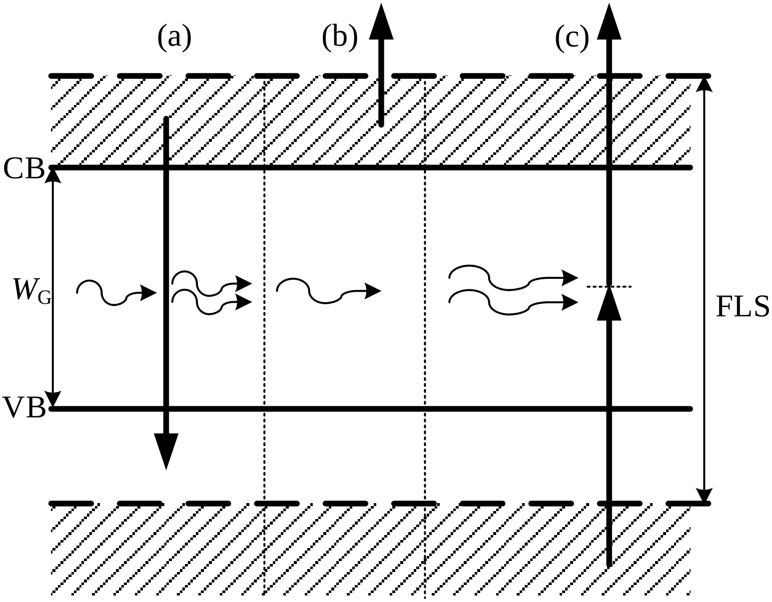

Fig. 3.1. Optically excited radiative transitions in SOAs within the gain spectrum: (a) stimulated emission, (b) free carrier absorption and (c) two-photon absorption.

TPA is a nonlinear process [19, 20] in which the electrons of the VB are excited into the CB by successive absorption of two photons. The process occurs in two steps: the electron reaches a virtual level by absorbing a first photon while a second photon raises the electron into the CB. Therefore, transition rate is proportional to the square of the photon density S^2. However, the TPA gain reduction Δg_{TPA} is proportional to the photon density S as

$$\Delta g_{\text{TPA}} = -\overline{\beta_2} S \, , \tag{3.1}$$

where the TPA coefficient $\overline{\beta_2}$ is measured in m^2. Alternatively, if one uses the light power P instead of S, the TPA coefficient is denoted as β_2 and expressed in cm/GW.

Additionally, spontaneous emission and non-radiative recombination in traps, e.g by Shockley-Read-Hall effects, in Auger processes and through carrier leakage mechanisms [7]. The spontaneous emission is amplified (ASE) and gets relevant for the SOA dynamics.

In the following we explain the SOA carrier dynamics.

3.2.2 Carrier density dynamics

Carrier depletion and recovery are the main processes in the carrier density dynamics. After injecting a light pulse into the SOA, the carrier density $N = N_\mathrm{e} = N_\mathrm{h}$ gets smaller due to the stimulated recombination of electron-hole pairs, and the quasi-Fermi levels change their positions accordingly. By electrical pumping, the carrier density and the quasi-Fermi levels reach their steady state values. This slow process needs about 1 ns for the complete carrier recovery.

3.2.3 Carrier density and energy dynamics

By stimulated emission, ΔN electrons from the CB with energies in a specific range ΔW_p recombine yielding a distortion of the Fermi-Dirac distribution [21] (see Fig. 3.2). The energy domain ΔW_p is broad for short pulses and narrow for long ones.

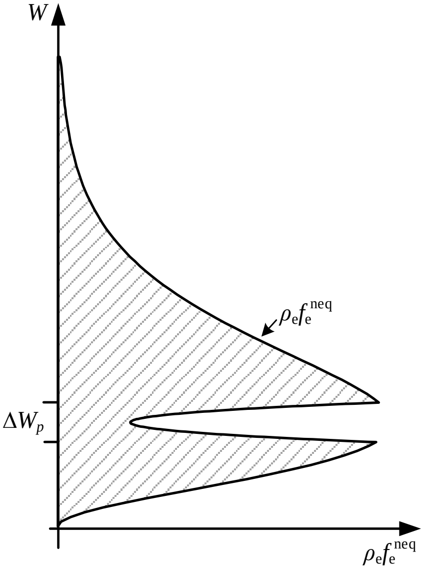

Fig. 3.2. Electron spectral density versus electron energy W *with a hole being burned by stimulated emission.*

For a small photon density S the stimulated emission is weak such that the “spectral” electron density in the energy range ΔW_p is relatively high. In this small-signal regime, the SOA works as a linear amplifier.

If the electrons in the energy domain ΔW_p around the mean CB kinetic energy are strongly depleted by stimulated emission, gain saturation is reached and a spectral hole burning (SHB) process arises [21]. One can see SHB as the formation of a dip in the gain spectrum, occurring by the recombination of electrons and holes at the photon energy, see Fig. 3.2. SHB is a significant local deviation from the Fermi-Dirac distribution at carrier energies corresponding to optical transitions and occurs on a time scale τ_{uf} up to 80 fs.

The creation of a spectral hole has been measured by employing a mode-locked laser at a pulse repetition rate of 10 GHz as pump source. A dip in the optical pump pulse spectrum after the SOA (Fig. 3.3) indicates a high degree of saturation.

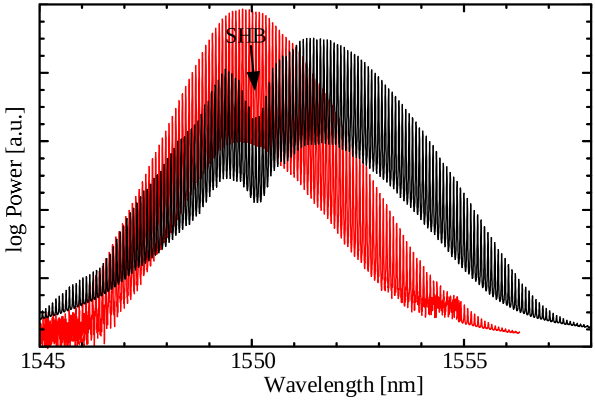

Fig. 3.3. *Pulse spectrum (red curve) before the SOA and pulse spectrum (black curve) after the SOA (biased at* $I = 400\,\mathrm{mA}$ *) for a repetitive sequence of optical pulses with the properties:* $P_{\mathrm{in}} = 12\,\mathrm{dBm}$ *(peak power),* $2.8\,\mathrm{ps}$ *full width at half maximum (FWHM), and* $\lambda_0 = 2\pi c/\omega_0 = 1550\,\mathrm{nm}$ *central wavelength. The pulse repetition frequency is* $f_{\mathrm{rep}} = 10\,\mathrm{GHz}$ *. The powers are differently normalized for both spectra. The pulse spectrum corresponds to the envelope of the traces.*

Carrier heating (CH)

By carrier heating the carrier temperature in the band becomes larger than the lattice temperature [22]. If photon energies are smaller than the FLS but larger than W_{G}, stimulated emission removes cool carriers and heats the distribution. The carrier distribution can additionally be heated by FCA and TPA [23].

Through carrier-carrier scattering these hot carriers give up their excess energy and heat up the rest of the distribution. This effect is called carrier heating. A new “hot” Fermi-Dirac distribution is established, and the carriers get a temperature higher than the lattice. Typical carrier-carrier scattering times are about 80 fs up to 100 fs. Through heating of carriers, the gain of the active semiconductor m edium is reduced.

The “hot” distribution will cool down to the lattice temperature by phonon emission. This effect is called carrier cooling (CC). The corresponding relaxation time, named intraband relaxation time, is in the range from

0.6…1 ps depending on pulse power and length. Cooling the distribution will increase the gain.

While carrier heating describes the installation of a temperature higher than the lattice temperature, carrier cooling is responsible for the return to the lattice temperature. The carrier heating is characterized by gain compression and by an increase of refractive index, while carrier cooling leads to an increase of the gain and a decrease of the refractive index.

Briefly, carrier heating is a consequence of stimulated emission, FCA and TPA. At transparency ($\hbar\omega = \mathrm{FLS}$) and for a pump energy below the bandgap energy ($\hbar\omega < W_\mathrm{G}$), the heating can only occur via FCA and TPA since there are no stimulated transitions [19, 21-23].

Fig. 3.4 shows a qualitative evolution of the carrier density per unit energy, induced by a short pulse in the SOA: Stimulated emission burns a spectral hole, and TPA as well as FCA generate hot carriers. After these processes the carrier distribution recovers via carrier-carrier scattering to a “hot” Fermi-Dirac distribution. The spectral hole gets filled within a time scale of 80…100 fs. In general, the time scale for carrier-carrier scattering is shorter for holes than for electrons and depends on the total carrier density as well as on the pulse duration and power. A further carrier cooling and carrier injection helps to restore the initial Fermi-Dirac distribution [21].

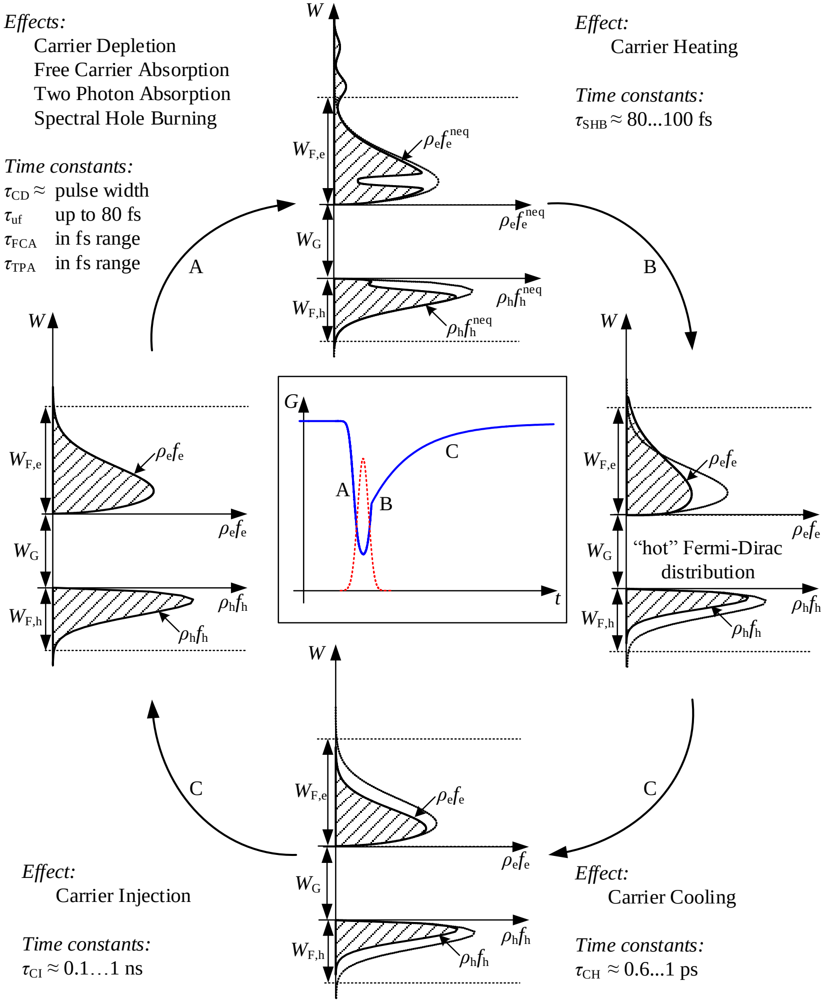

Fig. 3.4. Center image: Temporal gain change (blue curve) of an SOA during and after its excitation by a short pulse. The input pulse is indicated by the red dotted curve. Surrounding images: Corresponding evolution of the carrier density per unit energy.

During and after the pulse-SOA interaction interband and intraband processes occur with different dynamics:

The *slow dynamic effect* is carrier recovery (CR) via electrical pump.

The fast dynamic effects include

- carrier depletion and possibly burning of a spectral hole via stimulated emission,
- instantaneous processes TPA and FCA,
- carrier-carrier scattering (electron-electron scattering), and
- carrier-phonon scattering leading to carrier temperature relaxation.

According to the type of transition, one can distinguish interband and intraband effects:

- *Interband effects* are spontaneous and stimulated emission, TPA and carrier injection by electrical or optical pumping. The effects are associated with changes in carrier density.
- *Intraband effects* are FCA, carrier-carrier scattering (creation of the “hot” carrier distribution and annihilation of the spectral hole) as well as carrier-lattice scattering (leading to carrier cooling). Such effects lead to a change of the energy distribution in the bands without modifying the carrier density ($\Delta N = 0$).

Significance of various processes in SOAs as a function of time

During the propagation of a pulse through an active medium, three main processes occur:

Pulse-SOA interaction

- A short but strong pulse induces carrier depletion via stimulated emission (with formation of a spectral hole for large signals, $\Delta N < 0$), TPA ($\Delta N \gtrsim 0$) and FCA ($\Delta N = 0$).

Carrier heating and relaxation

- The mechanism of heating carriers includes stimulated emission that removes cool carriers from the band, as well as FCA and TPA that create highly energetic carriers in the band. Through carrier-carrier scattering, these hot carriers give up their excess energy and heat the rest of the distribution. The spectral hole vanishes when the "hot" Fermi-Dirac distribution has been realized.

- CC sets in after CH by carrier-lattice scattering. The carrier distribution will cool down, and a Fermi-Dirac distribution at lattice temperature is established. During the relaxation time one can consider the carrier density unchanged ($\Delta N = 0$).

Electrical pumping

- The injection current leads to an increase in carrier density ($\Delta N > 0$) with a constant rate $I/(eV)$.

All the above processes occur during the whole interaction time, while electrical pumping takes place permanently. The relative weight of each process changes in time, resulting in the dynamics of the carrier concentration $N(t)$ and of the energy distribution.

The change of local carrier concentration in the ΔW_p energy domain, see Fig. 3.2, determines the gain dynamics, whereas the change in the whole distribution of carriers defines the refractive index dynamics. The studies of all processes in the active medium of an SOA are especially relevant for short pump pulses. A long pulse can be considered as a sequence of successive short segments. Only the first segment interacts with the medium in the 'ground state', the remaining segments hit the medium in a perturbed status in which the partially ultrafast recovery and/or carrier recovery have already occurred. This explains the difference between the gain dynamics $G(t)$ of the SOA during an interaction with long and short pump-pulses, see Fig. 3.5. By splitting the long pump-pulse into a sequence of short-duration time segments, the gain dynamics results by merging the gain in all segments. Notice that the contributions of various segments are time-delayed with respect to each other. As mentioned at the beginning of this subsection, for long pulses the corresponding ΔW_p is narrow. Therefore, in order to analyze the SOA dynamics, only short pulses are suitable. For long pulses, the interband effects are dominant, not the intraband effects. In contrast, for pulses shorter than the critical value τ_{cr} [24], intraband effects cannot be neglected. Below τ_{cr} the ultrafast nonlinear processes, like spectral hole burning and carrier heating, dominate the gain dynamics. At τ_{cr} the carrier saturation and ultrafast compression contributes equally to the gain reduction.

There is experimental evidence that the 3 dB output saturation energy is smaller for short pulses than for long ones. The 3 dB output saturation energy is the pulse energy at which the SOA gain has been reduced to half of its small-signal value.

For pulses shorter than τ_{cr}, spectral hole burning and carrier heating as well as their relaxation, play an essential role to establish gain saturation. The dynamics of the local carrier density in the energy domain ΔW_p consist of a decrease of carrier number due to stimulated emission and an increase of carrier number through relaxations. Since both processes, carrier depletion and spectrally local recovery occur simultaneously, the 3 dB output saturation energy depends on the pulse length [24].

3.2.4 Rate equation approximation

The carrier density N and the photon density S are not uniformly distributed along the waveguide in the active region of the SOA as the photon number strongly increases by stimulated emission while the carrier density decreases. The optical gain depends therefore on the position within the amplifier.

For taking into account the longitudinal variations of the carrier and photon densities while solving the rate equations, the amplifier is subdivided into Z sections, each of which have uniform carrier and photon densities [14]. Considerable simplifications apply if the intraband relaxation time is neglected. Using this approximation in each section i (with $i = 1,\ldots,Z$) of the SOA, carrier density $N_i(t)$ and photon density $S_i(t)$ dynamics are described by the rate equations,

$$\begin{aligned} \frac{\mathrm{d}N_i}{\mathrm{d}t} &= \frac{I}{eV} - \frac{N_i}{\tau_s} - v_g g_i S_i + \frac{v_g}{2}\frac{\overline{\beta_2} S_i^2}{\Gamma}, \\ \frac{\mathrm{d}S_i}{\mathrm{d}t} &= v_g \Gamma g_i S_i - v_g \alpha_{\mathrm{int}} S_i - v_g \overline{\beta_2} S_i^2, \end{aligned} \tag{3.2}$$

with v_g as the group velocity, τ_s as the carrier lifetime and $v_g \alpha_{\text{int}}$ as the photon lifetime. N_i, S_i and $g_i = g_{\text{m}}\left(N_i, S_i\right)$ represent the carrier and photon densities, and the material gain in the i -th section, respectively. τ_s is determined by the amplified spontaneous emission (ASE) and the non-radiative processes as Auger and Shockley-Read-Hall recombinations, as well as carrier leakage mechanisms. Note the weight factor $1/2$ associated with the carrier density increase due to TPA.

The term $v_g g_i S_i$ corresponds to the depletion of carriers, while $v_g \overline{\beta_2} S_i^2$ represents the TPA term. The depletion becomes larger with increasing i such that it reaches a maximum at the end of the amplifier. The change of carrier density along the SOA leads to changes in the transparency frequency $\omega = \text{FLS}/\hbar$ in the gain spectrum $g_{\text{m}}\left(\omega\right)$ and in its maximum.

With the help of Eqs. (2.15) and (2.26), the explicit dependency of the material gain on carrier and photon densities reads

$$g_i = g_{\text{m}}\left(N_i, S_i\right) = \frac{a_0\left(N_i - N_{\text{tr}}\right)}{1 + \overline{\varepsilon} S_i} \,. \tag{3.3}$$

The rate equations in Eq. (3.2) are usually solved numerically.

3.3 Gain dynamics

The SOA gain, defined in Section 2.3, can be put to a form appropriate for the solution of Eq. (3.2),

$$G_Z\left(t\right) = \exp\left\{\frac{L}{Z}\sum_{i=1}^{Z}\left[\Gamma g_{\text{m}}\left(N_i\left(t\right), S_i\left(t\right)\right) - \overline{\beta_2} S_i\left(t\right)\right] - \alpha_{\text{int}} L\right\}, \tag{3.4}$$

where, for simplicity, we have considered Z sections of equal length L/Z. The higher the number Z of sections the better is the approximation Eq. (3.4) for the SOA power gain. The time dependence of the SOA gain follows from the carrier and photon density dynamics $N\left(t\right)$ and $S\left(t\right)$, respectively. The gain dynamics can be measured in pump-probe experiments, where the probe can be chosen either as a pulse train or as CW.

Considering that a strong pump pulse train and a weak CW probe light are simultaneously launched into an SOA, the probe light is linearly amplified as long as no pump pulse enters the SOA. As soon as a pump pulse enters the

SOA, the SOA gets depleted, i.e., the pulse strongly reduces the carrier density N. The decrease of the number of carriers reduces the gain of the SOA, i.e., the amplification of the probe light. This effect is known as cross-gain modulation (XGM). $P_{\mathrm{CW}}(t)$ follows approximately the dynamics of the average carrier density, $N(t)$, in the SOA. The carrier depletion corresponds to a decrease and the carrier recovery to an increase of the probe output power.

In the case of long pulses, the gain recovery has a weakly ascending slope, while for short pulses below a critical value τ_{cr} [24], the gain recovery curve consists of two segments with differently ascending slopes. The steep slope is associated to the ultrafast recovery, the flat slope corresponds to the slower carrier recovery.

The afore statements can be justified from the experiment in [25], where a data sequence 1011010000 as pump signal is injected together with a CW probe light into an SOA. Fig. 3.5(a) shows the output probe light for short pump pulses (1.8 ps), while Fig. 3.5(b) depicts the output probe light for long pump pulses (8 ps). Note the weight factor $1/2$ associated with the carrier density increase due to TPA.

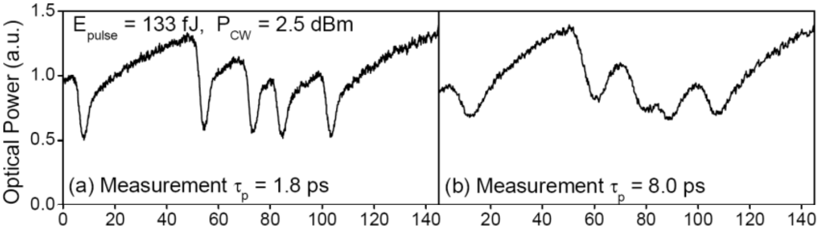

Fig. 3.5. Comparison between experimentally measured [25] cross-gain modulated probe light for pump pulse widths of (a) $1.8\,\mathrm{ps}$ *and (b)* $8\,\mathrm{ps}$.

3.3.1 Gain overshoot

By injecting strong optical pump pulses together with CW probe light into an SOAs, which operates at high bias currents, an increase of the device gain over the steady state value is achieved. This results in a gain overshoot, which can be seen in the output probe light, see Fig. 3.6(a).

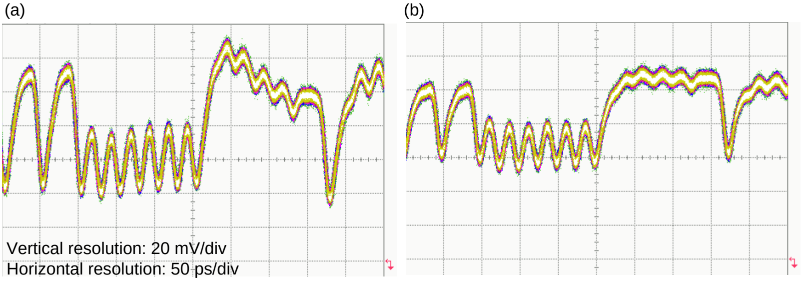

Fig. 3.6. Output probe light power versus time for two SOAs (a) with gain overshoot, (b) without gain overshoot (the gain recovers to a steady state).

The overshoot is explained [26-28] as a result of an inhomogeneous carrier density along the length of the SOA. With increasing CW probe light, which acts as a holding beam in the gain region, the carrier concentration, and thus the gain overshoot, can be reduced.

3.3.2 Gain recovery

The gain recovery time is defined as the time necessary to recover the gain from 10% to 90% of its unsaturated value. It depends on the bias current, the pulse energy and on the probe light power P_{CW}. To shorten this time the bias current can be increased, or a holding beam can be utilized in gain or absorption regimes. The increase of the electrical or optical pump helps, but the use is limited due to the ASE noise and the electrical confinement. Using a holding beam in the gain spectral region, the carrier concentration gets partially saturated since both, the signal and the holding beam, get amplified [27, 29-31]. By reducing the number of carriers with the holding beam, the saturation of the SOA causes a reduction of the pulse amplification. The depletion of the carriers due to the pump pulse is lower, and the SOA can recover faster. The CW probe light acts as a holding beam if its power P_{CW} is comparable to the pulse power P_{in}. Usually, the choice of the holding beam power leads to a trade-off between recovery time and pulse amplification. At transparency $\left(\hbar\omega = \mathrm{FLS}\right)$ the holding beam behaves like an optical pump when the gain spectrum shifts towards smaller energies. It maintains the separation of the quasi-Fermi levels, FLS, and keeps the recovery time of the device constant. The ASE acts as a holding beam in the entire gain region. A wavelength dependency of the gain recovery time has been measured [32].

The experimental results reveal a minimum recovery time at the same wavelength as the peak of gain spectrum, $G = G(\lambda)$.

The recovery time constant has been introduced as a variable parameter to match the measured probe light dynamics [33-35]. The experimentally measured time dependency of the SOA gain has been fitted accordingly to the formula (a and b are fitting parameters)

$$G(t) = \exp\left[a \exp\left(-\frac{t}{\tau_{\mathrm{CI}}} \right) + b \left(1 - \exp\left(\frac{t}{\tau_{\mathrm{delay}}} \right) \right) \exp\left(-\frac{t}{\tau_{\mathrm{SHB}}} \right) \right], \tag{3.5}$$

where τ_{SHB} is the recovery time constant for the ultrafast carrier-carrier scattering which fills the spectral hole, and τ_{CI} is the recovery time constant for the carrier recovery. τ_{delay} denotes the time interval between the arrival of the pulse and the onset of ultrafast recovery. The recovery time constant depends on the bias current but not on the length of the SOA.

3.4 Refractive index dynamics

3.4.1 Theory

The complex refractive index $\underline{n}(\omega)$ can be defined (see also Eq. (1.7)) as

$$\underline{n}(\omega) = \sqrt{1 + \underline{\chi}^{(1)}(\omega)}\,. \tag{3.6}$$

Being the Fourier transform of a causal influence function, the linear susceptibility $\underline{\chi}^{(1)}(\omega)$ is an analytic function in a domain of the complex angular frequency plane (Titchmarsh's theorem [36, p. 28]). As the square root of an analytic function remains analytic, $\underline{n}(\omega)$ is also an analytic function. Following Eq. (1.8) we can express $\underline{n}(\omega)$ as

$$\underline{n}(\omega) = n(\omega) - \mathrm{j} n_i(\omega), \quad n_i(\omega) = \frac{c}{2\omega} a(\omega)\,. \tag{3.7}$$

The analytic function $\underline{n}(\omega)$ can be made single-valued by requiring

$$\lim_{\omega \to \infty} n(\omega) = 1\,. \tag{3.8}$$

Assuming that certain conditions [12, pp. 372,373] for the modulus $\left|\underline{n}(\omega)\right|$ are fulfilled, the real and imaginary parts of $\underline{n}(\omega)$ form a Hilbert pair, i.e., they are interconnected by the Hilbert transforms

$$n(\omega)-1=\frac{1}{\pi}\mathbb{P}\int_{-\infty}^{\infty}\frac{n_i(\omega')}{\omega'-\omega}\mathrm{d}\omega'=\frac{1}{\pi}\int_{-\infty}^{\infty}\frac{n_i(\omega')-n_i(\omega)}{\omega'-\omega}\mathrm{d}\omega' \tag{3.9}$$

and

$$n_i(\omega)=-\frac{1}{\pi}\mathbb{P}\int_{-\infty}^{\infty}\frac{n(\omega')-1}{\omega'-\omega}\mathrm{d}\omega'=-\frac{1}{\pi}\int_{-\infty}^{\infty}\frac{n(\omega')-n(\omega)}{\omega'-\omega}\mathrm{d}\omega', \tag{3.10}$$

where $\mathbb{P}$ denotes the Cauchy principal value. The second form of the chained Eqs. (3.9) and (3.10) are obtained by taking advantage of the identity [37],

$$\mathbb{P}\int_{-\infty}^{\infty}\frac{\mathrm{d}\omega'}{\omega'-\omega}=0, \tag{3.11}$$

and by assuming $\mathrm{d}\underline{n}(\omega)/\mathrm{d}\omega$ finite. In Eqs. (3.9) and (3.10), the integrand, singular at $\omega'=\omega$ in the first form, has been replaced by a derivative at $\omega'=\omega$ in the second form. Having removed the singularity at $\omega'=\omega$, one can omit the symbol $\mathbb{P}$.

Being the Fourier transform of a real-valued function, the susceptibility $\underline{\chi}^{(1)}(\omega)$ satisfies (see Eq. (1.5)) also

$$\underline{\chi}^{(1)*}(\omega)=\underline{\chi}^{(1)}(-\omega). \tag{3.12}$$

By analyzing Eq. (3.6), one can show that the relation extends to the nonlinear case, $\underline{n}^*(\omega)=\underline{n}(-\omega)$. Subsequently, the real and imaginary parts satisfy

$$n(-\omega)=n(\omega) \text{ and } n_i(-\omega)=-n_i(\omega). \tag{3.13}$$

Note that $n_i(\omega)$ is represented by an odd function of the angular frequency, whereas the (real) refractive index $n(\omega)$ and the absorption coefficient $a(\omega)$ are even functions.

With the help of Eq. (3.13) one can reformulate the Hilbert transforms in Eqs. (3.9) and (3.10) as

$$n(\omega)=1+\frac{2}{\pi}\int_0^\infty\frac{\omega' n_i(\omega')-\omega n_i(\omega)}{\omega'^2-\omega^2}\mathrm{d}\omega' \tag{3.14}$$

and

$$n_i(\omega)=-\frac{2\omega}{\pi}\int_0^\infty\frac{n(\omega')-n(\omega)}{\omega'^2-\omega^2}\mathrm{d}\omega' , \tag{3.15}$$

respectively.

In Eqs. (3.14) and (3.15) one can replace the imaginary part $n_i(\omega)$ by the absorption coefficient $a(\omega)$, or by the gain coefficient $g(\omega)=-a(\omega)$, according to

$$n_i(\omega)=-\frac{c}{2\omega}g(\omega), \tag{3.16}$$

in which case the Hilbert transformations are usually called the Kramers-Kronig relations. They are expressed as

$$n(\omega)=1-\frac{c}{\pi}\int_0^\infty\frac{g(\omega')-g(\omega)}{\omega'^2-\omega^2}\mathrm{d}\omega' \tag{3.17}$$

and

$$g(\omega)=\frac{4\omega^2}{\pi c}\int_0^\infty\frac{n(\omega')-n(\omega)}{\omega'^2-\omega^2}\mathrm{d}\omega' . \tag{3.18}$$

As causality also holds for nonlinear systems, one can examine under what conditions the Kramers-Kronig relations apply in nonlinear optics. By viewing the material in the presence of a perturbation (e.g., a strong light beam) as a new linear system, one can apply causality and the linear Kramers-Kronig relations. Since the Kramers-Kronig relations apply in the absence of the perturbation, they will also apply to the refractive index and gain differences, Δn and Δg, between the perturbed and unperturbed systems. One can thus write [10, 37]

$$\Delta n(\omega,\zeta) = -\frac{c}{\pi}\int_{0}^{\infty}\frac{\Delta g(\omega',\zeta)-\Delta g(\omega,\zeta)}{\omega'^{2}-\omega^{2}}\mathrm{d}\omega', \tag{3.19}$$

where ζ denotes the perturbation, which must be held constant as ω' is varied.

This equation can be applied to resonant and non-resonant optical nonlinearities as long as the optical perturbation is another field. Since the perturbation must remain constant over the integration, the applicability of Eq. (3.19) is restricted to nondegenerate optical nonlinearities, e.g., to pump-probe experiments with the pump at a fixed frequency.

For nonlinear processes, it is easier to relate the dynamics of the refractive index n and the gain coefficient g by α-factors. An α-factor expresses the ratio between the change of refractive index and the change of gain as functions of the carrier density N, the temperature T or the photon intensity S,

$$\alpha_{\mathrm{BF}} = -\frac{4\pi}{\lambda}\frac{\frac{\partial n}{\partial N}}{\frac{\partial g}{\partial N}}, \quad \alpha_{\mathrm{CH}} = -\frac{4\pi}{\lambda}\frac{\frac{\partial n}{\partial T}}{\frac{\partial g}{\partial T}}, \quad \alpha_{\mathrm{TPA}} = -\frac{4\pi}{\lambda}\frac{\frac{\partial n}{\partial S}}{\frac{\partial g}{\partial S}}. \tag{3.20}$$

α_{BF} is often denoted by α_{N}. Each α-factor is frequency dependent and can be positive or negative [35, 38]. As there is a variation of the spectral gain change with position and time, the refractive index will also depend on this position and time, respectively. Nevertheless, it is assumed that the α-factors are constant. This holds for variations of N, T and S which are not too large.

At the beginning of Section 2.4 we have shown how to consider $\mathrm{FCA_{BF}}$ in the BF gain contribution. By employing the Kramers-Kronig relation on this modified BF gain, the refractive index change associated to BF also includes the free carrier index (FCI) change.

Knowing the value of α_{BF}, the first equation in Eq. (3.20) can be used with the modified BF gain to find the BF refractive index change which includes the FCI change.

We now comment on the definition of α_{TPA} (see third equation in Eq. (3.20)). $\partial n/\partial S$ is proportional to the conventional Kerr coefficient n_2 for the intensity-induced change in the refractive index

$$\frac{\partial n}{\partial S} = \hbar\omega v_g n_2 \,. \tag{3.21}$$

By using the TPA gain reduction, Eq. (3.1), one obtains

$$\alpha_{\text{TPA}} = \frac{4\pi}{\lambda}\frac{\hbar\omega v_g n_2}{\bar{\beta}_2} \,. \tag{3.22}$$

From the reported values $\bar{\beta}_2 = 3.8\times10^{-21}\,\text{m}^2$, $v_g = 8.45\times10^7\,\text{m/s}$ and $n_2 = -1.3\times10^{-16}\ \text{m}^2/\text{W}$, the value $\alpha_{\text{TPA}} = -3$ at $\lambda = 1.55\,\mu\text{m}$ results.

We will see in chapter 4 that the observed strong decrease of the refractive index cannot be explained based only on the TPA effect with $\alpha_{\text{TPA}} = -3$. An important contribution is from the excitation of TPA-produced electrons in the CB by free carrier absorption (FCA$_{\text{TPA}}$ effect). Denoting by N_{FCA} the density of the FCA$_{\text{TPA}}$-excited electrons and by m_{FCA} their effective mass, the decrease of the refractive index Δn_{FCA} can be obtained from the Drude formula, Eq. (2.30) by replacing N_e/m_e with $N_{\text{FCA}}/m_{\text{FCA}}$ and by setting $N_h = 0$. On the other hand, Δn_{FCA} can be expressed in terms of the FCA cross-section σ_{FCA} and the (negative) alpha factor α_{FCA}, see Eq. (A.2) and the first formula in Eq. (A.5). By equating the two expressions for the change in the refractive index one finds the relation

$$m_{\text{FCA}}\left|\alpha_{\text{FCA}}\right| = \frac{e^2\lambda}{2\pi\varepsilon_0 c^2 n_0 \sigma_{\text{FCA}}} \,. \tag{3.23}$$

for an SOA operating at the wavelength λ. By substituting $n_0 = 3.47$ from [10], $\lambda = 1.55\,\mu\text{m}$ and $\sigma_{\text{FCA}} = 10^{-20}\ \text{m}^2$, as suggested in Appendix A, the right-hand side of Eq. (3.23) amounts 25% of the free electron mass $m_0 = 9.109\times10^{-31}\ \text{kg}$.

With the conditions $\alpha_{\mathrm{FCA}} \gg 7.6$ derived in Appendix A for a negligible FCA-coefficient, one obtains $m_{\mathrm{FCA}} \ll 0.03 m_0$. The value of the FCA_{TPA} excited electron effective mass is thus significantly smaller than the electron effective mass m_e at the minimum of the lowest conduction band, e.g., $m_e = 0.04685 m_0$ for $\mathrm{Ga_{0.4}In_{0.6}As_{0.85}P_{0.15}}$ as reported in [10].

We conclude this subsection by emphasizing that the probability of direct absorption of one photon for $\mathrm{FCA_{TPA}}$ is several orders higher than in the $\mathrm{FCA_{BF}}$ effect.

3.4.2 Experimental methods for the study of the refractive index dynamics

A pulse propagating in z direction inside of an SOA is described by the electric field

$$\vec{E} = E_0(z,t)\frac{1}{2}\left\{\exp\left[\mathrm{j}\phi(z,t)\right] + \mathrm{c.c.}\right\}\vec{\mathrm{e}}_y\,, \tag{3.24}$$

where $E_0(z,t)$ is the real-valued field envelope and $\vec{\mathrm{e}}_y$ the polarization direction (taken here along the y-axis). $\phi(z,t)$ is the complete phase consisting of the plane wave phase and the phase shift $\varphi(z,t)$,

$$\phi(z,t) = \omega_0 t - \frac{2\pi}{\lambda_0} n_0 z + \varphi(z,t) \tag{3.25}$$

with $\omega_0 = 2\pi f_0 = 2\pi c/\lambda_0$ the central angular frequency of the pulse, n_0 the effective refractive index and $2\pi n_0/\lambda_0$ the effective propagation constant.

By neglecting for simplicity the guided propagation, the phase $\phi(z,t)$ becomes linear in z. A time dependent refractive index $n(t)$ can be defined according to

$$\frac{\partial}{\partial z}\phi(z,t) = -\frac{2\pi}{\lambda_0} n(t)\,. \tag{3.26}$$

By substituting the expression of the complete phase, Eq. (3.25), in the left hand side of Eq. (3.26), one obtains

$$\frac{\partial}{\partial z}\varphi(z,t)=-\frac{2\pi}{\lambda_0}\left[n(t)-n_0\right]. \tag{3.27}$$

For convenience of notation, we set $z=L$ with L as the SOA length, and write $\varphi(t)=\varphi(L,t)$ and $\Delta n(t)=n(t)-n_0$. The dynamics of the refractive index change $\Delta n(t)$ is related to the measured probe light phase shift $\varphi(t)$ by

$$\varphi(t)=-\frac{2\pi}{\lambda}L\Delta n(t). \tag{3.28}$$

From the definition of the instantaneous frequency, we obtain

$$\begin{aligned} f(t)&=\frac{1}{2\pi}\frac{\mathrm{d}}{\mathrm{d}t}\phi(L,t)= f_0+\Delta f(t)\\ &= f_0+\frac{1}{2\pi}\frac{\mathrm{d}}{\mathrm{d}t}\varphi(t)= f_0-\frac{L}{\lambda_0}\frac{\mathrm{d}}{\mathrm{d}t}n(t). \end{aligned} \tag{3.29}$$

For $\Delta\varphi(t)/\Delta t>0$, i.e., $\Delta n>0$, the instantaneous frequencies become smaller, leading to a spectral red-shift. In contrast, for $\Delta\varphi(t)/\Delta t<0$, i.e., $\Delta n<0$, the instantaneous frequency increases, yielding a spectral blue-shift. The change in time of the instantaneous frequency is named chirp.

3.4.3 Phase modulation

Techniques for the phase shift $\varphi(t)$ measurements are described below:

- An interferometric arrangement used in a pump-probe experiment enables measurements of pump-induced refractive index changes in the SOA. The refractive index change causes a phase shift of the probe pulse which can be measured with a third pulse, a reference pulse [39]. The probe phase shift is measured as a function of a pump-probe time delay.
- Time-resolved frequency chirp measurements at the output probe signal are used to calculate the phase shift as a function of time. This can be obtained by integrating over the measured chirp, i.e., the second derivative of the phase with time.

Techniques for simultaneous phase and gain dynamics measurements are:

- Both gain and phase functions are calculated from spectrograms [40-43]. The time-resolved complex transmission function is determined by the frequency resolved optical gating (FROG) technique or the frequency resolved electro-absorption gate (FREAG) technique, respectively. Measurements based on the FREAG technique will be presented in chapter 4 and 6.
- Simultaneous measurement of the dynamics of gain and refractive index in an optically excited SOA are performed using a terahertz optical asymmetric demultiplexer (TOAD) loop [33-35]. The reflection and transmission results of the probe light are used to determine the gain $G(t)$ and refractive index $n(t)$.

Cross-phase modulation (XPM)

The injection of a pump pulse together with a probe light into an SOA induces a time dependent modification of the refractive index in the active medium. As a consequence, the probe light phase is correspondingly modulated. This effect, called cross-phase modulation, is responsible for the broadening of the probe light spectrum. Considering only a band filling process inside the SOA, the carrier density decreases $(\Delta N < 0)$ during depletion while the refractive index increases $(\Delta n > 0)$. The instantaneous frequencies will have smaller values than the center frequency of the CW probe light ω_{CW}, and a red-shifted spectral component is created in the spectrum of the probe light. When the carrier recovery dominates $(\Delta N > 0)$, the refractive index decreases $(\Delta n < 0)$, and the instantaneous frequencies get larger than ω_{CW}. This process generates a blue-shifted component. Hence the probe light gets a red-shifted sideband during the depletion and a blue-shifted sideband during the recovery process.

For pulses longer than the critical value τ_{cr}, the ultrafast effects can be neglected. The XPM causes a shift of the probe spectral components first to longer (red-shifting) and then to shorter wavelengths (blue-shifting).

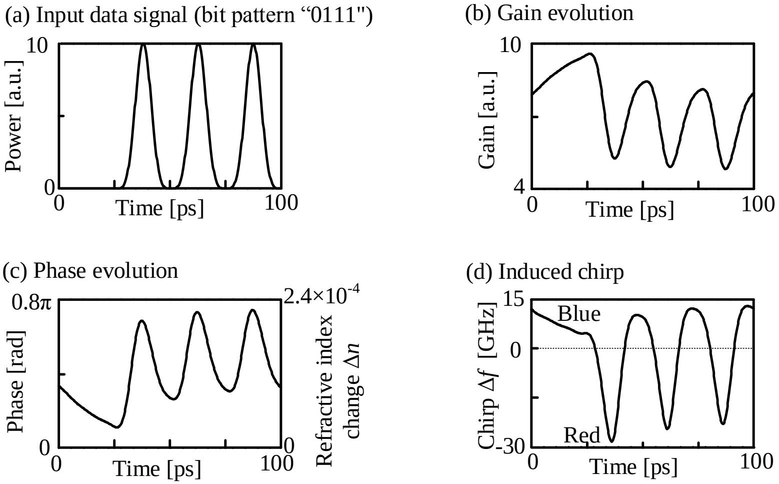

Fig. 3.7. Schematic diagram of (a) input pulses, (b) SOA gain modulation, (c) probe light phase modulation and refractive index evolution, (d) probe light induced chirp.

Fig. 3.7 shows the time evolution of the input pulse sequence, the dynamic SOA gain, the induced phase shift and the chirp. For simplicity we ignore the delay of the SOA gain with respect to the pulse peak.

Fig. 3.8 shows the spectrum of the probe light after the SOA in a pump-probe experiment using a 10 GHz clock signal from a mode-locked laser source. The spectrum is considerably broadened and displays a three-sideband structure, one strong red-shifted and two blue-shifted components.

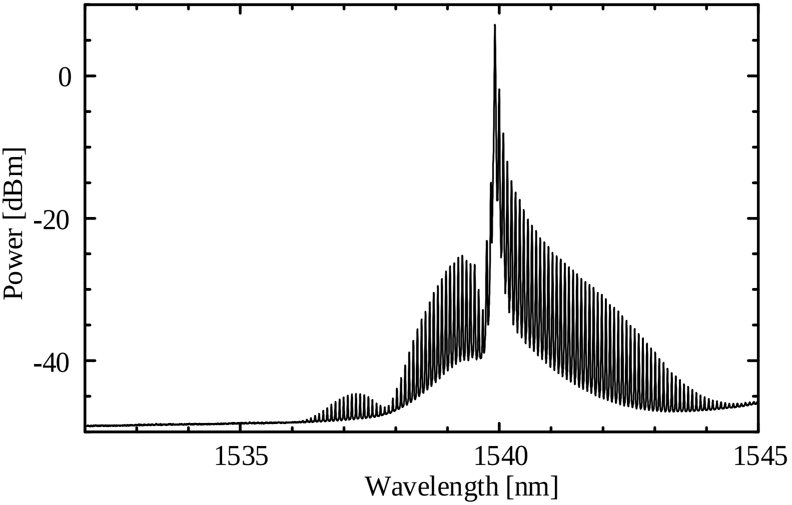

Fig. 3.8. *Probe light spectrum after the SOA (biased at* $I = 900\,\mathrm{mA}$*) for a repetitive sequence of optical pump pulses. The pump pulse power is* $P_{\mathrm{in}} = 12.5\,\mathrm{dBm}$ *at a center wavelength of* $\lambda_0 = 1550\,\mathrm{nm}$*. The pulse repetition frequency is* $f_{\mathrm{rep}} = 10\,\mathrm{GHz}$ *for pulse of* $2.8\,\mathrm{ps}$ *FWHM. The probe light power is* $P_{\mathrm{CW}} = 10\,\mathrm{dBm}$ *at a wavelength of* $\lambda_{\mathrm{CW}} = 1540\,\mathrm{nm}$*. The spectrum corresponds to the envelope of the traces.*

The time dependency of instantaneous frequencies gives information about the probe light phase shift $\varphi(t)$ and about the refractive index change $\Delta n(t)$ of the SOA. Measuring a spectrum with an optical spectrum analyzer (OSA) corresponds to an integration of the incoming photons in a certain spectral domain over equally long time intervals. Therefore, the probe light spectrum gives no information on the chronological order of the refractive index changes, which means that the sequence of spectral components is unknown.

This limited information coming from a probe light spectrum can be improved by a spectral analysis of the pulse after the SOA, see Chapter 4.

Self-phase modulation (SPM)

The pulse itself acts as probe light such that the output pulse spectrum gets modified. The gain and refractive index nonlinearities lead to a pulse distortion as the leading pulse edge produces gain saturation. Therefore, both gain and refractive index of the SOA get modified, and subsequently the trailing edge of the pulse is influenced. The pulse spectrum can be considerably distorted, if the refractive index suffers a relatively large modification.

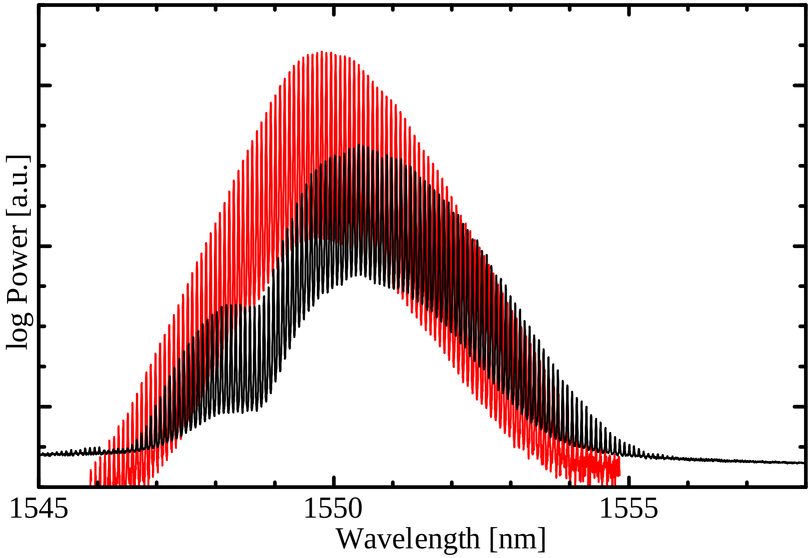

Fig. 3.9. *Pulse spectrum (red curve) before the SOA and pulse spectrum (black curve) after the SOA (biased at* $I = 400\,\mathrm{mA}$ *) for a repetitive sequence of optical pulses with the properties:* $P_{\mathrm{in}} = 0\,\mathrm{dBm}$ *,* $2.8\,\mathrm{ps}$ *FWHM,* $\lambda_0 = 1550\,\mathrm{nm}$ *. The pulse repetition frequency is* $f_{\mathrm{rep}} = 10\,\mathrm{GHz}$ *. The powers are differently normalized for both spectra. The pulse spectrum corresponds to the envelope of the traces.*

The SPM-induced spectral broadening in Fig. 3.9 shows a dominant peak shifted towards red with respect to the input spectrum as well as a weak blue-shifted peak.

XPM and SPM processes will be analyzed in more detail in chapter 4.

3.4.4 Nonlinear polarization rotation

In this section we explain how the polarization of an incident signal is rotated in an SOA by the 'nonlinear polarization rotation'.

Light propagating in an SOA can be decomposed into a transverse electric (quasi-TE) and a transverse magnetic (quasi-TM) mode (mutually orthogonal polarized), see Fig. 3.10. Generally, both modes sense different SOA power gain values G_{TE} and G_{TM}, and different refractive indices n_{TE} and n_{TM}, leading to a rotation of the polarization of the light [44, 45]. The absolute value of the difference between G_{TE} and G_{TM} is called polarization sensitivity and is denoted by

$$\Delta G_{\mathrm{TE/TM}} = \left| G_{\mathrm{TE}} - G_{\mathrm{TM}} \right| . \tag{3.30}$$

There are two reasons for the different gain for TE and TM modes in a bulk SOA. The first reason is the difference between the confinement factors of the TE and TM mode, while the second reason is the different material gain for TE and TM in the case of gain saturation.

Since a strong pump signal saturates the active region of both modes, the mode with the larger confinement factor experiences a larger gain, while the other one has a weaker amplification. By choosing a square cross-section of the active medium, the confinement factors for TE and TM can be made equal.

The modes propagate independently through the SOA, although they have an indirect interaction with each other via the gain saturation. The TE and TM gains couple different hole reservoirs, i.e., for light holes (lh) and heavy holes (hh), to a single electron reservoir of the SOA. For unstrained bulk SOAs, the transitions for electrons from CB to the lh-VB and to the hh-VB are fully symmetric for TE and TM fields.

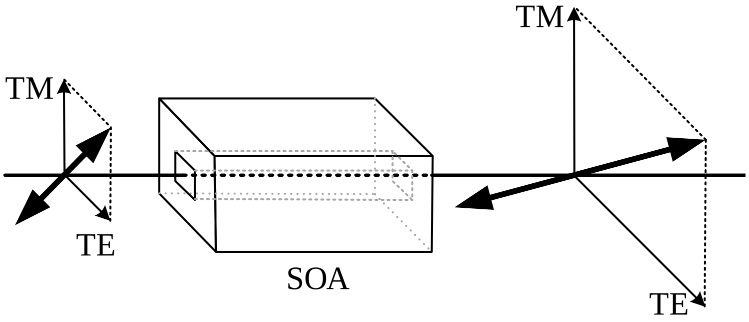

Fig. 3.10. Different amplifications of TE and TM modes leading to a polarization rotation.

In strained bulk SOAs the material gain coefficients for TE and TM polarizations are different, $g_{\mathrm{m,TM}} \neq g_{\mathrm{m,TE}}$. Different SOA gains for TE and TM polarizations give rise to different refractive indices $n_{\mathrm{TE}} \neq n_{\mathrm{TM}}$, which in turn are responsible for the relative phase shift

$$\varphi_{\mathrm{TE/TM}} = \frac{2\pi L}{\lambda}\left|n_{\mathrm{TE}} - n_{\mathrm{TM}}\right| . \tag{3.31}$$

This phase shift between TE and TM mode of the probe light is called cross-phase polarization. It increases with the power of the pump pulse [45]. The effect of different amplification for TE and TM modes of the probe light is called cross-gain polarization.

3.5 Correlation between gain and refractive index dynamics

3.5.1 Ultrafast refractive index dynamics

Experiments with very short strong pump pulses of 100 fs up to 440 fs [19, 20, 46] show an instantaneous decrease of the refractive index at the beginning of the interaction in the SOA. This refractive index decrease, measured with a probe light, is independent on the operation regime of the SOA, i.e., absorption, transparency or gain regime. By adjusting the center wavelength of the pump pulse to the transparency point of the SOA, stimulated absorption and emission balance, and therefore the carrier density is not affected by the pump pulse. Here, the measurement of the incipient instantaneous decrease of the refractive index is only attributed to TPA and FCA.

In [43] the refractive index decrease was measured for a 3 ps pulse.

3.5.2 Dynamics of gain and phase in an SOA

Time delay Δt_d

The dynamics of the gain and refractive index in an optically excited SOA, measured using spectrograms [40, 41, 43] and a picosecond pump-probe arrangement [34], shows a delay between the maximum of the refractive index and the minimum of the amplitude, see Fig. 3.11. This delay Δt_d depends on the pulse width of the input pulses. Measurements have shown a time delay of $\Delta t_\mathrm{d} \approx 2\,\mathrm{ps}$ for pulses of 3 ps FWHM and $\Delta t_\mathrm{d} \approx 5\,\mathrm{ps}$ for pulses of 20 ps FWHM. This makes clear that gain and phase response are not linearly related as implied by the constant Henry factor concept. To overcome this deficiency a time dependent α -factor has been introduced by J. Wang et al. [43].

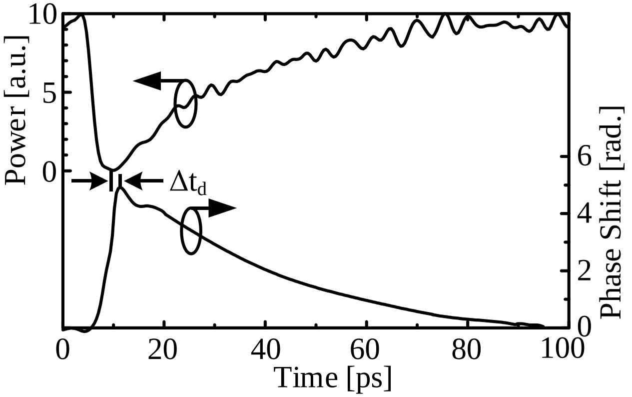

Fig. 3.11. Simultaneous measurements [43] of power and phase of the output probe light which describe the gain and refractive index dynamics.

Phase change at ultrafast gain recovery

Observations have confirmed that the ultrafast contribution to the gain recovery dynamics of an optically excited SOA has no counterpart in the phase dynamics.

Gain and refractive index recovery dynamics in SOAs differ in two aspects:

- the absence of the ultrafast component in the refractive index and
- the time delay Δt_d between the maximum of the gain compression and the maximum of the refractive index.

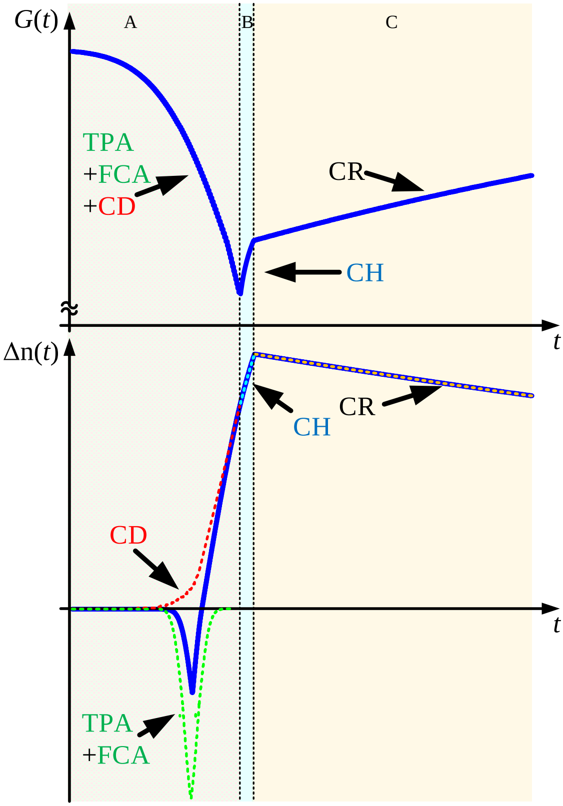

Fig. 3.12. A simplified scheme of gain and refractive index dynamics of an SOA indicating predominant physical effects. The total refractive index (blue curve) is the sum of all contributions.

We explain the gain and refractive index dynamics using a simplified scheme, see Fig. 3.12. The whole time interval is split into three segments A, B and C.

The gain reduction, consisting of carrier depletion and ultrafast gain compression, is the main effect in segment A. The ultrafast gain recovery during CH is depicted in segment B. Segment C shows carrier cooling and carrier recovery.

In the next subsection we will describe the change in the gain coefficient Δg and in the refractive index Δn within these time segments.

Evolution of gain and refractive index

Gain depletion

During the interaction of the pump pulse with the SOA, FCA and TPA accompany the CD by suppressing the gain, i.e., $\Delta g < 0$. While CD leads to an increase of refractive index $\Delta n > 0$, both FCA and TPA are responsible for its decrease. Carriers generated by TPA or excited by FCA are assumed to make a negligible contribution to the gain in the active region. SHB will not change the refractive index because of the approximate symmetry of Δg around the central angular frequency ω [35], see Eq. (3.19). At the angular frequency ω, the gain compression is at maximum, i.e. $\mathrm{d}g(\omega')/\mathrm{d}\omega'\big|_{\omega'=\omega} = 0$.

The main features of the gain and index dynamics are summarized in tabular form:

	CD	SHB	CH	TPA	FCA ($\mathrm{FCA_{BF}}$+$\mathrm{FCA_{TPA}}$)
Gain	$\Delta g_{\mathrm{CD}} < 0$	$\Delta g_{\mathrm{SHB}} < 0$	$\Delta g_{\mathrm{CH}} < 0$	$\Delta g_{\mathrm{TPA}} < 0$	$\Delta g_{\mathrm{FCA}} < 0$
Refractive index	$\Delta n_{\mathrm{CD}} > 0$	$\Delta n_{\mathrm{SHB}} \approx 0$	$\Delta n_{\mathrm{CH}} > 0$	$\Delta n_{\mathrm{TPA}} < 0$	$\Delta n_{\mathrm{FCA}} < 0$
α -factor	$\alpha_{\mathrm{BF}} > 0$	$\alpha_{\mathrm{SHB}} \approx 0$	$\alpha_{\mathrm{CH}} > 0$	$\alpha_{\mathrm{TPA}} < 0$	$\alpha_{\mathrm{FCA}} < 0$

The probability of stimulated emission is orders of magnitude larger than the probability of FCA or TPA. The stimulated emission of photon of $0.8\,\mathrm{eV}$ removes the cool carriers, i.e., the electrons and holes of a few meV above and respectively below the bandgap [20], and leaves carriers of higher energies in the distributions. In this way stimulated emission leads to heating of the carriers [22]. Each FCA or TPA event changes the total energy of the distribution by the single photon energy of $0.8\,\mathrm{eV}$ (for $\lambda = 1550\,\mathrm{nm}$) in the case of FCA, or by $1.6\,\mathrm{eV}$ for TPA. On the other hand, TPA and FCA have contributions to carrier heating proportional to their respective transition probabilities. Note that the effects, i.e., FCA, TPA, CD, carrier-carrier scattering, carrier-lattice scattering, and CR can occur simultaneously. If the effects can be considered independent, the total change in the refractive index is equal to the sum of their individual contributions. This property remains true for gain contributions because of the linearity of the Kramers-Kronig relations. By assuming that TPA, FCA, CD and SHB are the main effects occurring in time segment A, one immediately concludes a strong gain suppression. The lowest value of the SOA gain corresponds to the maximum SHB. Since the various contributions to the refractive index have opposite signs, the corresponding effects might even completely cancel.

Even though the probability for FCA and TPA is low, both effects have a significant impact on the interaction of short but strong optical pulses with the active material. This holds true especially at the beginning of the pulse, where FCA and TPA might suppress – and at certain times even overcompensate – the increase of the refractive index, see Fig. 3.12. $\mathrm{FCA}_{\mathrm{TPA}}$ is delayed with respect to TPA, see Appendix A.

Ultrafast Gain Recovery

After reaching its minimum, the SOA gain starts recovering immediately. The spectral hole fills during the CH process. This intraband process is accompanied by an increase in gain ($\Delta g > 0$) and in refractive index ($\Delta n > 0$). The gain increases due to the installation of the “hot” Fermi-Dirac distribution. As the distribution heats up, the refractive index increases.

Gain Recovery

The intraband carrier cooling (CC) as well as the slow increase of the carrier density ($\Delta N > 0$) due to CR change the gain ($\Delta g > 0$) and the refractive index ($\Delta n < 0$).

	CC	CR
Gain	$\Delta g_{\mathrm{CC}} > 0$	$\Delta g_{\mathrm{CR}} > 0$
Refractive index	$\Delta n_{\mathrm{CC}} < 0$	$\Delta n_{\mathrm{CR}} < 0$
α -factor	$\alpha_{\mathrm{CH}} > 0$	$\alpha_{\mathrm{BF}} > 0$

In Ref. [43], the SOA dynamics were discussed in terms of the SOA gain $G(t)$ and of the probe light phase shift $\varphi(t)$. The relative weights of the constituting processes change in time and determine the dynamics of both $G(t)$ and $\varphi(t)$ as well as their relation which can be encoded in the effective time-dependent α -factor, $\alpha_{\mathrm{eff}}(t)$,

$$\alpha_{\mathrm{eff}}(t) = 2\frac{\frac{\mathrm{d}}{\mathrm{d}t}\varphi(t)}{\frac{\mathrm{d}}{\mathrm{d}t}\left[\ln G(t)\right]}. \tag{3.32}$$

The time delay Δt_{d} between the minimum of the gain and the maximum of the refractive index has its origin in the intraband relaxation of the spectral hole during CH.

Both, TPA and FCA processes occur only for high pulse power. For weak pump pulses and short SOAs, where the amplification is small, the dominant process is CD. For strong pulses or when the SOA is long enough to produce significant amplification, the effects CH, SHB, TPA and FCA significantly contribute to gain reduction and refractive index change.

During the ultrafast gain recovery, the refractive index continues to increase. Since the refractive index decrease starts a time a time Δt_{d} later then the gain recovery, the refractive index appears to recover faster than the gain [47]. The correlation between the gain and refractive index dynamics and the output pulse shape and phase is discussed in Appendix A.

3.6 Summary

In order to find good operating parameters for an SOA, it is important to know the gain and the phase dynamics. These dynamics evolve differently for long and short pulses with respect to a critical temporal width τ_{cr}. For long pulses the dynamics of the gain and refractive index in the SOA can be related with a single α -factor, except for the time interval Δt_{d} between the gain minimum and the maximum of the refractive index. This time delay and the fact that the refractive index recovers faster than the gain, are both explained by the intraband relaxation of the spectral hole through CH.

For short input pulses the intraband and interband effects have almost the same importance. For short strong input pulses, the gain cannot be related to the refractive index by a single α -factor.

The high-speed switching dynamics of all-optical devices incorporating SOAs is mainly determined by the carrier density dynamics. The carrier recovery limits the available operating bandwidth. Solutions for mitigating this limitation are shown in chapter 5.

4 Measurement and modeling of optical spectra

4.1 Introduction

The refractive index modulation $\Delta n(t)$, induced by a pump pulse inside an SOA, leads to a cross-phase modulation (XPM) of the probe light and to a self-phase modulation (SPM) of the pump pulse.

As high-speed optical networks employ short optical pulses, the analysis of the SOA response to these pulses is important. Therefore, probe light spectra have been measured for different operating points with respect to the pump and probe light power, the probe wavelength as well as the applied bias current.

The goal of these measurements is to associate with each spectral component a process contributing to the SOA dynamics. This is required for practical applications utilizing optical filters, which select specific spectral domains. The refractive index dynamics is reflected by the probe light spectrum. Spectral measurements of pump and probe light allow to focus on one out of two different models [25, 48] regarding the refractive index dynamics during the interaction of a pump pulse with the SOA.

For clarifying the underlying physics, we propose an analytical model for a pump-probe experiment and compare the calculated and measured spectra in order to find the nonlinear SOA parameters.

4.2 Experimental setup and measurements

The experimental setup is shown in Fig. 4.1. A mode-locked laser generating pulses with 2.8 ps FWHM at a wavelength of 1550 nm was chosen as the pump pulse source. The pulse repetition rate was 10 GHz. The pump power P_{in} was varied between 0 dBm and 12 dBm, while the probe power P_{CW} is fixed between 0 dBm and 10 dBm. The probe wavelength was chosen in the range between 1535 nm and 1560 nm. The 2.6 mm long bulk SOA showed an almost polarization-independent amplification. The bias current I was varied between 150 mA and 900 mA. At the lower current limit, a gain recovery time of 75 ps was measured. The spectra were recorded using an optical spectrum analyzer (OSA).

Using a 3 dB coupler, pump and probe light were injected in co-propagation direction into the SOA. The CW light was TE linearly polarized in the SOA layer plane.

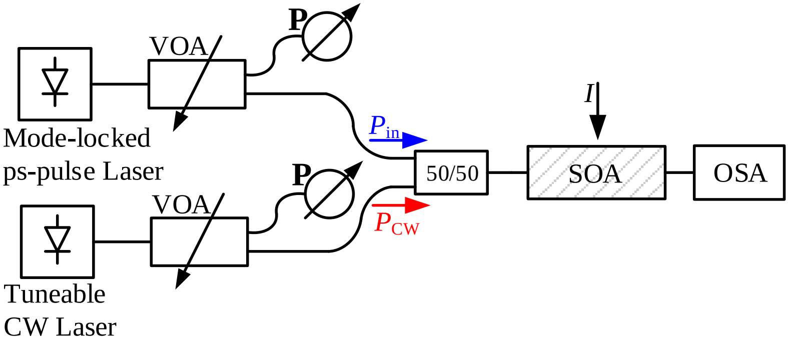

Fig. 4.1 *Experimental setup used for spectral measurements. A pump pulse train from a mode-locked laser is injected together with a CW probe light into an SOA. The output light behind the SOA was measured with an optical spectrum analyzer. The light power was adjusted for probe and pump using variable optical attenuators (VOAs).*

Results will be shown in Section 4.5 and Section 4.6.

4.3 Information retrieval of refractive index dynamics from spectra

4.3.1 Probe light spectrum

For a CW probe light of angular frequency ω_{CW}, instantaneous angular frequency $\omega_{\text{inst}}(t)$, and phase shift $\varphi(t)$ at the SOA output, the slope of the phase modulation can be related to the instantaneous frequency deviation by, see Eq. (3.28)

$$\Delta\omega(t) = \omega_{\text{inst}}(t) - \omega_{\text{CW}} = \frac{\mathrm{d}}{\mathrm{d}t}\varphi(t)\,. \tag{4.1}$$

The sign of $\Delta\omega$ determines an increase or decrease of the phase. A blue-shifted spectral component $(\Delta\omega > 0)$ indicates a decrease of the refractive index $(\Delta n < 0)$ and a red-shifted spectral component $(\Delta\omega < 0)$ an increase $(\Delta n > 0)$.

As mentioned in chapter 3, a measurement of optical spectra does not offer information about the temporal occurrence of the spectral components. The phase dynamics proposed in [25] and [48] is different, leads, however, to similar probe light spectra. In Fig. 4.2 the weak blue spectral band arising from the strong decay of the refractive index can occur either earlier or later as the red component. The missing information can be provided by the output pulse spectrum, Fig. 4.3.

The spectrum of the output pump pulse offers the possibility to find the correct model.

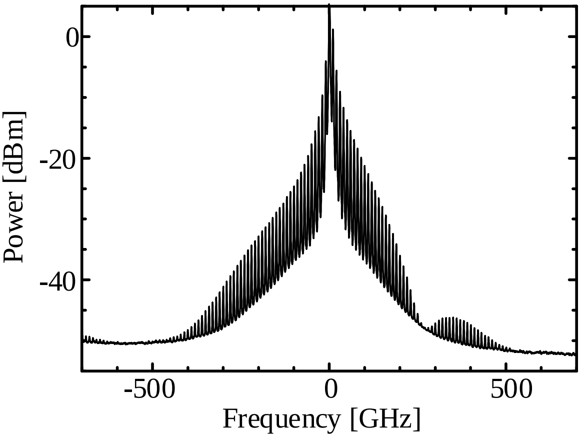

Fig. 4.2 *Probe light spectrum after the SOA, centered at the CW frequency. The pump pulses of* $2.8\,\mathrm{ps}$ *FWHM were emitted at a repetition rate of* $f_{\mathrm{rep}} = 10\,\mathrm{GHz}$*. The pump power was* $P_{\mathrm{in}} = 5\,\mathrm{dBm}$ *at a center wavelength of* $\lambda_0 = 1550\,\mathrm{nm}$*. The CW probe light power was* $P_{\mathrm{CW}} = 2\,\mathrm{dBm}$ *at a wavelength of* $\lambda_{\mathrm{CW}} = 1540\,\mathrm{nm}$*. The SOA was biased at* $I = 400\,\mathrm{mA}$*.*

4.3.2 Pump pulse spectrum after the SOA

The spectrum of the 2.8 ps FWHM pump pulse after propagation through an SOA is shown in Fig. 4.3.

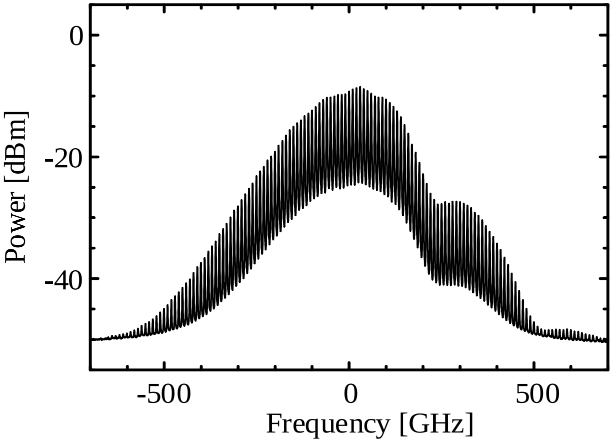

Fig. 4.3 Spectrum of the output pulse centered at the maximum intensity of the input pulses. The pump pulses of $2.8\,\mathrm{ps}$ *FWHM were emitted at a repetition rate of* $f_{\mathrm{rep}} = 10\,\mathrm{GHz}$*. The pump power was* $P_{\mathrm{in}} = 5\,\mathrm{dBm}$ *at a center wavelength of* $\lambda_0 = 1550\,\mathrm{nm}$*. The SOA was biased at* $I = 400\,\mathrm{mA}$*.*

Depending on the power and length of the output pulse, it is differently amplified, broadened (chirped) and distorted. For short pulses of 100 fs [49], 1 ps [50], 2 ps [51] the output spectrum shows additional blue components compared to the input spectrum. For long pulses of 21 ps [52] and 27 ps [50] additional blue and red components appear. Pulses of 55 ps [17] show only an additional red spectral component.

The optical spectra of short pulses capture the refractive index changes in the first span of time of the pulse-SOA interaction, and this time span cannot be longer than the pulse length itself. Since the measured spectra of a 2.8 ps FWHM pump pulse show only blue components, the refractive index dynamics starts with a decay of the refractive index.

The following order of occurrence results for the spectral components:

- weak blue spectral component far away from the CW wavelength,
- strong red component and
- strong blue component close to the CW wavelength.

In the next section we develop an analytical model for the gain and refractive index dynamics of an SOA in a pump-probe experiment and calculate the spectra of the pump and probe light.

4.3.3 Analytical model describing the SOA gain and refractive index dynamics

Optical spectra measured at the SOA output allow to derive the gain and refractive index dynamics of the amplifier operated in the nonlinear regime. The pump spectrum gives information on the self-phase modulation for a time no longer than the pulse duration. The probe light spectrum depicts the cross-gain and cross-phase modulation for the whole time interval of 100 ps between two consecutive pump pulses.

We propose below an analytical model for the gain and refractive index dynamics of an SOA in a pump-probe experiment. The dynamics described in the model impresses a distortion on the shape of an input pump pulse, as also reported in [53]. By comparing measured and calculated spectra for the pump and probe light, it is possible to extract numerical values of the parameters for the various nonlinear processes. This allows to attribute specific spectral components to the respective physical effects.

The following section is taken in part from [54] which covers Sections 2.1 to 4. The text has been altered with respect to variables and figures to match the thesis.

Begin of paper [54], Section 2.1 to Section 4.

Spectral signature of nonlinear effects in semiconductor optical amplifiers

A. Marculescu, S. Ó'Dúill, C. Koos, W. Freude, and J. Leuthold
Opt. Express **25**(24), 29526-29559 (2017)

General description

Before explaining the details of the model, we review the most relevant gain dynamics and gain-saturating processes in SOAs which occur on vastly different time scales [43]. Different α-factors can be attributed to these processes. For simplicity, carrier diffusion along the SOA is neglected.

(i) *Band filling (BF)*. BF relates to the change of the total number of carriers within the energy bands of the SOA. The dynamics comprises carrier depletion (CD) followed by subsequent carrier recovery (CR). The first effect is fast, because stimulated recombination is virtually instantaneous on the timescale of the pulse duration. Carrier depletion increases the refractive index. The recovery, which implies refilling of electron and hole states back to the concentration of the small-signal gain, takes place on a timescale of about $100\,\mathrm{ps}$, which is much longer than the pump pulse duration. The α -factor associated with BF is denoted by α_{BF}. In some publications, the symbol α_{N} is used instead.

(ii) *Spectral hole burning (SHB)*. The pump signal depletes the carriers virtually instantaneously at the pump photon energy so that a "hole" is burned into the gain spectrum. The empty states of the band are refilled through carrier-carrier scattering on a time scale of about 100 fs [22]. The change in gain due to SHB has a symmetric spectral profile around the center frequency of the pump and does not change the refractive index [38]. Assuming the probe frequency is close to the center frequency of the pump, the spectral symmetry applies also to the probe, and we therefore neglect the probe's SHB contribution to the refractive index. Consequently, the associated α_{SHB} factor is assumed to be zero.

(iii) *Carrier heating (CH).* If carrier equilibrium inside a band is destroyed by rapid processes, the instantaneous carrier occupation probability cannot be described anymore with a Fermi function. However, after refilling the unoccupied states left by SHB, the carrier occupation probability follows again a Fermi distribution with an effective "hot" carrier temperature larger than the lattice temperature. The process is named carrier heating. By heating the carrier distribution, the gain decreases [22] and the refractive index increases. Subsequently, the hot carriers cool down (carrier cooling, CC), and the gain relaxes back on a timescale of up to a picosecond (carrier heating relaxation time) [22]. The gain changes lead to refractive index changes, and the associated α -factor is denoted by α_{CH}.

(iv) *Two-photon absorption (TPA) and TPA-induced free carrier absorption (FCA_{TPA})*. Two photons with the same or with different energies can be absorbed simultaneously. This process is rather unlikely, and therefore large powers (large photon numbers) are needed for this effect to be significant. Electrons are lifted virtually instantaneously from the valence band (VB) to the conduction band (CB). The TPA process can occur with simultaneous absorption of two pump photons (degenerate TPA), or with the simultaneous absorption of a pump and of a probe light photon (nondegenerate TPA). For nondegenerate TPA, the polarizations of the optical fields play an important role, such that even for a weak probe light the corresponding TPA absorption coefficient can become twice as large as for degenerate TPA. Although a nondegenerate TPA-process may enhance the absorption coefficient for the probe light, the additional number of photoexcited electrons is too small for a significant change of the refractive index if the probe light is sufficiently weak. The associated increased optical loss with degenerate and nondegenerate TPA and the increased number of carriers lead to an instantaneous decrease of the refractive index [39]. The α -factor associated with the TPA process is thus negative and will be denoted by α_{TPA}. Carriers generated via TPA can become available for free carrier absorption (FCA), we denote this process $\mathrm{FCA}_{\mathrm{TPA}}$, and explain it as follows: For sufficiently strong pulses and semiconductors of suitably small bandgap, two-photon absorption generates an appreciable population of photoexcited electrons in the Γ -valley of the lowest conduction band (CB) [55]. If this Γ -valley is filled or if the sum energy of the two photons is large enough, lower unoccupied states in side-valleys [56], e.g., in the X-valley, can be filled. In this case, however, an additional phonon has to deliver the required difference in crystal momentum. This is also true if electrons in Γ -valley states are to be scattered into the same-energy X-valley states [56, 57]. The transfer of the photoexcited electrons from the Γ -valley to the satellite X-valley needs a finite amount of time τ_0 [57], usually termed intervalley scattering time. Since the bottom of the X-valley lies close [58] to the next higher CB, electrons which reached this side-valley can absorb one more photon (direct absorption) and make a momentum-conserving upwards transition to the next higher conduction band without the assistance of a phonon. This direct,

> TPA-induced free carrier absorption (FCA$_{\mathrm{TPA}}$) has been demonstrated [55] for the binary compounds GaAs and InP. Similar to TPA, TPA-induced FCA increases the optical loss so that the refractive index decreases [59]. However, this refractive index change occurs delayed by the intervalley scattering time τ_0. An instantaneous FCA$_{\mathrm{TPA}}$-effect requires a simultaneous absorption of a photon to conserve both, energy and momentum, and can be neglected [55]. A pictorial explanation of both instantaneous and delayed FCA$_{\mathrm{TPA}}$-processes is given in Appendix A. Intervalley scattering effect may well have other significance for SOAs. In previous work intervalley scattering would explain for the required higher-order correction term applied to the carrier density rate equation in [43] (Eq. (13)), whereby carrier leakage at high carrier energies was necessary to get a good fitting with experiments.

The aforementioned effects can be identified when looking at the evolution of the input pump signal (subscript S) and the input CW probe light (subscript $\times$) inside the SOA. We assume single-mode propagation and represent the waveguide mode by a plane wave with an effective propagation constant $k_0 n_0$ and an effective refractive index n_0. The fields depend on the coordinates z (position) and t (time), and are represented by the square root of the respective powers. Denoting the powers by $P_{\gamma S,\times}(z,t)$ and the phases by $\varphi_{\gamma S,\times}(z,t)$ we write the normalized root-mean-squared (RMS) electric fields as

$$E_{\gamma S,\times}(z,t)=\sqrt{P_{\gamma S,\times}(z,t)}\exp\left[\mathrm{j}\varphi_{\gamma S,\times}(z,t)\right]\exp\left[\mathrm{j}\left(\omega_{S,\times}t-k_0 n_0 z\right)\right], \tag{4.2}$$

where $\omega_0=k_0 c$ stands for the closely neighbored pump signal and probe angular frequencies $\omega_S\approx\omega_\times\approx\omega_0$. In the subsections 4.3.3 and 4.3.4 the index γ is reserved for the functions in the real (non-retarded) time frame. The SOA length is denoted by L. We attach the superscript in (out) to the functions of time at the SOA input (output) at position $z=0$ ($z=L$). Then the input and output normalized RMS fields are given by

$$E_{\gamma S,\times}^{\mathrm{in}}(t)=\sqrt{P_{\gamma S,\times}^{\mathrm{in}}(t)}\exp\left[\mathrm{j}\varphi_{\gamma S,\times}^{\mathrm{in}}(t)\right]\exp\left(\mathrm{j}\omega_{S,\times}t\right) \tag{4.3}$$

and

$$E^{\mathrm{out}}_{\gamma S,\times}(t)=\sqrt{P^{\mathrm{out}}_{\gamma S,\times}(t)}\exp\left[\mathrm{j}\varphi^{\mathrm{out}}_{\gamma S,\times}(t)\right]\exp\left[\mathrm{j}\left(\omega_{S,\times}t-k_0n_0L\right)\right], \tag{4.4}$$

respectively. We further assume that the probe light power is much smaller than the pump light power so that four-wave mixing between pump and probe remains insignificant. In this case coherent interaction is excluded so that the phase relation between pump and probe is unimportant, and the assignments $\varphi^{\mathrm{in}}_{\gamma S,\times}(t)=0$ for both the pump and the probe are justified. Pump wave and probe wave (influenced by the pump) have complex-valued envelopes with a typical width of $2.8\,\mathrm{ps}$,

$$\mathcal{E}_{\gamma S,\times}(z,t)=\sqrt{P_{\gamma S,\times}(z,t)}\exp\left[\mathrm{j}\varphi_{\gamma S,\times}(z,t)\right]. \tag{4.5}$$

When pump and probe propagate simultaneously through the amplifier, the response of the nonlinear medium depends on the powers $P_{\gamma S}(z,t)$ and $P_{\gamma\times}(z,t)$ of both co-propagating fields. This response can be described by a complex refractive index $\underline{n}_{\gamma S,\times}(z,t)$, which is split in a coordinate-independent part n_0, g_0 and a coordinate-dependent contribution $\Delta n_{\gamma S,\times}(z,t)$, $\Delta g_{\gamma S,\times}(z,t)$. Real and imaginary parts define the refractive index $n_{\gamma S,\times}(z,t)$ and the modal gain $g_{\gamma S,\times}(z,t)$, respectively. As $\omega_S\approx\omega_\times\approx\omega_0$ holds, we write

$$\begin{aligned}\Delta\underline{n}_{\gamma S,\times}(z,t)&=\underline{n}_{\gamma S,\times}(z,t)-n_0=\Delta n_{\gamma S,\times}(z,t)+\frac{\mathrm{j}}{2k_0}g_{\gamma S,\times}(z,t),\\ g_{\gamma S,\times}(z,t)&=g_0+\Delta g_{\gamma S,\times}(z,t).\end{aligned} \tag{4.6}$$

While the dominant coordinate-independent part is virtually the same for both signals, the coordinate-dependent contributions $\Delta n_{\gamma S}(z,t)$ and $\Delta n_{\gamma\times}(z,t)$ are in general different because the SOA nonlinearity couples the two optical fields through a nondegenerate TPA process. (Such a coupling cannot occur in the FCA$_{\mathrm{TPA}}$ process because the absorbed photon belongs either to the pump or to the probe light.) We also assume that both signals propagate with the same group velocity v_g, have a negligible group-velocity dispersion [48], and the wavelengths of both pump and probe are close to the wavelength of the SOA gain peak so that SOA gain-dispersion can be ignored, i.e., $\partial g_{\gamma S,\times}/\partial\omega_{S,\times}=0$. For simplicity, throughout this chapter, we neglect the internal loss coefficient α_{int}. In the slowly-varying envelope approximation [17], the complex-valued envelope function $\mathcal{E}_{\gamma S,\times}(z,t)$, Eq. (4.5), is related to the complex refractive index $\underline{n}_{\gamma S,\times}(z,t)$ by the propagation equation

$$\frac{\partial}{\partial z}\mathcal{E}_{\gamma S,\times}(z,t)+\frac{1}{v_g}\frac{\partial}{\partial t}\mathcal{E}_{\gamma S,\times}(z,t)=-\mathrm{j}k_0\Delta\underline{n}_{\gamma S,\times}(z,t)\mathcal{E}_{\gamma S,\times}(z,t). \tag{4.7}$$

It is convenient to formulate the propagation of the light signals in a retarded time frame $\tau=t-z/v_g$ (functions $F_\gamma(z,t)$ transform in retarded functions $F(z,\tau)$),

$$\begin{aligned} P_{S,\times}(z,\tau)&=P_{\gamma S,\times}(z,t), & g_{S,\times}(z,\tau)&=g_{\gamma S,\times}(z,t),\\ \varphi_{S,\times}(z,\tau)&=\varphi_{\gamma S,\times}(z,t), & \Delta n_{S,\times}(z,\tau)&=\Delta n_{\gamma S,\times}(z,t). \end{aligned} \tag{4.8}$$

Since the retarded time τ at the SOA input ($z=0$) coincides with the natural time t, the input pump and CW probe power dependencies as well as the input phase shifts are

$$\begin{aligned} &P_S(0,\tau)=P_{\gamma S}^{\mathrm{in}}(\tau)=P_{\mathrm{in}}(\tau), \qquad P_\times(0,\tau)=P_{\gamma\times}^{\mathrm{in}}(\tau)=P_\times=\mathrm{const},\\ &\varphi_{S,\times}(0,\tau)=\varphi_{\gamma S,\times}^{\mathrm{in}}(\tau)=0. \end{aligned} \tag{4.9}$$

At the SOA output ($z=L$) we have the output pump and CW probe power dependencies as well as the output phase shifts

$$\begin{aligned} P_{S,\times}(L,\tau)&=P_{\gamma S,\times}^{\mathrm{out}}\left(\tau+L/v_g\right)=P_{S,\times}^{\mathrm{out}}(\tau),\\ \varphi_{S,\times}(L,\tau)&=\varphi_{\gamma S,\times}^{\mathrm{out}}\left(\tau+L/v_g\right)=\varphi_{S,\times}^{\mathrm{out}}(\tau). \end{aligned} \tag{4.10}$$

We now perform the coordinate transformations (z,t) to (z,τ) in Eq. (4.7), separate modulus and argument of $\mathcal{E}_{S,\times}$, observe $P_{S,\times}=\mathcal{E}_{S,\times}\mathcal{E}_{S,\times}^*$, and obtain the propagation equations for the powers and the phase shifts,

$$\frac{\partial}{\partial z}P_{S,\times}(z,\tau)=g_{S,\times}(z,\tau)P_{S,\times}(z,\tau) \tag{4.11}$$

and

$$\frac{\partial}{\partial z}\varphi_{S,\times}(z,\tau)=-k_0\Delta n_{S,\times}(z,\tau), \tag{4.12}$$

respectively. Integrating Eq. (4.11) over the SOA length leads to

$$P_{S,\times}(L,\tau)=P_{S,\times}(0,\tau)\exp\left[h_{S,\times}(\tau)\right], \qquad h_{S,\times}(\tau)=\int_0^L g_{S,\times}(z,\tau)\,\mathrm{d}z\,. \tag{4.13}$$

The power gain coefficient $g_{S,\times}(z,\tau)$ in Eq. (4.11) is positive and takes care of the fact that the signal power is distributed over a cross-section so that the total power is larger by the field concentration factor [60]. The highest value g_0 represents the unsaturated small-signal gain, see Eq. (4.6). The dimensionless integrated gain coefficient $h_{S,\times}(\tau)$ (logarithmic power gain) is also positive and determines the amplification of the respective optical signal

$$\frac{P_{S,\times}(L,\tau)}{P_{S,\times}(0,\tau)}=\exp\left[h_{S,\times}(\tau)\right]. \tag{4.14}$$

The integrated unsaturated gain coefficient $h_0=g_0L$ corresponds to the largest amplification. It is convenient to subtract h_0 from $h_{S,\times}(\tau)$ and introduce the integrated gain decrease

$$\Delta h_{S,\times}(\tau)=h_{S,\times}(\tau)-h_0=\int_0^L\left[g_{S,\times}(z,\tau)-g_0\right]\mathrm{d}z\,. \tag{4.15}$$

From Eq. (4.12) we find the solution $\Delta\varphi_{S,\times}(\tau)$ for the spatially integrated phase change of the output light with respect to the input light,

$$\begin{aligned}\Delta\varphi_{S,\times}(\tau)&=\varphi_{S,\times}(L,\tau)-\varphi_{S,\times}(0,\tau)=-k_0L\Delta n_{S,\times}(\tau),\\ \Delta n_{S,\times}(\tau)&=\frac{1}{L}\int_0^L\Delta n_{S,\times}(z,\tau)\,\mathrm{d}z.\end{aligned} \tag{4.16}$$

The nonlinear output phase shift follows from Eqs. (4.9) and (4.16),

$$\varphi_{S,\times}^{\mathrm{out}}(\tau)=-k_0\int_0^L\Delta n_{S,\times}(z,\tau)\,\mathrm{d}z\,. \tag{4.17}$$

In Fig. 4.4 we display a schematic of the dependencies listed in Eqs. (4.9), (4.10) and (4.16). The pump pulse $P_S^{\mathrm{in}}(\tau)$ at the input has a symmetric shape (shown in red in Fig. 4.4 (a)). While propagating through the SOA, the leading edge of the pump pulse experiences a larger gain than the trailing edge, due to gain saturation. The pump pulse emerging at the SOA output (shown in blue in Fig. 4.4(a)) has therefore an asymmetric shape with its peak power shifted to smaller τ, this has been documented in [17].

The gain dynamics which results from the previously mentioned effects is probed with a weak CW input light having constant power $P_\times$, which becomes modulated by the instantaneous gain. Fig. 4.4(b) shows the power dependency of the modulated probe light $P_\times(L,\tau)=P_\times^{\text{out}}(\tau)$. The gain decreases as induced by the pump pulse causes the falling slope of $P_\times^{\text{out}}(\tau)$. While CD occurs over the whole pump pulse duration, only the processes dominant in each temporal segment are explicitly marked. The probe power minimum is reached *after* the (input) pump pulse maximum at $\tau=0$, because CD, TPA and SHB are still in effect. Eventually, the SOA gain recovers, and subsequently the probe power increases towards its initial value.

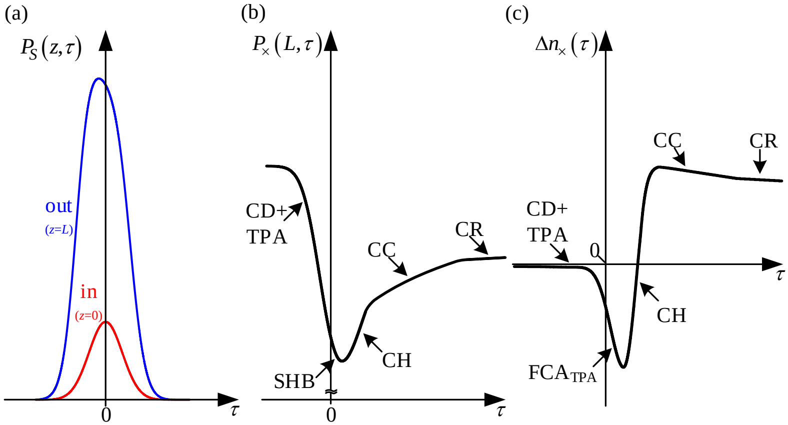

Fig. 4.4 *Schematic input and output pump power, probe output power, and refractive index change as a function of retarded time* $\tau=t-z/v_g$ *(t: real time, z: propagation coordinate,* v_g *: group velocity). The dominant process for each time segment is marked. (a) Input pump pulse power (red line,* $z=0$ *) and output pump pulse power (blue line,* $z=L$ *). (b) Probe output light power at* $z=L$ *. (c) Refractive index change* $\Delta n_\times(\tau)$ *according to Eq. (4.16), averaged over the SOA length. (CD: Carrier depletion; CH: Carrier heating; TPA: Two-photon absorption; SHB: Spectral hole burning;* FCA_{TPA}*: Free carrier absorption induced by TPA; CC: Carrier cooling; CR: Carrier recovery).*

The time dependency of the change in the refractive index $\Delta n_\times(\tau)$ is shown in Fig. 4.4(c). The combined effects of CD (Section (i)) and TPA (Section (iv)) reduce the gain. However, the corresponding positive (CD) and negative changes (TPA) in the refractive index tend to balance, resulting in a time-independent region (CD+TPA) in Fig. 4.4(c). The onset of SHB in Fig. 4.4(b) reduces the gain further, but has no effect on the refractive index change, Fig. 4.4(c) (Section (ii)). While all nonlinear effects in Fig. 4.4 (b) are of first order and FCA can be neglected, the index change in Fig. 4.4(c) due to $\mathrm{FCA_{TPA}}$ decreases quadratically with the pump pulse power, so that TPA-induced free carrier absorption ($\mathrm{FCA_{TPA}}$) is responsible (Section (iv)) for the pronounced dip in the refractive index curve. During the ultrafast gain recovery (CH) the refilling of the spectral hole counteracts CD and increases the gain. Consequently, the SOA refractive index increases (Section (iii)). Once the pump signal leaves the SOA, the carrier distributions start resuming their intraband equilibrium states (CC). Finally, CR through the injection current begins and re-establishes the original carrier concentration.

Description of the analytical model

We now describe the gain and phase evolution by an analytical model in which the probe power can be considered negligible. The pump power $P_S\left(z,\tau\right)$ influences the amplification and phase shift for both pump and probe light. According to the discussion of Section (iv), a weak probe light plays an important role only for TPA processes.

As a consequence, we will treat the other processes (BF, SHB and CH) as if they occur in the absence of the probe, and therefore omit the subscript S for all dynamical quantities except $P_S\left(z,\tau\right)$.

The local modal gain coefficient $g\left(z,\tau\right)$ comprises the small-signal gain coefficient g_0 and the coefficients of the gain changes $\Delta g_{\mathrm{x}}\left(z,\tau\right)$ from the contributions of the processes labelled by “x”, i.e., $\mathrm{x}=\left\{\mathrm{BF,SHB,CH,TPA}\right\}$. We neglect the internal loss coefficient because we were not able to include it in an analytical model. By integrating the gain coefficients over the SOA length and summing up over all processes, we obtain the logarithmic power gain, see Eqs. (4.13) and (4.15). We therefore write

$$
\begin{aligned}
g(z,\tau) &= g_0 + \sum_{\mathrm{x}} \Delta g_{\mathrm{x}}(z,\tau), \quad h(\tau) = h_0 + \Delta h(\tau), \\
\Delta h(\tau) &= \sum_{\mathrm{x}} \Delta h_{\mathrm{x}}(\tau), \quad \Delta h_{\mathrm{x}}(\tau) = \int_0^L \Delta g_{\mathrm{x}}(z,\tau)\,\mathrm{d}z.
\end{aligned}
\tag{4.18}
$$

The α_{x}-factors associated with the above processes are denoted by

$$
\alpha_{\mathrm{x}} = -2k_0 \frac{\Delta n_{\mathrm{x}}(z,\tau)}{\Delta g_{\mathrm{x}}(z,\tau)}, \qquad \mathrm{x}=\{\mathrm{BF,\ SHB,\ CH,\ TPA}\}\,. \tag{4.19}
$$

The α_{x}-factors do not depend on time or space, because the functional dependencies of $\Delta n_{\mathrm{x}}(z,\tau)$ and $\Delta g_{\mathrm{x}}(z,\tau)$ are assumed to be the same. For simplicity, we neglect the coefficient Δg_{FCA} associated with the two-photon induced free carrier absorption in our analysis and the corresponding local change $\Delta n_{\mathrm{FCA}}(z,\tau)$ of the refractive index is derived by applying the Drude model, see Eq. (4.51). The total change in the refractive index $\Delta n(z,\tau)$ is given by

$$
\begin{aligned}
\Delta n(z,\tau) &= \sum_{\mathrm{x}} \Delta n_{\mathrm{x}}(z,\tau) + \Delta n_{\mathrm{FCA}}(z,\tau), \\
\Delta n_{\mathrm{x}}(z,\tau) &= -\frac{\alpha_{\mathrm{x}}}{2k_0} \Delta g_{\mathrm{x}}(z,\tau).
\end{aligned}
\tag{4.20}
$$

We substitute Eq. (4.20) in the right-hand side of Eq. (4.17) in order to determine the output phase shift of the pump field. We denote the contribution of the various processes by

$$
\begin{aligned}
\Delta\varphi_{\mathrm{x}}(\tau) &= -k_0 \int_0^L \Delta n_{\mathrm{x}}(z,\tau)\,\mathrm{d}z = \frac{1}{2}\alpha_{\mathrm{x}} \int_0^L \Delta g_{\mathrm{x}}(z,\tau)\,\mathrm{d}z, \\
\Delta\varphi_{\mathrm{FCA}}(\tau) &= -k_0 \int_0^L \Delta n_{\mathrm{FCA}}(z,\tau)\,\mathrm{d}z.
\end{aligned}
\tag{4.21}
$$

Further, taking into account that $\Delta\varphi_{\mathrm{x}}(\tau) = 1/2\,\alpha_{\mathrm{x}}\Delta h_{\mathrm{x}}(\tau)$ holds, we eventually obtain

$$
\varphi^{\mathrm{out}}(\tau) = \frac{1}{2}\sum_{\mathrm{x}} \alpha_{\mathrm{x}} \Delta h_{\mathrm{x}}(\tau) + \Delta\varphi_{\mathrm{FCA}}(\tau)\,. \tag{4.22}
$$

We now start with the analytical description for band filling as developed by Agrawal and Olsson [17], and we then include the ultrafast gain saturation as well as the TPA effect in a phenomenological fashion [48, 61]. In the following, we calculate the individual gain changes $\Delta g_{\mathrm{x}}(z,\tau)$ and the integrated coefficients $\Delta h_{\mathrm{x}}(\tau)$ of Eq. (4.18) as well as the quantities $\Delta n_{\mathrm{FCA}}(z,\tau)$ and $\Delta\varphi_{\mathrm{FCA}}(\tau)$ related by Eq. (4.21).

Spatial integration techniques to account for nonlinear effects were previously described in [62] for gain recovery in SOAs, and in [63] for analyzing active and passive silicon waveguides. Such techniques are very different from the traditional discretization approach used in the context of distributed feedback semiconductor lasers [64].

Logarithmic gain

The description of the carrier dynamics in the active medium is based on rate equations [65, 66].

Band filling

We assume a linear dependence of the band filling gain coefficient $g_0+\Delta g_{\mathrm{BF}}(z,\tau)$ on the carrier concentration $N(z,\tau)$ and write

$$\Delta g_{\mathrm{BF}}(z,\tau)=\Gamma a_0\left[N(z,\tau)-N_{\mathrm{st}}\right], \tag{4.23}$$

where Γ denotes the field confinement factor, a_0 is the differential gain and N_{st} represents the unsaturated value of the carrier density [61]. Here we include Γ, a_0 and N_{st} in the unsaturated (small-signal) gain $g_0=\Gamma\overline{g}_0$, the saturation power [61] P_{sat}, and in the spontaneous carrier lifetime τ_s, see Eq. (2.23). We now put down a differential equation that describes the temporal evolution of band filling during a pump-probe experiment with a negligible probe light power. From the differential equation for the charge carrier concentration we find the differential equation [65] for Δg_{BF} as

$$\frac{\partial}{\partial\tau}\Delta g_{\mathrm{BF}}(z,\tau)=\underbrace{-\left[g(z,\tau)-\frac{1}{2}\Delta g_{\mathrm{TPA}}(z,\tau)\right]\frac{P_S(z,\tau)}{P_{\mathrm{sat}}\tau_s}}_{\mathrm{CD}}\underbrace{-\frac{\Delta g_{\mathrm{BF}}(z,\tau)}{\tau_s}}_{\mathrm{CR}}. \tag{4.24}$$

Band filling effects comprise carrier depletion (CD) and carrier recovery (CR). As the unsaturated gain coefficient is always larger than the band filling gain coefficient, $\Delta g_{\mathrm{BF}}(z,\tau)<0$. The first term on the right-hand side of Eq. (4.24) is negative and therefore stands for the power gain decrease which is due to induced carrier depletion. The first term also includes TPA gain. According to [65] the TPA contribution to the carrier density increase has a weight factor $1/2$, therefore we have to subtract $1/2\,\Delta g_{\mathrm{TPA}}(z,\tau)$ from the total gain $g(z,\tau)$ in Eq. (4.18). The second term is responsible for an increase of the gain and therefore for carrier recovery on a timescale of τ_s. For picosecond pulses, CD and CR operate on two vastly different timescales (see Section (i)) and both effects can be treated separately. Over the duration of the pump pulse, CD is instantaneous and dominates over a timescale much shorter than τ_s, therefore CR is negligible allowing for the CR term in Eq. (4.24) to be set to zero. After the pump pulse has vanished, there is no more carrier depletion and now CR dominates, the first term in Eq. (4.24) can be neglected. We now solve Eq. (4.24) analytically for both cases separately. When CD dominates we use the notation $\Delta g_{\mathrm{BF}}=\Delta g_{\mathrm{CD}}$, and we use the notation $\Delta g_{\mathrm{BF}}=\Delta g_{\mathrm{CR}}$ when CR dominates. The integrated gain coefficient, $\Delta h_{\mathrm{BF}}(\tau)$, will be accordingly denoted by $\Delta h_{\mathrm{BF}}=\Delta h_{\mathrm{CD}}$ and $\Delta h_{\mathrm{BF}}=\Delta h_{\mathrm{CR}}$.

Carrier depletion

For the case of weak to moderate pump energies, i.e., when the effects of CH, SHB and TPA on pump-induced changes in carrier density are neglected and the conditions $\left|\Delta g_{\mathrm{x}\neq\mathrm{CD}}(z,\tau)\right| \ll g_0+\Delta g_{\mathrm{CD}}(z,\tau)$ hold, the local gain coefficient $g(z,\tau)$ describes only the CD contribution $g_0+\Delta g_{\mathrm{CD}}(z,\tau)$ of the BF effect,

$$g(z,\tau)\approx g_0+\Delta g_{\mathrm{CD}}(z,\tau). \tag{4.25}$$

As a consequence, in determining $\Delta g_{\mathrm{CD}}(z,\tau)$ we can approximate $P_{\mathrm{S}}(z,\tau)$ by the solution $P_{\mathrm{CD}}(z,\tau)$ of the propagation equation

$$\frac{\partial}{\partial z}P_{\mathrm{CD}}(z,\tau)=\left[g_0+\Delta g_{\mathrm{CD}}(z,\tau)\right]P_{\mathrm{CD}}(z,\tau). \tag{4.26}$$

Writing $P_{\mathrm{S}}(z,\tau)\approx P_{\mathrm{CD}}(z,\tau)$ the first term of the right-hand side of Eq. (4.24) simplifies to

$$\frac{\partial}{\partial \tau}\Delta g_{\mathrm{CD}}(z,\tau)=-\left[g_0+\Delta g_{\mathrm{CD}}(z,\tau)\right]\frac{P_{\mathrm{CD}}(z,\tau)}{P_{\mathrm{sat}}\tau_s}. \tag{4.27}$$

We integrate both sides of Eq. (4.27) over the whole SOA length, substitute $\left[g_0+\Delta g_{\mathrm{CD}}(z,\tau)\right]P_{\mathrm{CD}}(z,\tau)$ from Eq. (4.26), employ Eq. (4.13) with $P_{\mathrm{CD}}(0,\tau)=P_{\mathrm{in}}(\tau)$, and find a differential equation for the integrated BF gain coefficient Δh_{CD},

$$\frac{\mathrm{d}}{\mathrm{d}\tau}\Delta h_{\mathrm{CD}}(\tau)=-\frac{\exp\left[h_0+\Delta h_{\mathrm{CD}}(\tau)\right]-1}{P_{\mathrm{sat}}\tau_s}P_{\mathrm{in}}(\tau)\,. \tag{4.28}$$

With the integrated unsaturated small-signal gain as an initial condition, $\Delta h_{\mathrm{CD}}(-\infty)=0$, Eq. (4.28) can be integrated (see Appendix B) resulting in

$$\Delta h_{\mathrm{CD}}(\tau)=-\ln\left\{\exp(h_0)-\left[\exp(h_0)-1\right]\exp\left[-\int_{-\infty}^{\tau}P_{\mathrm{in}}(\tau')\,\mathrm{d}\tau'\Big/\left(P_{\mathrm{sat}}\tau_s\right)\right]\right\}. \tag{4.29}$$

For the case of Gaussian input pulses, the integral in Eq. (4.29) has a closed-form expression in terms of the error function [17].

After $h_0+\Delta h_{\mathrm{BF}}(\tau)$ has attained its minimum, it recovers back to the unsaturated value h_0. As the model is based on a sharp separation of CD and CR, the temporal threshold $\tau=\tau_{\mathrm{R}}$ needs to be introduced. A suitable time $-\tau_{\mathrm{R}}$ can be identified as the moment when the gain saturation begins. The gain reduction (in dB) up to this moment can be written as $10\log_{10}\left\{\exp\left[\left|\Delta h_{\mathrm{CD}}(-\tau_{\mathrm{R}})\right|\right]\right\}=q$. Eq. (4.29) allows for the determination of the time $\tau=-\tau_{\mathrm{R}}$ when the gain amplification starts modifying

$$\int_{-\infty}^{-\tau_{\mathrm{R}}}P_{\mathrm{in}}(\tau)\,\mathrm{d}\tau=P_{\mathrm{sat}}\tau_{\mathrm{s}}\ln\left[\frac{\exp(h_0)-1}{\exp(h_0)-10^{q/10}}\right]. \tag{4.30}$$

The energy content of the part up to $-\tau_{\mathrm{R}}$ in the leading edge represents thus the largest energy for which the saturation can be neglected in the CD process. We can assume that the amplification ceases when the energy content of the final part in the trailing edge attains the amount considered negligible. For symmetric pulses, i.e., for $P_{\mathrm{in}}(-\tau)=P_{\mathrm{in}}(\tau)$, this happens at $\tau=+\tau_{\mathrm{R}}$, due to the obvious identity $\int_{\tau_{\mathrm{R}}}^{\infty}P_{\mathrm{in}}(\tau)\,\mathrm{d}\tau=\int_{-\infty}^{-\tau_{\mathrm{R}}}P_{\mathrm{in}}(\tau)\,\mathrm{d}\tau$. Given a certain gain reduction q at the beginning of the saturation (at time $\tau=-\tau_{\mathrm{R}}$), one can solve the resulting Eq. (4.30) for τ_{R}. This procedure is particularly useful for a Gaussian power pulse of width τ_{p}, where the ratio $\tau_{\mathrm{R}}/\tau_{\mathrm{p}}$ can be expressed in closed-form through the complementary error-function involving q (and other independent parameters). A practicable criterion for determining τ_R will be presented later.

Carrier recovery

The differential equation for the gain recovery coefficient $\Delta g_\mathrm{CR}\left(z,\tau\right)$ is found by setting the first term on the right-hand side of Eq. (4.24) to zero,

$$\frac{\partial}{\partial\tau}\Delta g_\mathrm{CR}\left(z,\tau\right)=-\frac{\Delta g_\mathrm{CR}\left(z,\tau\right)}{\tau_s}\,. \tag{4.31}$$

The CR gain dynamics for $\Delta h_\mathrm{BF}\left(\tau\right)$ is obtained by integrating both sides of Eq. (4.31) over the SOA length and by solving the resulting differential equation for $\Delta h_\mathrm{CR}\left(\tau\right)$ with the initial condition

$$\Delta h_\mathrm{CR}\left(\tau_\mathrm{R}\right)=\Delta h_\mathrm{CD}\left(\tau_\mathrm{R}\right). \tag{4.32}$$

The value of $\Delta h_\mathrm{CD}\left(\tau_\mathrm{R}\right)$ on the right-hand side has to be found from Eq. (4.29).

Overall band filling

The complete gain contribution to BF is then given by

$$\Delta h_\mathrm{BF}\left(\tau\right)=\begin{cases}\Delta h_\mathrm{CD}\left(\tau\right) & \tau\le\tau_\mathrm{R}\\ \Delta h_\mathrm{CD}\left(\tau_\mathrm{R}\right)\exp\left(-\dfrac{\tau-\tau_\mathrm{R}}{\tau_s}\right) & \tau>\tau_\mathrm{R}\,.\end{cases} \tag{4.33}$$

Our approximations lead to an analytical result, however, the time derivative of $\Delta h_\mathrm{BF}\left(\tau\right)$ is no more continuous at $\tau=\tau_\mathrm{R}$.

Spectral hole burning and carrier heating

The equations describing the intraband dynamics are stated in [66]. If intraband relaxation times are much smaller than the pulse width, the time derivative in these equations can be adiabatically eliminated, i.e., set to zero, and the local gain changes $\Delta g_\mathrm{SHB,CH}\left(z,\tau\right)$ can be immediately written as [61]

$$\Delta g_\mathrm{SHB,CH}\left(z,\tau\right)=-\varepsilon_\mathrm{SHB,CH}\left[g\left(z,\tau\right)-\Delta g_\mathrm{TPA}\left(z,\tau\right)\right]P_S\left(z,\tau\right), \tag{4.34}$$

with $\varepsilon_{\mathrm{SHB.CH}}^{-1}$ being the saturation power for the respective process. Accordingly, it is the ratio of ultrafast gain compression $\Delta g_{\mathrm{SHB,CH}}$ to the local material gain, $g-\Delta g_{\mathrm{TPA}}$, that is proportional to the pulse power inside the SOA. The material gain itself comprises $g_0+\Delta g_{\mathrm{BF}}$ and the local ultrafast gain contribution $\Delta g_{\mathrm{SHB}}+\Delta g_{\mathrm{CH}}$ which can be calculated from Eq. (4.34). Denoting the total ultrafast compression coefficient by $\varepsilon=\varepsilon_{\mathrm{SHB}}+\varepsilon_{\mathrm{CH}}$, one can relate $g-\Delta g_{\mathrm{TPA}}$ to $g_0+\Delta g_{\mathrm{BF}}$, see the first Eq. (4.18). By making use of this relation in Eq. (4.34), one obtains

$$\Delta g_{\mathrm{SHB,CH}}(z,\tau)=-\varepsilon_{\mathrm{SHB,CH}}\frac{\left[g_0+\Delta g_{\mathrm{BF}}(z,\tau)\right]P_S(z,\tau)}{1+\varepsilon P_S(z,\tau)}\,. \tag{4.35}$$

Eq. (4.35) describes the ultrafast gain reduction due only to the stimulated emission that removes the “cool” carriers from the distribution. We do not consider here the carrier heating via TPA and FCA. The ultrafast processes occur simultaneously with CD, however we calculate their contributions by only considering CD, see Eq. (4.25). For strong pulses the amount of CD would also be affected by the strength of the ultrafast gain compression, but for moderate levels of gain compression it is sufficient to replace in Eq. (4.35) Δg_{BF} by Δg_{CD} and $P_S(z,\tau)$ by $P_{\mathrm{CD}}(z,\tau)$ as defined in Eq. (4.26). As a consequence, $\Delta g_{\mathrm{SHB,CH}}(z,\tau)$ can be written as

$$\Delta g_{\mathrm{SHB,CH}}(z,\tau)=-\frac{\varepsilon_{\mathrm{SHB,CH}}}{\varepsilon}\frac{\partial}{\partial z}\left\{\ln\left[1+\varepsilon P_{\mathrm{CD}}(z,\tau)\right]\right\}\,. \tag{4.36}$$

The ultrafast compressions are obtained by integrating both sides of Eq. (4.36) over z from $z=0$ to $z=L$, and by taking into account the boundary conditions

$$P_{\mathrm{CD}}(0,\tau)=P_{\mathrm{in}}(\tau) \text{ and } P_{\mathrm{CD}}(L,\tau)=P_{\mathrm{in}}(\tau)\exp\left[h_0+\Delta h_{\mathrm{CD}}(\tau)\right] \tag{4.37}$$

with the result

$$\Delta h_{\mathrm{SHB,CH}}(\tau)=-\frac{\varepsilon_{\mathrm{SHB,CH}}}{\varepsilon}\ln\left\{\frac{1+\varepsilon P_{\mathrm{in}}(\tau)\exp\left[h_0+\Delta h_{\mathrm{CD}}(\tau)\right]}{1+\varepsilon P_{\mathrm{in}}(\tau)}\right\}. \tag{4.38}$$

The above results remain valid in the presence of a weak probe light. In contrast, as will be shown below, the probe light can sensibly influence the TPA-process, even when its power $P_\times$ is small.

Two-photon absorption

We describe the local gain reduction due to a degenerate TPA-process (simultaneous absorption of two identical photons) by an absorption coefficient $\Delta g_{\mathrm{TPA}}(z,\tau)$ which is proportional to the power of the propagating light P_S and to the inverse of an effective TPA cross-section A_{TPA} [60, 65], with a proportionality factor $\beta_2(\omega_S)$ called the TPA coefficient at the pump frequency ω_S ,

$$\Delta g_{\mathrm{TPA}}(z,\tau) = -\frac{\beta_2(\omega_S)}{A_{\mathrm{TPA}}} P_S(z,\tau) \qquad \text{(degenerate case)}. \tag{4.39}$$

The area A_{TPA} is larger than the cross-section A of the active region [60], because it always includes some adjacent layers within the cladding region.

In a nondegenerate TPA-process a VB electron can reach the CB by absorbing one photon from the pump and another photon from the probe. The pump having power P_S and angular frequency ω_S is assumed to be dominantly linear polarized in the direction of the unit vector $\vec{e}_S$, which lies in the cross-section area of the SOA waveguide. The probe light with power $P_\times$ and angular frequency $\omega_\times$ is assumed to be linearly polarized in the same plane, but along a different direction $\vec{e}_\times$, and its contribution has to be weighted by a factor $\beta_S(\omega_S,\vec{e}_S,\omega_\times,\vec{e}_\times)/\beta_2(\omega_S)$ [67, 68]. The local TPA absorption coefficient $\Delta g_{\mathrm{TPA},S}(z,\tau)$ experienced by the pump in the presence of the probe light is

$$\Delta g_{\mathrm{TPA},S}(z,\tau) = -\frac{\beta_2(\omega_S)}{A_{\mathrm{TPA}}}\left[P_S(z,\tau) + \frac{\beta_S(\omega_S,\vec{e}_S,\omega_\times,\vec{e}_\times)}{\beta_2(\omega_S)} P_\times(z,\tau)\right]. \tag{4.40}$$

In analogy, we define the local TPA absorption coefficient $\Delta g_{\mathrm{TPA},\times}(z,\tau)$ experienced by the probe light in the presence of the pump light as

$$\Delta g_{\mathrm{TPA},\times}(z,\tau) = -\frac{\beta_2(\omega_\times)}{A_{\mathrm{TPA}}}\left[\frac{\beta_\times(\omega_S,\vec{e}_S,\omega_\times,\vec{e}_\times)}{\beta_2(\omega_\times)} P_S(z,\tau) + P_\times(z,\tau)\right]. \tag{4.41}$$

The functions $\beta_{S,\times}\left(\omega_S,\vec{e}_S,\omega_\times,\vec{e}_\times\right)$ depend on the relative polarization angle, $\cos^{-1}\left(\vec{e}_S\cdot\vec{e}_\times\right)$, are related to each other, and become equal for $\omega_S=\omega_\times$ [68], see Appendix C. In general, a TPA in pump-probe experiments consists of three kinds of absorption processes occurring at the same time: absorption processes of identical photon pairs from the pump and probe light, and of different photon pairs from the pump-probe coupling. For neighboring angular frequencies $\omega_S\approx\omega_\times\approx\omega_0$ we introduce a new parameter r_{TPA} by the ratio

$$r_{\mathrm{TPA}}=\frac{\beta_{S,\times}\left(\omega_0,\vec{e}_S,\omega_0,\vec{e}_\times\right)}{\beta_2\left(\omega_0\right)}, \tag{4.42}$$

write β_2 for $\beta_2\left(\omega_0\right)$ and simplify Eqs. (4.40) and (4.41) to

$$\Delta g_{\mathrm{TPA},S}\left(z,\tau\right)=-\frac{\beta_2}{A_{\mathrm{TPA}}}\left[P_S\left(z,\tau\right)+r_{\mathrm{TPA}}P_\times\left(z,\tau\right)\right] \tag{4.43}$$

and

$$\Delta g_{\mathrm{TPA},\times}\left(z,\tau\right)=-\frac{\beta_2}{A_{\mathrm{TPA}}}\left[r_{\mathrm{TPA}}P_S\left(z,\tau\right)+P_\times\left(z,\tau\right)\right]. \tag{4.44}$$

The ratio r_{TPA}, hereafter called the TPA non-degeneracy factor, is positive and depends on the relative polarization angle. For semiconductors with zinc blende crystal structure $r_{\mathrm{TPA}}=2$ for parallel polarizations and takes on a value 2-3 times smaller for orthogonal polarizations, depending on the probe frequency [68, 69], see Appendix C. Moreover, for a weak probe light only the first term on the right-hand side of Eqs. (4.43) and (4.44) contributes, and we are left with

$$\Delta g_{\mathrm{TPA},S}\left(z,\tau\right)=\Delta g_{\mathrm{TPA}}\left(z,\tau\right),\quad \Delta g_{\mathrm{TPA},\times}\left(z,\tau\right)=r_{\mathrm{TPA}}\Delta g_{\mathrm{TPA}}\left(z,\tau\right). \tag{4.45}$$

Under the assumptions stated above, the local absorption coefficient from the pump in the presence of the (weak) probe light coincides with the degenerate case, Eq. (4.39), while the local absorption coefficient from the (weak) probe light differs from the latter by the TPA non-degeneracy factor r_{TPA} due to the pump-probe coupling. Proceeding in analogy to the fourth formula in Eq. (4.18) and substituting the subscript x by TPA,S and $\mathrm{TPA},\times$, the integrated absorption coefficients $\Delta h_{\mathrm{TPA},S}$ for the degenerate case and $\Delta h_{\mathrm{TPA},\times}$ for the nondegenerate case can be written with the help of Eq. (4.45) as

$$\Delta h_{\mathrm{TPA},S}\left(\tau\right)=\Delta h_{\mathrm{TPA}}\left(\tau\right),\ \Delta h_{\mathrm{TPA},\times}\left(\tau\right)=r_{\mathrm{TPA}}\Delta h_{\mathrm{TPA}}\left(\tau\right). \tag{4.46}$$

Similarly, proceeding in analogy to Eq. (4.21), we find the TPA-induced phase change contributions $\Delta\varphi_{\mathrm{TPA},S}$ for the degenerate case and $\Delta\varphi_{\mathrm{TPA},\times}$ for the nondegenerate case

$$\Delta\varphi_{\mathrm{TPA},S}\left(\tau\right)=\frac{1}{2}\alpha_{\mathrm{TPA}}\Delta h_{\mathrm{TPA}}\left(\tau\right),\quad \Delta\varphi_{\mathrm{TPA},\times}\left(\tau\right)=\frac{1}{2}\alpha_{\mathrm{TPA}}r_{\mathrm{TPA}}\Delta h_{\mathrm{TPA}}\left(\tau\right). \tag{4.47}$$

The dynamical quantities in Eqs. (4.46) and (4.47), associated to the TPA-process are all expressed in terms of the contribution $\Delta h_{\mathrm{TPA}}\left(\tau\right)$. For the calculation of this contribution according to Eqs. (4.18) and (4.39), it is necessary to integrate $P_S\left(z,\tau\right)$ over the SOA length. Since in Eq. (4.25) we assumed that ultrafast processes including TPA are negligible in comparison with CD, we replaced $P_S\left(z,\tau\right)$ by the solution $P_{\mathrm{CD}}\left(z,\tau\right)$ of Eq. (4.26). The integration of arbitrary positive powers of $P_{\mathrm{CD}}\left(z,\tau\right)$ is carried out in Appendix B, yielding the coefficients $C_n\left(\tau\right)$, see Eq. (B.15). An explicit form of $P_{\mathrm{CD}}\left(z,\tau\right)$ is shown in Eqs. (B.11) and (B.13). By introducing the compression coefficient

$$\varepsilon_{\mathrm{TPA}}=\frac{\beta_2 L}{A_{\mathrm{TPA}}h_0}, \tag{4.48}$$

and by using the result, see Eq. (B.22),

$$C_1\left(\tau\right)=\frac{\left|\Delta h_{\mathrm{CD}}\left(\tau\right)\right|}{\exp\left[\left|\Delta h_{\mathrm{CD}}\left(\tau\right)\right|\right]-1}, \tag{4.49}$$

one finds the following TPA contribution $\Delta h_{\mathrm{TPA}}\left(\tau\right)$:

$$\Delta h_{\mathrm{TPA}}\left(\tau\right)=-\varepsilon_{\mathrm{TPA}}\left[\exp\left(h_0\right)-1\right]C_1\left(\tau\right)P_{\mathrm{in}}\left(\tau\right). \tag{4.50}$$

We prove in Appendix B that all coefficients $C_n\left(\tau\right),\ n=1,2,\ldots$ are positive and decrease with time.

FCA$_{TPA}$ induced refractive index

In order to include the FCA$_{\text{TPA}}$ process as described in [55], we assume that many of the photoexcited electrons reach the X-valley of the lowest CB by absorbing optical phonons of suitable wave vectors. Owing to the low amount of energy carried by the phonon [56], the energy of the electron remains nearly constant, while its momentum increases accordingly. Also, the transit time to the X-valley expressed by the intervalley scattering time τ_0 is of order of the electron-phonon scattering time. Once arrived in the new X-valley state, the electrons can be further excited into the next higher CB by absorption of a photon. The contribution of this free carrier absorption to the index change can be estimated based on the classical oscillator model of Drude and Lorentz. By assuming the electrons moving freely in the optical field according to Newton's second law, one finds the decrease of the refractive index as given by the Drude formula [37]

$$\Delta n_{\text{FCA}}\left(z,\tau\right) = -\frac{e^2}{2\varepsilon_0 n_0 \omega_0^2 m_{\text{FCA}}} N_{\text{FCA}}\left(z,\tau\right), \qquad (4.51)$$

where N_{FCA} denotes the intraband density of FCA-excited electrons with effective mass m_{FCA} and the field-independent refractive index n_0. Since in general $N_{\text{FCA}}\left(z,\tau\right)$ represents only a fraction K of the density $N_{\text{ex}}\left(z,\tau\right)$ of photoexcited electrons, one can write

$$N_{\text{FCA}}\left(z,\tau\right) = K\, N_{\text{ex}}\left(z,\tau-\tau_0\right), \quad 0 < K < 1. \qquad (4.52)$$

An instantaneous FCA$_{\text{TPA}}$ process in the Γ-valley where photoexcited electrons are produced needs phonon assistance and is unlikely.

In the following we consider photoexcited electrons with average lifetime τ_{ex} arising in the active region of cross-section A by TPA from the pump (power P_S, angular frequency ω_S) and probe light (power $P_\times$, angular frequency $\omega_\times$). We describe the dynamics of these carriers by the following rate equation

$$\frac{\partial N_{\text{ex}}(z,\tau)}{\partial \tau} = -\frac{\Delta g_{\text{TPA},S}(z,\tau) P_S(z,\tau)}{2A\hbar\omega_S} - \frac{\Delta g_{\text{TPA},\times}(z,\tau) P_\times(z,\tau)}{2A\hbar\omega_\times} - \frac{N_{\text{ex}}(z,\tau)}{\tau_{\text{ex}}}. \qquad (4.53)$$

The first term on the right-hand side is positive and apart from the factor $1/2$ whose origin has been already explained (see Eq.(4.24)), represents the local density of photons absorbed per second from both, pump and probe light. The second term is negative and accounts for the loss of photoexcited electrons. By setting $P_S = P_\times = 0$ one can verify that τ_{ex} is the photoexcited carrier lifetime. The double heterostructure confines all carriers in the active region, i.e., one can assume that the carriers are distributed over the cross-section A. In the stationary regime $\partial N_{\text{ex}}/\partial\tau = 0$ holds, and the concentration of photoexcited electrons can be calculated from

$$N_{\text{ex}}\left(z,\tau\right) = -\frac{\tau_{\text{ex}}}{2A}\left[\frac{\Delta g_{\text{TPA},S}\left(z,\tau\right)P_S\left(z,\tau\right)}{\hbar\omega_S} + \frac{\Delta g_{\text{TPA},\times}\left(z,\tau\right)P_\times\left(z,\tau\right)}{\hbar\omega_\times}\right]. \tag{4.54}$$

For closely neighbored frequencies $\omega_S \approx \omega_\times \approx \omega_0$ one can substitute Eqs. (4.43) and (4.44) in Eq. (4.54). The contributions proportional to $P_S^2\left(z,\tau\right)$, $P_\times^2\left(z,\tau\right)$ and $2r_{\text{TPA}}P_S\left(z,\tau\right)P_\times\left(z,\tau\right)$ enter with the same weight and represent the three kinds of aforementioned TPA-processes, two degenerate and one nondegenerate TPA-processes. For a sufficiently weak probe light (see Appendix C), one can neglect the terms containing $P_\times\left(z,\tau\right)$ such that $N_{\text{ex}}\left(z,\tau\right)$ becomes independent of the TPA non-degeneracy factor r_{TPA},

$$N_{\text{ex}}\left(z,\tau\right) = -\tau_{\text{ex}}\Delta g_{\text{TPA}}\left(z,\tau\right)\frac{P_S\left(z,\tau\right)}{2\hbar\omega_0 A}. \tag{4.55}$$

By substituting Eqs. (4.52), (4.55) and (4.39) into the right-hand side of the Drude formula (Eq. (4.51)), one gets

$$\Delta n_{\text{FCA}}\left(z,\tau\right) = -\frac{c}{\omega_0}g_0\eta_{\text{FCA}}\varepsilon_{\text{TPA}}P_S^2\left(z,\tau-\tau_0\right),\ \eta_{\text{FCA}} = \frac{Ke^2\tau_{\text{ex}}}{4\varepsilon_0\hbar c m_{\text{FCA}}\omega_0^2 n_0 A}. \tag{4.56}$$

The dependency of Δn_{FCA} on the power squared qualifies the FCA_{TPA} process as a fifth-order nonlinear optical effect (see Eq. (1.9)). According to the assumption that TPA-induced free carrier absorption has a negligible gain coefficient Δg_{FCA}, the nonlinear susceptibility $\chi^{(5)}$ [67] is real and is proportional to the product $\eta_{\text{FCA}}\varepsilon_{\text{TPA}}$. Although both factors in this product are measured in $1/\text{W}$, η_{FCA} cannot represent a compression coefficient and will be simply termed as nonlinear (optical) coefficient. The FCA$_{\text{TPA}}$ phase contribution, Eq. (4.21), can be found by integration over the SOA length. As before we use the approximation from Eq. (4.25) to replace $P_S(z,\tau)$ by $P_{\mathrm{CD}}(z,\tau)$, perform the integral with the methods developed in Appendix B, and obtain

$$\Delta\varphi_{\mathrm{FCA}}(\tau)=\eta_{\mathrm{FCA}}\varepsilon_{\mathrm{TPA}}\left[\exp(h_0)-1\right]^2 C_2(\tau-\tau_0)P_{\mathrm{in}}^2(\tau-\tau_0). \qquad (4.57)$$

The function $C_2(\tau)$ is related to the function $C_1(\tau)$ given in Eq. (4.49) by the expression

$$C_2(\tau)=\frac{C_1(\tau)-\left[\exp(h_0)-1\right]^{-1}\left\{\exp\left[h_0+\Delta h_{\mathrm{CD}}(\tau)\right]-1\right\}}{\exp\left[\left|\Delta h_{\mathrm{CD}}(\tau)\right|\right]-1}. \qquad (4.58)$$

As the FCA$_{\mathrm{TPA}}$ effect is significant, most of the electrons produced by TPA in the conduction band will have an average lifetime close to τ_0, i.e., one also expects $\tau_{\mathrm{ex}}\gtrsim\tau_0$. On the other hand, the validity of the steady-state solution, Eq. (4.55), requires τ_{ex} to be shorter than the pulse width. The large value of η_{FCA} (see Table 4.1) leads to a strong decrease of the refractive index. Notice that the corresponding phase shift contribution starts changing later, with a time delay τ_0 after the input pulse peak.

Summary

By definition, the power amplification of a light signal is the ratio of the output to the input signal power. For a graphical representation of $P_S(0,\tau)=P_{\mathrm{in}}(\tau)$ and $P_S(L,\tau)=P_S^{\mathrm{out}}(\tau)$, see Fig. 4.4(a). Inserting Eqs. (4.33), (4.38) and (4.50), into the third formula in Eq. (4.18), one obtains

$$\Delta h_S(\tau)=\Delta h(\tau)=\Delta h_{\mathrm{BF}}(\tau)+\Delta h_{\mathrm{SHB}}(\tau)+\Delta h_{\mathrm{CH}}(\tau)+\Delta h_{\mathrm{TPA}}(\tau). \qquad (4.59)$$

In the pump-probe experiments the overall SOA power gain

$$G(\tau)=\exp\left[h_\times(\tau)\right]=\exp\left[h_0+\Delta h_\times(\tau)\right] \qquad (4.60)$$

is always given by the probe light amplification. It is represented in Fig. 4.4(b) for a CW probe light. The logarithmic integrated gain $\Delta h_\times(\tau)$ differs from $\Delta h_S(\tau)$ by replacing $\Delta h_{\mathrm{TPA},S}(\tau)$ with $\Delta h_{\mathrm{TPA},\times}(\tau)$ (see Eq. (4.46)),

$$\Delta h_\times(\tau)=\Delta h_{\mathrm{BF}}(\tau)+\Delta h_{\mathrm{SHB}}(\tau)+\Delta h_{\mathrm{CH}}(\tau)+r_{\mathrm{TPA}}\Delta h_{\mathrm{TPA}}(\tau). \qquad (4.61)$$

According to the discussion in Section (ii), we will assume that SHB does not contribute to the phase shifts $\varphi_S^{\text{out}}(\tau)$, and set the corresponding α -factor $\alpha_{\text{SHB}} = 0$. By substituting Eqs. (4.33), (4.38), (4.50) and (4.57) in Eq. (4.22) we find

$$\begin{aligned}\varphi_S^{\text{out}}(\tau) &= \varphi^{\text{out}}(\tau) \\ &= \tfrac{1}{2}\left[\alpha_{\text{BF}}\Delta h_{\text{BF}}(\tau) + \alpha_{\text{CH}}\Delta h_{\text{CH}}(\tau) + \alpha_{\text{TPA}}\Delta h_{\text{TPA}}(\tau)\right] + \Delta\varphi_{\text{FCA}}(\tau).\end{aligned} \tag{4.62}$$

The phase shift $\Delta\varphi_\times(\tau)$ of the probe light is related to the change in the refractive index, $\Delta n_\times(\tau)$, see Eq. (4.16), and is schematically depicted in Fig. 4.4(c). The quantity $\varphi_\times^{\text{out}}(\tau)$ is obtained in a similar way as $\varphi_S^{\text{out}}(\tau)$ by taking into account Eq. (4.47),

$$\varphi_\times^{\text{out}}(\tau) = \tfrac{1}{2}\left[\alpha_{\text{BF}}\Delta h_{\text{BF}}(\tau) + \alpha_{\text{CH}}\Delta h_{\text{CH}}(\tau) + r_{\text{TPA}}\alpha_{\text{TPA}}\Delta h_{\text{TPA}}(\tau)\right] + \Delta\varphi_{\text{FCA}}(\tau). \tag{4.63}$$

As an example, we calculate the gain dynamics of an SOA, driven with a Gaussian input pump pulse having $3.8\,\text{mW}$ peak power and a full width at half maximum (FWHM) of $2.8\,\text{ps}$, i.e., with a pump input energy of $11.3\,\text{fJ}$. The parameters given in Table 4.1 are typical for an SOA being operated at a wavelength of $1.55\,\mu\text{m}$ corresponding to a frequency of about $f_0 = \omega_0/(2\pi) = 193.4\,\text{THz}$. According to [48] the carrier lifetime τ_s lies in the range $100\,\text{ps} \ldots 1\,\text{ns}$. By taking $\tau_s = 100\,\text{ps}$ and by choosing $P_{\text{sat}} = 50\,\text{mW}$, one obtains a saturation energy $W_{\text{sat}} = P_{\text{sat}}\tau_s = 5\,\text{pJ}$ in agreement with the typical range of $5 \ldots 10\,\text{pJ}$ reported in [17]. The α -factors are taken from [43].

We postpone the discussion of the other parameters to the end of Subsection 4.3.4 and first calculate the optical spectra, which we then compare to measured data.

*Table 4.1. List of parameters used to calculate SOA gain and phase shift dynamics. * indicates typical value for the intraband process relaxation time, though not resolved in this work.*

Process	BF	CH	SHB	TPA	$\mathrm{FCA_{TPA}}$
Unsaturated device gain	$h_0 = 6$	—	—	—	—
Sat. power & nonlinearity coefficient	$P_{\mathrm{sat}} = 50\,\mathrm{mW}$	$\varepsilon_{\mathrm{CH}} = 0.5\,\mathrm{W}^{-1}$	$\varepsilon_{\mathrm{SHB}} = 0.3\,\mathrm{W}^{-1}$	$\varepsilon_{\mathrm{TPA}} = 0.25\,\mathrm{W}^{-1}$	$\eta_{\mathrm{FCA}} = 15\,\mathrm{W}^{-1}$
TPA non-degeneracy factor	$r_{\mathrm{TPA}} = 1$	—	—	—	—
α -parameter	$\alpha_{\mathrm{BF}} = 3.8$	$\alpha_{\mathrm{CH}} = 0.7$	$\alpha_{\mathrm{SHB}} = 0$	$\alpha_{\mathrm{TPA}} = -3$	—
Carrier lifetime & intervalley scattering time	$\tau_s = 100\,\mathrm{ps}$	$\tau_{\mathrm{CH}} = 600\,\mathrm{fs}^*$	$\tau_{\mathrm{SHB}} = 100\,\mathrm{fs}^*$	—	$\tau_0 = 1\,\mathrm{ps}$
Gain reduction at saturation onset	$q = 0.017\,\mathrm{dB}$	—	—	—	—

The results of the calculated gain and phase shift dynamics are plotted in Fig. 4.5. They are in agreement with the measured gain and phase dynamics from pump-probe experiments [35, 42, 43]. Starting with the basic BF contribution, we successively add the contributions of the other processes, and are able to see how each process contributes individually to the overall gain. An important feature of the plots is the delay between the gain minimum and the refractive index maximum. This was shown experimentally and theoretically by others [35, 42, 43] and is also confirmed by our model.

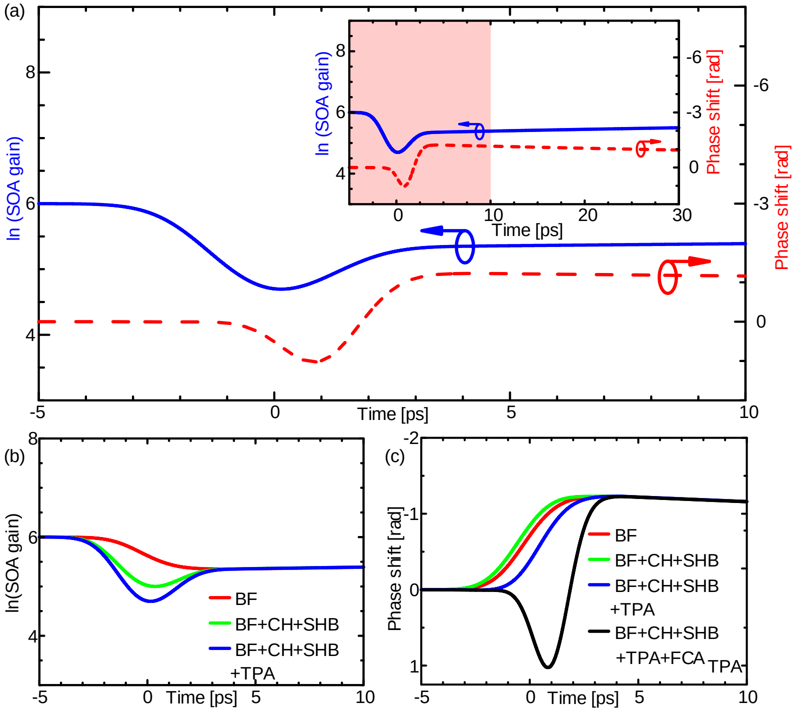

Fig. 4.5 Calculated time dependence of SOA gain $G=\exp(h_\times)$*. The origin* $\tau=0$ *of the retarded time coincides with the maximum of the pump pulse* $P_S(0,\tau)$*, see Fig. 4.4. With our model we calculate* $\ln(G)=h_\times$ *and the phase shift* $\Delta\varphi_\times=-k_0\Delta n_\times$*. (a) Gain and phase shift as a function of retarded time. The inset shows a blow-up. (b) Gain and (c) phase contributions of the various effects. (BF: Band filling; TPA: Two-photon absorption; FCA*$_{\text{TPA}}$*: TPA-induced free carrier absorption delayed by the intervalley scattering time* $\tau_0=1\,\text{ps}$*; SHB: Spectral hole burning; CH: Carrier heating).*

Since the FCA$_{\text{TPA}}$ process starts $\tau_0=1\,\text{ps}$ later than the TPA itself, the refractive index is stationary during this delay (Fig. 4.5(c)). Notice that due to the fast and ultrafast saturation effects the refractive index minimum is reached somewhat earlier than 1 ps. Neglecting Δg_{FCA} can only be compatible with moderately high TPA effects in bulk SOAs. In such cases there are fewer free carriers arising during the FCA$_{\text{TPA}}$ process than removed by carrier depletion. However, the absorption cross-sections calculated in [55] are in the order of the BF differential gain. This fact can satisfactorily explain the dramatic FCA$_{\text{TPA}}$ phase shift shown in Fig. 4.5(c) by simultaneously keeping the negligible free carrier absorption stipulated in Fig. 4.5(b). The topic is thoroughly discussed in Appendix A.

The advantage of using this approach is the ability to analytically model the temporal gain dynamics with the few parameters of Table 4.1. Most of these parameters can be derived by fitting the calculated spectrum to the measured one. The model does not require details on the geometry and on the other SOA parameters which typically are inaccessible.

4.3.4 Pump and probe light spectra at SOA output: comparison of model and measurements with experiment

The closed form expressions for the gain and phase dynamics, in which only a few constant parameters are chosen independently, allows us to derive the spectral shapes and to compare them with the experiment. Moreover, one can determine the remaining constant parameters by fitting the spectral traces and hence get a better understanding of the dynamic behavior of an SOA at the respective operation point. The model parameters discussed at the end of this section are found to be within a $\pm 10\%$ spread of their absolute extracted values.

In the following we assume that the condition $P_{\text{in0}} > P_{\times}$ is met, and P_{in0} denotes the peak power of the pump pulse $P_{\text{in}}(\tau)$, i.e., $P_{\text{in0}} = \max\left[P_{\text{in}}(\tau)\right]$ and $P_{\times}$ is the CW probe light power. We also assume – as before – that the pump and CW frequencies are not too far apart. According to Eqs. (4.61) and (4.63), one needs an additional parameter, the TPA non-degeneracy factor r_{TPA}, for describing the amplification and the phase shift of the probe light. Only if $r_{\text{TPA}} \approx 1$ holds, the propagation of a weak probe light does not influence the active medium. Since the SOA material is assumed to have a negligible dispersion, we can use the same values of the constant parameters other than r_{TPA}, for both signals.

For a comparison with the experiment, we calculate the one-sided power spectra $\Theta_{S,\times}$ for the real optical pump (subscript *S*) and probe (subscript ×) fields at the SOA output. Starting with the output normalized RMS electric fields $E^{\text{out}}_{\gamma S,\times}(t)$ as given by Eq. (4.4), we perform the Fourier transform of the real part $\Re\left\{E^{\text{out}}_{\gamma S,\times}(t)\right\}$. We then shift it from the carrier angular frequencies

$\omega_{S,\times}$ to the baseband, observe a factor of $1/2$ for the one-sided transform, take the modulus square and express the resulting power spectrum versus the frequency shift $f=\left(\omega-\omega_{S,\times}\right)/\left(2\pi\right)$,

$$\Theta_{S,\times}\left(f\right)=\left|\frac{1}{2}\int_{-\infty}^{\infty}\sqrt{P^{\text{out}}_{\gamma S,\times}\left(t\right)}\exp\left[\mathrm{j}\varphi^{\text{out}}_{\gamma S,\times}\left(t\right)\right]\exp\left[-\mathrm{j}\left(k_0 n_0 L+2\pi f t\right)\right]\mathrm{d}t\right|^2 . \quad (4.64)$$

The powers and phase shifts of the output signals are obtained in terms of $\Delta h_{S,\times}\left(\tau\right)$ (Eqs. (4.59) and (4.61)) and $\varphi^{\text{out}}_{S,\times}\left(\tau\right)$ (Eqs. (4.62) and (4.63)). Writing

$$P^{\text{out}}_{S}\left(\tau\right)=\exp\left[h_0+\Delta h_S\left(\tau\right)\right]P_{\text{in}}\left(\tau\right) \text{ and } P^{\text{out}}_{\times}\left(\tau\right)=\exp\left[h_0+\Delta h_\times\left(\tau\right)\right]P_\times , \quad (4.65)$$

the retarded time dependencies from Eqs. (4.9) and (4.10) allow to express the optical spectra as

$$\Theta_{S,\times}\left(f\right)=\left|\frac{1}{2}\int_{-\infty}^{\infty}\sqrt{P^{\text{out}}_{S,\times}\left(\tau\right)}\exp\left[\mathrm{j}\varphi^{\text{out}}_{S,\times}\left(\tau\right)\right]\exp\left(-\mathrm{j}2\pi f\tau\right)\mathrm{d}\tau\right|^2 . \quad (4.66)$$

The calculated and measured spectra of the pulse and probe light at the SOA output are shown in Fig. 4.6(a) and Fig. 4.6(b). Mode-locked pulses with a $2.8\,\text{ps}$ FWHM are generated at the repetition rate of $10\,\text{GHz}$ in order to allow the complete CR between two successive pulses. Pump and probe light are injected in co-propagating direction into the SOA, utilizing a 3 dB coupler. The spectra were recorded by an optical spectrum analyzer with a resolution bandwidth of $0.1\,\text{nm}$, and correspond to the envelope of the oscillatory structure related to the pulse repetition rate.

Pulse spectra help investigating the dynamics of the gain and refractive index. Due to the short pulse duration of a few picoseconds, only nonlinear effects that occur while the pump is present show up in the output spectrum of the pump. Whereas, the probe senses both the ultrafast effects that occur when the pump is present and also the slower effects like CR that do not influence the pump. Hence, the temporal limitation of the injected optical power acts as a gating mechanism which allows to get insight of the dynamics at the beginning, while suppressing later effects. The full dynamics of the SOA gain and refractive index can be concluded from the probe light spectra. Although possibly significant effects such as spectral artifacts [48] and amplified spontaneous emission (ASE) were not included in the analytical model, the calculated spectra (solid black lines) resemble the measured ones (light grey lines). For instance, one observes the pronounced sidelobes in the blue-shifted spectral domain of calculated and measured pump and probe spectra. The origin of this spectral region can be traced back to the FCA_{TPA} nonlinear effect – as described by the parameters η_{FCA} and τ_0 (see Fig. 4.6(c) and Fig. 4.6(d)).

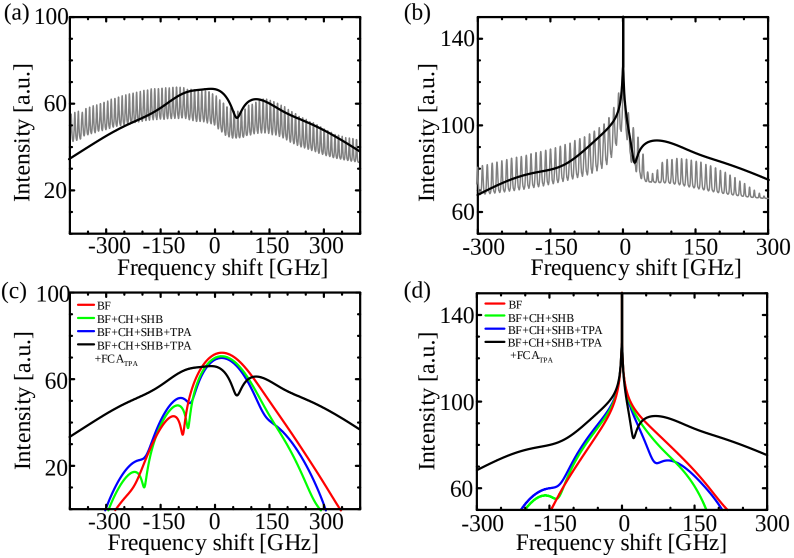

Fig. 4.6 Calculated spectra (log scale) using the parameters from Table 4.1 and comparison with measured ones. (a) Measured (light gray lines) and calculated (solid black lines) spectra after the SOA of the pump pulse and (b) measured (light gray lines) and calculated (solid black lines) spectra after the SOA of the probe light. The decomposition of the spectra is shown in (c) for the pump pulse and in (d) for the CW pulse light. (BF: Band filling; TPA: Two-photon absorption; FCA_{TPA}: Free carrier absorption induced by TPA; SHB: Spectral hole burning; CH: Carrier heating).

Both measured and simulated probe light spectra have broad and pronounced red-shifted spectral components extending beyond $-200\,\text{GHz}$ with respect to the center frequency, see Fig. 4.6(b). They mainly originate from CD and CH effects. Towards higher frequencies with respect to the center frequency one can notice two blue-shifted spectral regions. First, there is a blue-shifted spectral range starting closely to the carrier frequency.

This can be attributed to the slow carrier recovery process. We attribute the small blue-shifted shoulder with a peak around $100\,\mathrm{GHz}$ to the presence of both TPA and FCA$_{\mathrm{TPA}}$ nonlinear effects, Fig. 4.6(d).

Other researchers have found similar spectral characteristics, particularly when experiments have been performed with short pulses of $1\,\mathrm{ps}$ [50] and $2\,\mathrm{ps}$ [51]. The discussion here has shown that the presence or absence of spectral components gives an indication for the occurrence and strength of a particular nonlinear effect. Specifically, one expects a distinct blue-shifted sidelobe far off from the center frequency in the presence of TPA and FCA$_{\mathrm{TPA}}$, and a red-shifted spectral component due to CD and CH as well as a blue-shifted spectral component nearby the center frequency due to CR.

In Fig. 4.11 we present pump and probe spectra for different pulse input powers which allow to verify the differences in order of nonlinearity. Note the characteristics behavior of the blue sideband intensity associated with FCA$_{\mathrm{TPA}}$.

The method outlined here allows to easily recognize when TPA and FCA$_{\mathrm{TPA}}$ play a role by just looking at the spectrum and by observing that the ultrafast decrease of the refractive index occurs during the trailing edge of the pump pulse. In addition, the method allows for an estimation of the nonlinear coefficients in a particular SOA at a certain operating point (see, e.g., Table 4.1). For instance, in our experiment we have employed an SOA with the structural parameters from [43]: $L = 2.6\,\mathrm{mm}$, $A = 0.225\,\mu\mathrm{m}^2$, field confinement factor $\Gamma = 0.351$ and $v_g = 8.4\times10^7\,\mathrm{m/s}$. Following [48], we take the TPA effective cross-section to be of the same size as the modal cross-section, $A_{\mathrm{TPA}} = A/\Gamma$. By using Eq. (4.48), we estimate the nonlinear TPA coefficient β_2 from $\varepsilon_{\mathrm{TPA}}$ which is given in Table 4.1, and find a value of $37\,\mathrm{cm/GW}$ which is close to the value of $35\,\mathrm{cm/GW}$ reported in [48] for InGaAsP-SOAs. We also express the ultrafast compression coefficients in m^3 facilitating the comparison with the values given in literature: $\varepsilon_{\mathrm{CH}} = 3.5\times10^{-24}\,\mathrm{m}^3$ and $\varepsilon_{\mathrm{SHB}} = 2.1\times10^{-24}\,\mathrm{m}^3$.

We now look for the remaining parameters q, η_{FCA}, τ_0 and r_{TPA}. A reduction of the gain by $q = 0.01\,\mathrm{dB}$ compared to the unsaturated gain marks the beginning of saturation and corresponds to a time $\tau_{\mathrm{R}} = 3.3\,\mathrm{ps}$ for a transition from CD to CR and to a ratio of the output pulse power at τ_{R}, $P_S^{\mathrm{out}}\left(\tau_{\mathrm{R}}\right)$, to the peak output power, $P_S^{\mathrm{out,peak}}$,

$$X_{\mathrm{R}} = P_S^{\mathrm{out}}\left(\tau_{\mathrm{R}}\right) / P_S^{\mathrm{out,peak}} = 4\% \, . \tag{4.67}$$

We could not see any spectral change for $q < 0.03\,\mathrm{dB}$ or, equivalently, for $X_{\mathrm{R}} < 9.5\%$, i.e., for transition times from CD to CR larger then $2.9\,\mathrm{ps}$. The value $q = 0.017\,\mathrm{dB}$ reported in Table 4.1 corresponds to $\tau_{\mathrm{R}} = 3.1\,\mathrm{ps}$ and a ratio $X_{\mathrm{R}} = 6\%$.

In order to assign values to the remaining fit-parameters, a sensitivity analysis has been performed. For this purpose, we consider the relative error

$$F_{S,\times}\left(f\right) = \frac{\left|\Theta_{S,\times\,\mathrm{measured}}\left(f\right) - \Theta_{S,\times\,\mathrm{calculated}}\left(f\right)\right|}{\Theta_{S,\times\,\mathrm{measured}}\left(f\right)} \, , \tag{4.68}$$

and denote its averaged value over the whole measured spectrum with $\left\langle F_{S,\times} \right\rangle$. We determine by calculation the changes of a single parameter leading, or corresponding to a minimum of $\left\langle F_{S,\times} \right\rangle$. We then look for physical or model dependent reasons impeding the realization of this minimum. As a plausibility check, the parameter q is a useful indicator for the onset of carrier saturation. It also stands for a time τ_{R}, which has to be longer than the pulse duration (FWHM of the pump pulse). Approximate values for τ_0 and r_{TPA} result from their physical meanings and can be used as a first guess in the optimization algorithm. The value $\eta_{\mathrm{FCA}} = 15\,\mathrm{W}^{-1}$ in Table 4.1 can be subsequently determined from the agreement of the calculated and measured spectra. The relative error averaged over the whole measured probe light spectrum $\left\langle F_{\times} \right\rangle$ has a minimum for $q = 0.017\,\mathrm{dB}$. By keeping this value for q constant, a sensitivity analysis has been performed for the parameters η_{FCA}, τ_0 and r_{TPA}. The following ranges have been established in this way: $14.5 \ldots 15.5\,\mathrm{W}^{-1}$ for η_{FCA}, $0.9 \ldots 1.1\,\mathrm{ps}$ for the $\Gamma \rightarrow \mathrm{X}$ intervalley scattering time τ_0 and $0.9 \ldots 1.1$ for the TPA non-degeneracy factor r_{TPA}. Recalling that $r_{\mathrm{TPA}} = 1$ describes the TPA-process for the pump alone, we conclude that in our measurements, the probe light has no measurable effect on the active medium.

4.4 Selecting spectral regions to perform optical filter based wavelength conversion

The previous subsection has shown that nonlinear effects in an SOA lead to unique spectral traces. With our model, we can estimate their qualitative and quantitative relevance. This information is useful to judge if a particular effect is present at all, and if it is sufficiently large to be exploited in a nonlinear experiment.

There are three distinct spectral ranges which feature strong nonlinear effects. We now discuss the SOA with respect to its capability to perform all-optical signal processing by exploiting the nonlinear cross-gain modulation (XGM) and cross-phase modulation (XPM) effect.

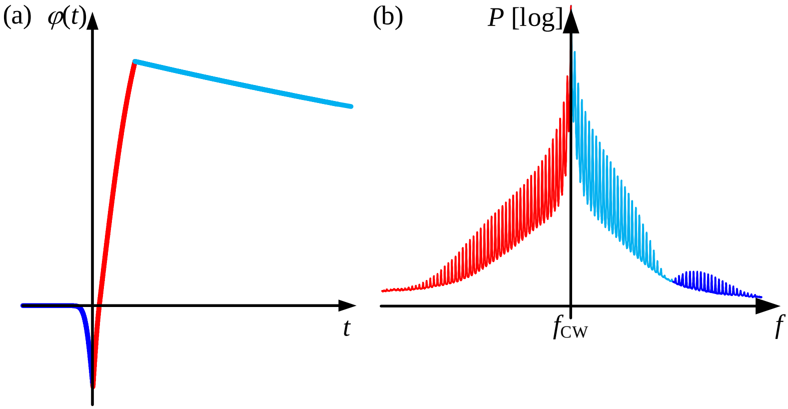

Fig. 4.7 (a) Phase shift dynamics and (b) corresponding induced spectral components in a measured probe light spectrum.

The basic features within the phase dynamics and the spectral components as seen by a probe light are schematically depicted in Fig. 4.7. Both figures are derived from the plots in Fig. 4.5(c) and Fig. 4.6(b). The colors indicate three temporal regions associated with three distinct nonlinear effects as discussed in Fig. 4.4(c). In the previous section we have shown that the dominant nonlinear effects in the three different temporal regions yield clear spectral traces in different spectral regions. So, for instance, the blue-shifted (BS) shoulder away from the central frequency (shown in dark blue) is due to the ultrafast sharp decrease of the refractive index due to TPA and $\mathrm{FCA}_{\mathrm{TPA}}$ in the first time segment. Next, the strong red-shifted (RS) spectral component (shown in red color) is mainly induced by the carrier depletion in the SOA. Finally, the spectral component close to the CW (in light blue color) results from the carrier recovery in the active medium. Note that a fast CR process causes a broad component.

Thus, SOA nonlinear effects create new spectral components, first in the far blue, then in the red and again in the near blue spectral domain [70]. By combining an SOA with properly adjusted optical filters one can build simple and efficient all-optical wavelength converters.

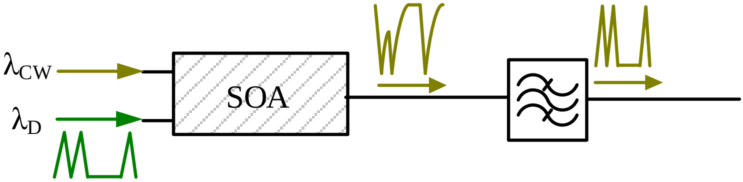

Fig. 4.8 Scheme of an optical filter based all-optical wavelength conversion system.

A wavelength converter generating non-inverted signals is schematically depicted in Fig. 4.8. Using suitable red-shifted optical filters (RSOF) after an SOA, a wavelength converter can be realized. In [71], a 10 Gbit/s and a 40 Gbit/s all-optical regeneration experiment has been performed with a red-shifted optical filter offset by about 50 GHz from the center frequency. In another demonstration, the blue spectral range close to the CW carrier has been exploited for performing all-optical wavelength conversion, using blue-shifted optical filtering (BSOF). In [72], a BSOF experiment where the filter is offset by approximately 60 GHz has been demonstrated at 40 Gbit/s .

Finally, the ultra-fast nonlinear TPA and FCA_{TPA} effects can be used. While the power in the spectral component is lowest, this spectral component is created by the fastest nonlinear effect. Since this effect does not depend on the carrier density, there is no contribution from the carrier dynamics that suffer from patterning effects. The spectral contribution due to FCA_{TPA} is very distinctive in the output probe spectrum and its presence in the spectrum is clearly recognizable. One would immediately know of the presence of the ultrafast FCA_{TPA} effects in their SOA and be able to optimize the experimental conditions in order to maximize this FCA_{TPA} contribution for their optical signal processing needs. Indeed, successful patterning free all-optical wavelength conversion at 320 Gbit/s has been demonstrated [73]. In that experiment, the filter was offset by more than 150 GHz from the center frequency, where we previously identified the dominant nonlinear TPA and FCA_{TPA} spectral component. By combining both filter types, RSOF and BSOF, a pulse reformatting optical filter (PROF) has been realized and tested with signals up to 40 Gbit/s [74, 75].

The PROF works as follows: The signal after the SOA is split into two copies. One signal copy is routed through an RSOF, delayed and attenuated with respect to the second copy which passes a BSOF. The introduced delay compensates for the group delay difference between RS and BS components. Both modified signal copies, which contain only parts of the BS and RS components, are superimposed after being equalized in power and group delay such that a return-to-zero (RZ) signal at the novel wavelength will result. All-optical wavelength conversion supported by RSOF, BSOF or PROF leads to a signal consisting of Fourier transform limited pulses.

By properly offsetting the filter, each of the three spectral regions in Fig. 4.7(b) can be used to induce a progressive phase shift between subsequent pulses. This way RZ, vestigial sideband (VSB) and carrier-suppressed return-to-zero (CSRZ) signals can be generated [76-78]. In this work we have concentrated on the characterization and interpretation of the nonlinear responses of the active medium to Gaussian pulses.

End of paper [54], Section 2.1 to 4.

4.5 Influence of operating parameters on the spectra

Measured output spectra of pump pulse and probe light for different pump powers, probe powers and bias currents are shown in this section. The presented spectra allow to deduce the optimum conditions for the filter-supported wavelength conversion.

An optical pulse entering an SOA perturbs the carrier density and carrier energies in the conduction and valence bands. The perturbation is not constant over the whole gain spectrum, it is strongest at the peak pulse wavelength λ_0. At $\Delta\lambda = |\lambda_0 - \lambda_{\mathrm{CW}}|$ above the peak pump wavelength (see Fig. 4.9(a)) the perturbation is weaker than at the same $\Delta\lambda$ below the peak pump wavelength (see Fig. 4.9(b)). The perturbation is even weaker for a larger $\Delta\lambda$ below the peak pump wavelength (see Fig. 4.9(c)).

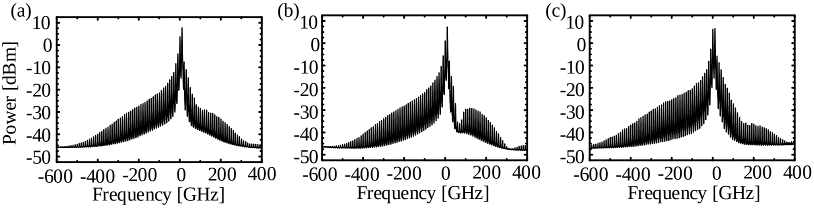

Fig. 4.9 *Output probe light spectra for different wavelengths (a)* $\lambda_{\mathrm{CW}} = 1560\,\mathrm{nm}$*, (b)* $\lambda_{\mathrm{CW}} = 1540\,\mathrm{nm}$*, and (c)* $\lambda_{\mathrm{CW}} = 1535\,\mathrm{nm}$*. The spectra are centered on the respective CW frequencies. The SOA was biased at* $I = 400\,\mathrm{mA}$*. The pump pulses of* $2.8\,\mathrm{ps}$ *FWHM were emitted at a repetition rate of* $f_{\mathrm{rep}} = 10\,\mathrm{GHz}$*. The pump power was* $P_{\mathrm{in}} = 10\,\mathrm{dBm}$ *at a center wavelength of* $\lambda_0 = 1550\,\mathrm{nm}$*. The CW probe light power is* $P_{\mathrm{CW}} = 2\,\mathrm{dBm}$*.*

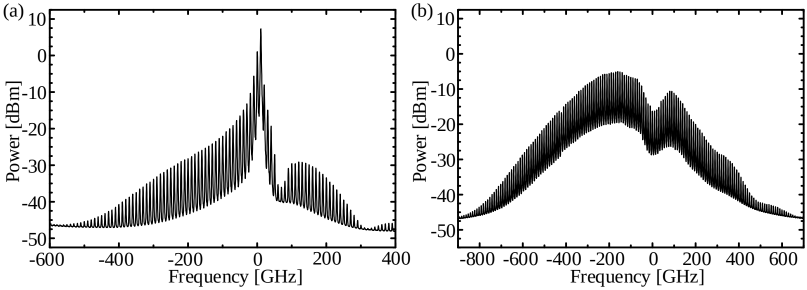

Fig. 4.10 *Optical spectra of (a) probe light and (b) pump pulse train behind an SOA. The pump pulses of* $2.8\,\mathrm{ps}$ *FWHM were emitted at a repetition rate of* $f_{\mathrm{rep}} = 10\,\mathrm{GHz}$*. The pump power was* $P_{\mathrm{in}} = 10\,\mathrm{dBm}$ *at a center wavelength of* $\lambda_0 = 1550\,\mathrm{nm}$*. The CW probe light power was* $P_{\mathrm{CW}} = 2\,\mathrm{dBm}$ *at a wavelength of* $\lambda_{\mathrm{CW}} = 1540\,\mathrm{nm}$*. The SOA was biased at* $I = 400\,\mathrm{mA}$*. The spectra are centered on the CW or input pulse carrier frequencies, respectively.*

Fig. 4.10 shows probe and pump light spectra for a high degree of saturation.

The probe and pump spectra for different input pulse powers P_{in}, probe light powers P_{CW}, and bias currents I are shown in Fig. 4.11, Fig. 4.12 and Fig. 4.13. In all the experiments, the pump pulse of 2.8 ps FWHM is centered on the wavelength 1550 nm, while the CW probe light is centered on 1540 nm.

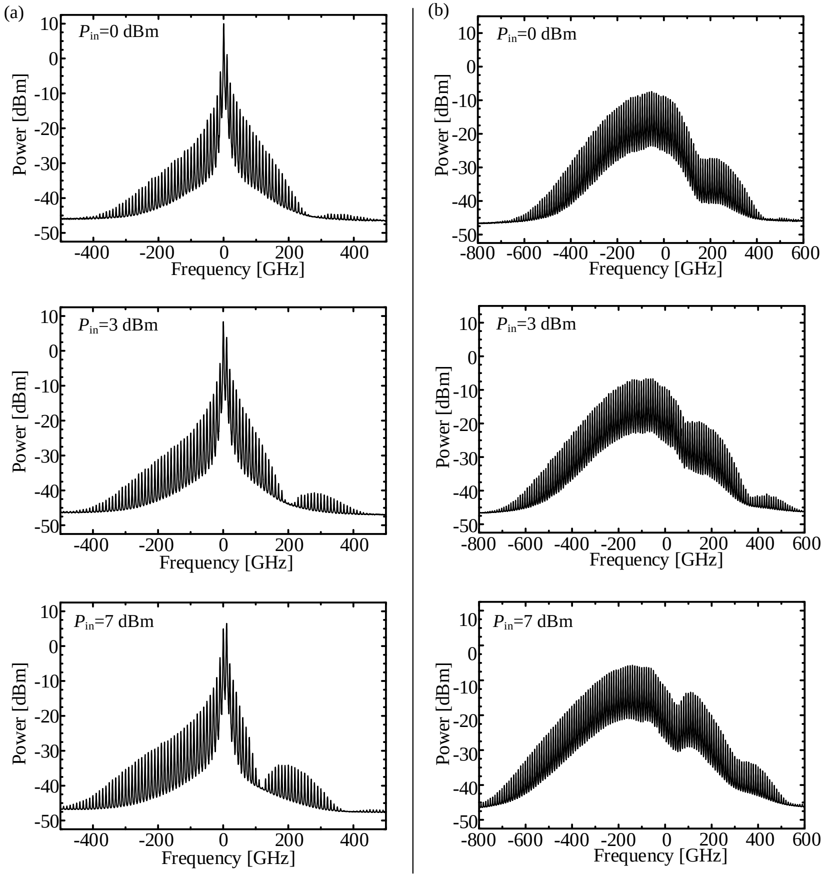

Fig. 4.11. Optical spectra of (a) probe light and (b) pump pulse train behind an SOA for different pump powers $P_{\text{in}} = 0, 3, 7\,\text{dBm}$*. The pump pulses of* $2.8\,\text{ps}$ *FWHM were emitted at a repetition rate of* $f_{\text{rep}} = 10\,\text{GHz}$ *. The pump center wavelength was* $\lambda_0 = 1550\,\text{nm}$ *. The CW probe light power was* $P_{\text{CW}} = 2\,\text{dBm}$ *at a wavelength of* $\lambda_{\text{CW}} = 1540\,\text{nm}$ *. The SOA was biased at* $I = 400\,\text{mA}$ *. The spectra are centered on the CW or input pulse carrier frequencies, respectively.*

The pump pulse spectra in Fig. 4.11 show an increasing red shift of the center frequency, i.e., a shift towards lower frequencies. In the probe light spectra, the red shift also affects the blue spectral components but not the center frequency.

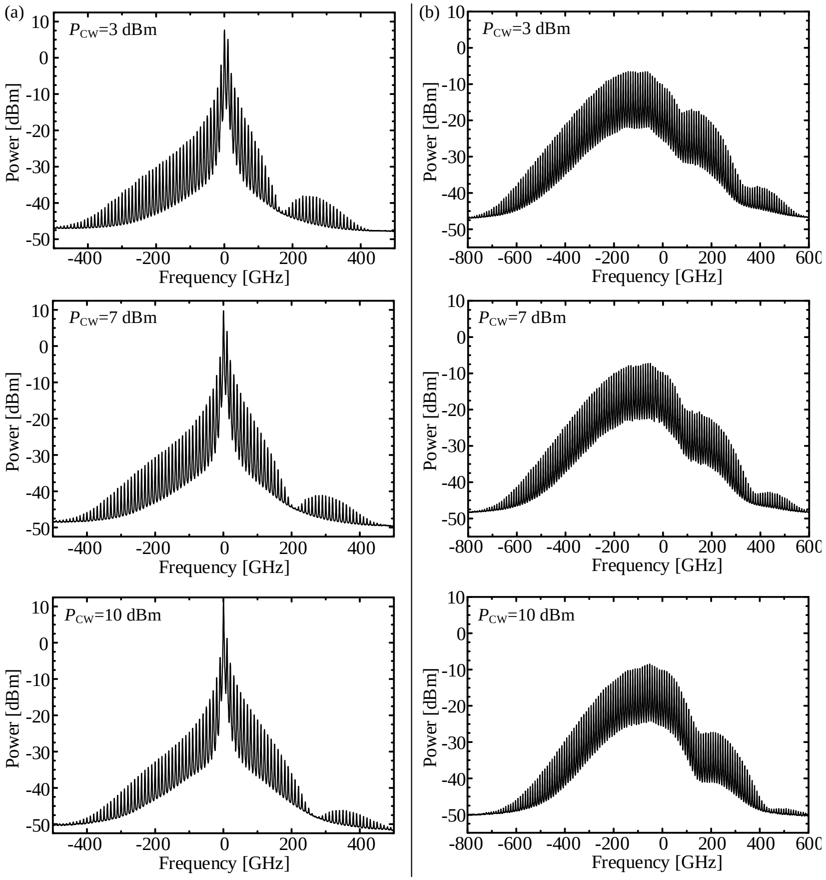

Fig. 4.12. Optical spectra of (a) probe light and (b) pump pulse train behind an SOA for different probe powers $P_{\mathrm{CW}} = 3, 7, 10\,\mathrm{dBm}$. *The pump pulses of* $2.8\,\mathrm{ps}$ *FWHM were emitted at a repetition rate of* $f_{\mathrm{rep}} = 10\,\mathrm{GHz}$. *The pump power was* $P_{\mathrm{in}} = 5\,\mathrm{dBm}$ *at the center wavelength of* $\lambda_0 = 1550\,\mathrm{nm}$. *The probe light wavelength was* $\lambda_{\mathrm{CW}} = 1540\,\mathrm{nm}$. *The SOA was biased at* $I = 400\,\mathrm{mA}$. *The spectra are centered on the CW or input pulse carrier frequencies, respectively.*

For a strong spectral component related to CR, $P_{\mathrm{CW}} > P_{\mathrm{in}}$ is required.

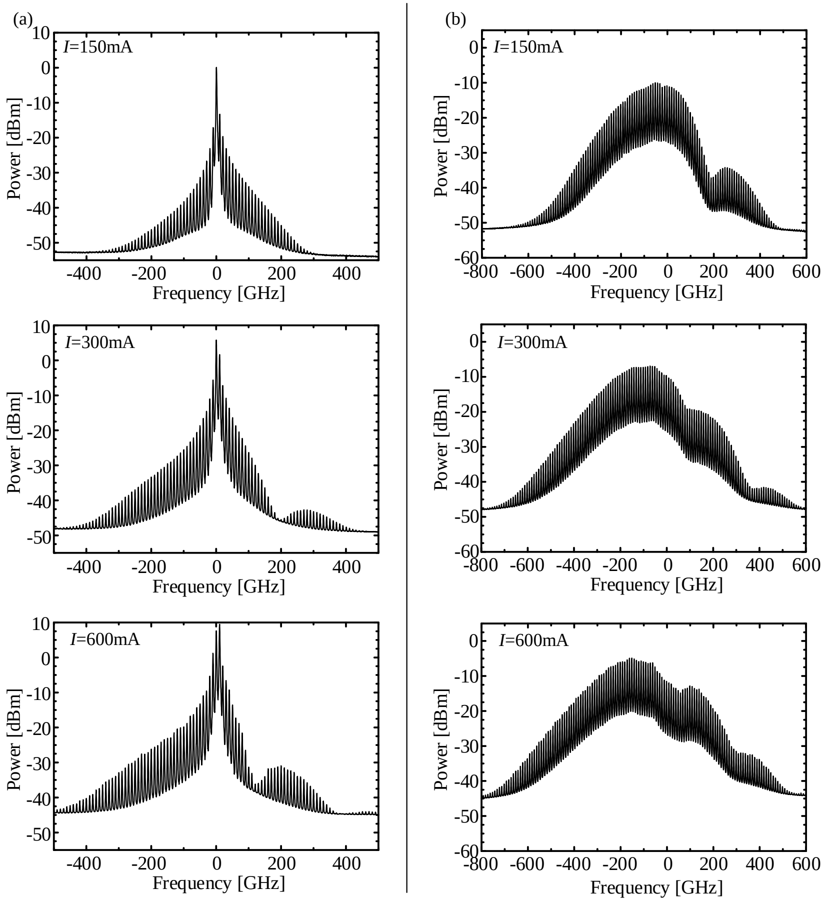

Fig. 4.13. Optical spectra of (a) probe light and (b) pump pulse train behind an SOA for different SOA bias currents $I = 150, 300, 600\,\mathrm{mA}$*. The pump pulses of* $2.8\,\mathrm{ps}$ *FWHM were emitted at a repetition rate of* $f_{\mathrm{rep}} = 10\,\mathrm{GHz}$*. The pump power was* $P_{\mathrm{in}} = 5\,\mathrm{dBm}$ *at the center wavelength of* $\lambda_0 = 1550\,\mathrm{nm}$*. The probe light power was* $P_{\mathrm{CW}} = 2\,\mathrm{dBm}$ *at a wavelength of* $\lambda_{\mathrm{CW}} = 1540\,\mathrm{nm}$*. The spectra are centered on the CW or input pulse carrier frequencies, respectively.*

The main outcome of the evaluation of the measured spectra:

- By increasing P_{in} or I, the ultrafast spectral components become stronger and the spectra of the output pulse becomes more red-shifted.
- In our measurements the 100 ps time interval between two pulses is longer than the duration of the pulse-SOA interaction and CR. For this reason, the measured probe light spectra contain spectral components for the modulated parts and for the unmodulated part. Only the spectral components associated with the modulated parts – consisting of red, blue and ultrafast blue components – are red-shifted, whereas the center frequency f_{CW} is not shifted.
- The observed red-shift for the pump and probe spectra is due to the spectral artifact and to the spatial decrease of carrier density along the SOA. The spectral artifact [48] is defined as the wavelength dependence of the SOA gain profile. The spatial decrease of carrier density along the SOA explains why the spectral shift increases with the input pulse power P_{in} [49] and bias current I.
- The increasing depletion along the length of the SOA reduces the carrier concentration and translates both, the gain maximum and the transparency point towards longer wavelengths.
- A spectral shift changes the central angular frequency ω_0 by an amount determined by the part of the output phase shift $\varphi(t)$ which is linear in time. This linear part can be separated with help of a Taylor expansion of $\varphi(t)$ around $t=0$,

$$\varphi(t)=\left.\frac{\mathrm{d}\varphi}{\mathrm{d}t}\right|_{t=0} t+\varphi_{\mathrm{chirp}}(t)\,, \tag{4.69}$$

- where the dot superscript means the time derivation, $\varphi_{\mathrm{chirp}}(t)$ gathers together all terms nonlinear in time, and $\varphi(0)$ has been omitted since it plays no role in the spectrum. By using Eq. (4.69) the formula for the optical spectrum (see Eq. (4.64)) gets modified into

$$\left|\frac{1}{2}\int_{-\infty}^{\infty}\sqrt{P^{\mathrm{out}}(t)}\exp\left\{-\mathrm{j}\left[\left(\omega-\left(\omega_0+\left.\frac{\mathrm{d}\varphi}{\mathrm{d}t}\right|_{t=0}\right)\right)t-\varphi_{\mathrm{chirp}}(t)\right]\right\}\mathrm{d}t\right|^2, \quad (4.70)$$

- showing that the central angular frequency ω_0 has been shifted by the amount $\left.(\mathrm{d}\varphi/\mathrm{d}t)\right|_{t=0}$. Thus, a spectral red-shift occurs whenever the slope is negative, i.e., for $\left.(\mathrm{d}\varphi/\mathrm{d}t)\right|_{t=0}<0$.
- According to Eq. (4.69), the change of the refractive index has also a part linear in time. If we first neglect the position dependency, we can write an expansion similar to Eq. (4.69) for the change in the refractive index averaged over the SOA length (see Eq. (4.16))

$$\Delta n(t)=\left.\frac{\mathrm{d}\Delta n}{\mathrm{d}t}\right|_{t=0}t+\Delta n_{\mathrm{chirp}}(t), \quad (4.71)$$

- with $\left.(\mathrm{d}\Delta n/\mathrm{d}t)\right|_{t=0}>0$. The figures Fig. 4.11(a), Fig. 4.12(a) and Fig. 4.13(a) show a red-shift of all three components (RS, BS and ultrafast). In particular this means that the first term in Eq. (4.71) is valid during the whole period of time when the refractive index has been modulated.
- Eq. (4.71) implies that a part $\Delta N(t)$ of the total carrier density dynamics suffers a linear decrease in time, $\left.(\mathrm{d}\Delta N/\mathrm{d}t)\right|_{t=0}t$, with $\left.(\mathrm{d}\Delta N/\mathrm{d}t)\right|_{t=0}<0$.
- The optical inhomogeneity of the carrier density (and of the refractive index) can be taken into account by splitting the SOA into homogenous sections, as described in Section 3.2.4. While the linear decrease of the carrier density in each section will be different, e.g., will have the form $\left.(\mathrm{d}\Delta N_i/\mathrm{d}t)\right|_{t=0}t$ in the i-th section, we do not expect large differences in the values of

$\left(\mathrm{d}\Delta N_i/\mathrm{d}t\right)\big|_{t=0}$ at least for adjacent sections. The temporal distortions of the carrier density can be related to the spatial ones by replacing the time t by z_i/v_g, where z_i denotes the average position of the i-th section and v_g the group velocity in the SOA. Since $\left|\left(\mathrm{d}\Delta N_i/\mathrm{d}t\right)\big|_{t=0} z_i/v_g\right|$ grows with z_i, the total density $N_i(t)$ becomes more reduced in the section i that is closer to the output facet, i.e., $z = L$.

- By increasing P_{CW}, the ultrafast blue spectral components of the probe light and the output pulse spectra are both blue-shifted, an effect which is opposite to the increase of the input pulse power and the bias current. In this case the probe light plays the role of a holding beam in the gain region. It weakens the pump pulse effects by diminishing the modulation of the carrier density.

4.6 Filter based all-optical logic functions – a suggestion

The selection of parts of the probe light spectrum after an SOA, does not only allow for wavelength conversion (see 5), but it also allows to realize logic gates. As reported in [79], logic gate functions were implemented based on experimentally determining the SOA operating parameters and the filter properties.

In this section we suggest a method to implement the logic functions AND, OR and XOR based on probe light spectra which are pump power dependent, see Fig. 4.11. It is possible to realize an all-optical gate by proper filtering the spectral components from the probe light.

Two modulated optical return-to-zero (RZ) control signals, D1 and D2, enter an SOA together with a CW probe light. To realize an OR gate at least one control pulse (mark) enters the SOA, whereas for an AND gate it is necessary that control pulses from both signals enter the SOA simultaneously, and for an XOR gate only one out of the two control pulses has to enter the SOA, see Fig. 4.14.

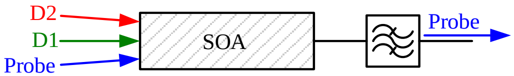

OR			AND			XOR		
D1	D2	Probe	D1	D2	Probe	D1	D2	Probe
0	0	0	0	0	0	0	0	0
1	0	1	1	0	0	1	0	1
0	1	1	0	1	0	0	1	1
1	1	1	1	1	1	1	1	0

Fig. 4.14. Logic gate scheme and Boolean logic.

Having D1 and D2 at the same wavelength λ_0 and at the same control pulse power levels $P_\mathrm{D} = P_\mathrm{D1} = P_\mathrm{D2}$, but orthogonally polarized (to allow the power summation), a comparison of the spectra helps to identify spectral regions for logic functions.

For the analysis, we measured probe light spectra (see Fig. 4.15) at a pulse repetition rate of 10 GHz, which corresponds to a control pulse bit rate of 10 Gbit/s.

In the probe light spectra of Fig. 4.15, the spectral components differ for control pulse powers of $P_\mathrm{D} = 3\,\mathrm{dBm}$, $6\,\mathrm{dBm}$ and $12\,\mathrm{dBm}$. By selecting the power levels for the control pulses D1 and D2 as $P_\mathrm{D} = 3\,\mathrm{dBm}$ we obtain the spectra of Fig. 4.15(a), whereas with the selection of $P_\mathrm{D} = 6\,\mathrm{dBm}$ we obtain the spectra of Fig. 4.15(b).

The following analysis is based on the comparison of the probe light spectra for P_D and $2P_\mathrm{D}$:

- An OR gate is realized when having optical power both spectral regions of the probe light spectra for P_D and $2P_\mathrm{D}$. Here, the summed power of control pulse D1 and D2 corresponds to P_D or $2P_\mathrm{D}$.
- An XOR gate is realized when having optical power only in the spectral region of the probe light spectrum for P_D. Here the summed power of control pulse D1 and D2 corresponds only to P_D.

- An AND gate is realized when having optical power only in the spectral region of the probe light spectrum for $2P_\mathrm{D}$. Here the summed power of control pulse D1 and D2 corresponds only to $2P_\mathrm{D}$.

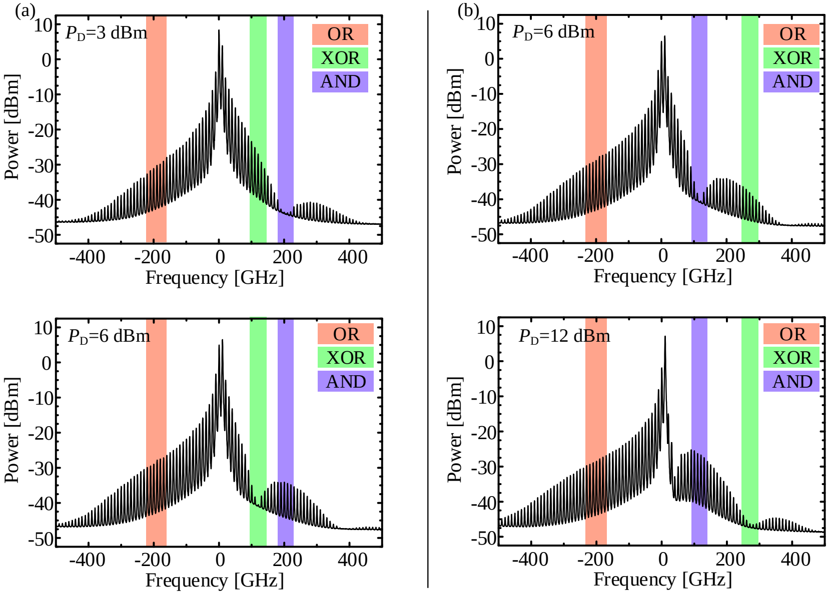

Fig. 4.15. Optical spectra of probe light $\lambda_0 = 1550\,\mathrm{nm}$, $\lambda_\mathrm{CW} = 1540\,\mathrm{nm}$, $P_\mathrm{CW} = 2\,\mathrm{dBm}$ *and* $I = 400\,\mathrm{mA}$ *at a pulse repetition rate for the pump of* $f_\mathrm{rep} = 10\,\mathrm{GHz}$. *(a)* $P_\mathrm{D} = 3\,\mathrm{dBm}$ *and* $P_\mathrm{D} = 6\,\mathrm{dBm}$, *(b)* $P_\mathrm{D} = 6\,\mathrm{dBm}$ *and* $P_\mathrm{D} = 12\,\mathrm{dBm}$.

The order and positions of the spectral regions, corresponding to the different logic gates, depend on the power of the control pulses. With increasing frequency, the order is OR, XOR and AND for $P_\mathrm{D} = 3\,\mathrm{dBm}$, and XOR, AND and OR for $P_\mathrm{D} = 6\,\mathrm{dBm}$.

Performing the same analysis for control pulses at a bit rate of 40 Gbit/s, the spectra do not show the same pronounced spectral regions as before.

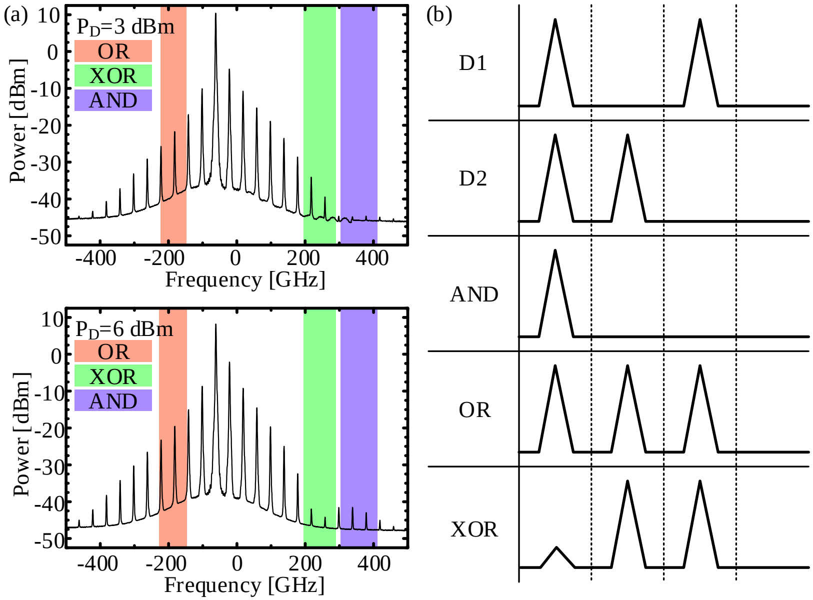

Fig. 4.16. (a) Spectra of the probe light at a pulse repetition rate of 40 GHz and (b) results of the logic gates.

4.7 Summary

The spectra of output pulse and probe light give information about physical effects occurring in the SOA. The knowledge of the refractive index dynamics in the SOA and of the spectral components of the pump and probe light, allows a filter-supported all-optical wavelength conversion also for other applications like logic gates.

As will be seen in chapter 6, the spectra also provide information on phase patterning effects due to slow carrier recovery.

5 All-optical wavelength conversion and regeneration based on SOAs

5.1 Introduction

The transmission at highest data rates in optical communication networks requires high-speed processing of optical data pulses at various wavelengths. All-optical wavelength converters (AOWCs) are promising candidates for this task as they transfer optical information from one wavelength to another without a conversion to the electrical domain.

The required properties of AOWCs are

- large bandwidth for high bit rate transmission,
- no extinction ratio degradation of the signal,
- good optical signal-to-noise ratio (OSNR) of the output signal,
- moderate input power levels of the signal and the new wavelength,
- wide wavelength range for input and output signals,
- low chirp of the output signal, and
- insensitivity to the polarization of the input signal.

A possible implementation of AOWCs are SOAs, which directly impress the information from a data signal on a probe light. Due to the SOA nonlinearities, the probe light gets modulated in amplitude and phase.

The exploited SOA nonlinearities concern

- gain (cross gain modulation (XGM)),
- phase (cross phase modulation (XPM)),
- both gain and phase (XGM+XPM), and
- polarization (cross polarization modulation; XPolM) by induced birefringence.

The saturation power level $P_{\mathrm{sat}}^{\mathrm{in}}$ represents the maximum input power for the operation in the small-signal regime of the SOA. With input powers P_{D} up to $P_{\mathrm{sat}}^{\mathrm{in}}$, i.e., $P_{\mathrm{D}} < P_{\mathrm{sat}}^{\mathrm{in}}$, the signal has negligible influence on the gain coefficient, and the amplifier works as a linear amplifier. An operation in the large signal regime of the SOA, $P_{\mathrm{D}} \geq P_{\mathrm{sat}}^{\mathrm{in}}$, is achieved with input powers P_{D} above the threshold $P_{\mathrm{sat}}^{\mathrm{in}}$.

The semiconductor devices show bandwidth limitations due to an incomplete refilling of the band by carrier recovery. Long signal sequences of mark bits as well as an insufficient number of subsequent space bits avoid a full carrier recovery. The incomplete band refilling acts as a memory effect for the carrier density inside the SOA, influencing the pump pulse amplification and the wavelength conversion results. The memory effect, expressed as a patterning effect, is the main drawback because it limits the signal quality and operation speed. To counteract these limitations, several solutions will be discussed in this chapter.

For specifying the pattern dependency of the output signal quantitatively, a quotient $P_{\mathrm{d}} = P_{\min} / P_{\max}$ can be defined where $P_{\min}$ ($P_{\max}$) are the minimum (maximum) powers in a pulse sequence of a pseudo-random bit sequence (PRBS). Having no pattern dependency results in $P_{\mathrm{d}} = 1$.

The output signal quality is quantified using the Q^2-factor defined in dB as

$$\left(Q^2\right)_{\mathrm{dB}} = 10\log_{10}\left(\frac{u_1 - u_0}{\sigma_1 + \sigma_0}\right)^2, \tag{5.1}$$

where u_1 and u_0 are the mean optical power for marks and spaces, and σ_1 and σ_0 the standard deviation of the noise for the respective optical power levels. The extinction ratio is the ratio between peak pulse power and the maximum power of the background between pulses.

A further benefit of semiconductor optical amplifiers is the possible use of the devices in signal regeneration [80] schemes. Signal regeneration is essential for ultra long-haul transmission since a signal distortion accumulates with the transmission distance and with the number of signal processing steps.

The different degenerative effects and their impact on the signal are listed in Table 5.1.

Table 5.1. Degenerative effects and their impact on the signal

Degenerative effect	Impact on the signal
Attenuation on the fiber	Weaker pulses
Chromatic dispersion	Broader pulses
Noise from erbium-doped fiber amplifiers	Decrease of the signal-to-noise ratio
Filtering effects	Extinction ratio decrease
Polarization mode dispersion (PMD)	Broader pulses
Nonlinear effects	Signal outside of the channel of interest

Regeneration types can be categorized with respect to their ability to improve the signal. In Fig. 5.1, the three types of regeneration are depicted schematically.

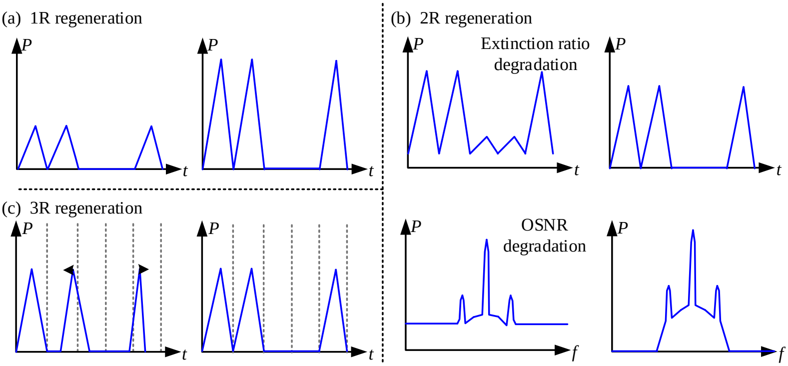

Fig. 5.1. Schematic representation of the regeneration types 1R, 2R and 3R.

The simplest type of regenerator compensates only for the amplitude loss of signals, i.e., it reamplifies (1R regenerator) the signals. An example of an 1R regenerator is the erbium-doped fiber amplifier (EDFA).

Signals with reduced extinction ratio or with low optical signal-to-noise ratio can be improved by reamplification and reshaping (2R regenerator) of the signal. 2R regenerators without wavelength conversion, e.g. the Mamyshev

2R regenerator [81], are based on the self-phase modulation (SPM) of the data signal in a nonlinear medium with subsequent optical filtering. Fluctuations in the peak power of input pulses lead in the nonlinear medium to fluctuations of the spectral shift and of the spectral broadening of the pulses in the output signal. By subsequent optical filtering the amplitudes of the pulses get equalized. An SOA-based 2R regenerator [82] impresses a data signal on a CW probe light by XPM. The phase modulated probe light signal is subsequently converted back to an amplitude modulated signal by a delay interferometer and improved in extinction ratio by passing an optical bandpass filter.

The ideal transfer function of a 2R regenerator is shown in Fig. 5.2.

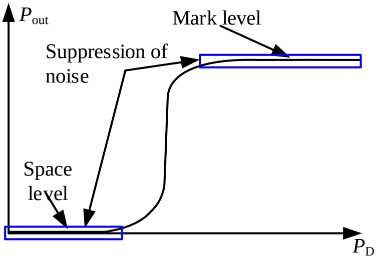

Fig. 5.2. The nonlinear transfer function for ideal 2R and 3R regeneration.

The task of a 2R regenerator is reducing the impact of noise during spaces while leveling the marks of a signal. An improvement of the bit error probability (BER) can never be realized, since existing errors cannot be corrected.

3R regenerators perform reamplification, reshaping and retiming of a signal and are employed to reduce the effect of timing jitter in signals [80, 83]. For a 3R regeneration based on SOAs, a clock signal is employed as probe light in the aforementioned 2R regenerator.

All-optical regeneration schemes with SOAs are based on the use of their nonlinearities, see Fig. 5.3.

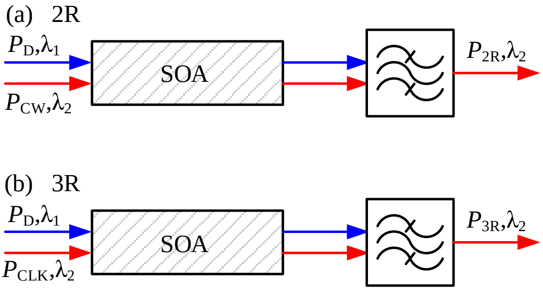

Fig. 5.3. Schematic representation of (a) a 2R and (b) a 3R regenerative wavelength converter consisting of an SOA and a filter.

In SOA based all-optical regenerators the signal regeneration is accompanied by a wavelength conversion [80, 83].

5.2 Patterning effect

The bandwidth limitation in all-optical signal processing based on SOAs is attributed to the patterning effect in the output pulse sequence, namely the decay of amplitudes for subsequent mark bits. Patterning-free operation requires a full recovery of the carriers between subsequent pulses, i.e., the delay between two consecutive pulses has to be larger than the carrier recovery time of the SOA.

Fig. 5.4 shows in an overview the changes in the SOA properties, if the carrier density does not recover between consecutive pulses in a pump probe experiment. The input bit pattern 0111 (Fig. 5.4(a)) enters the SOA. Fig. 5.4(b) shows carrier density depending on the BF interband effects, i.e., carrier depletion and carrier recovery. As depicted, the carrier density decreases with each pulse, and it recovers incompletely during its absence. Accordingly, the carrier density modulation ($\Delta N_1 > \Delta N_2 > \Delta N_3$ in Fig. 5.4(b)) diminishes. As a consequence, all material characteristics depending on the carrier density N, i.e., the SOA gain G, the change of refractive index Δn_{BF}, and the polarization-rotation are influenced. The gain decrease gets smaller with every mark in the series, see Fig. 5.4(c). This effect can also be seen in the dynamics of the refractive index Δn_{BF} for the band filling process (Fig. 5.4(d)) and also in the phase shift $\Delta\varphi_{\mathrm{CW}}$ (Fig. 5.4(e)) of the probe light [75].

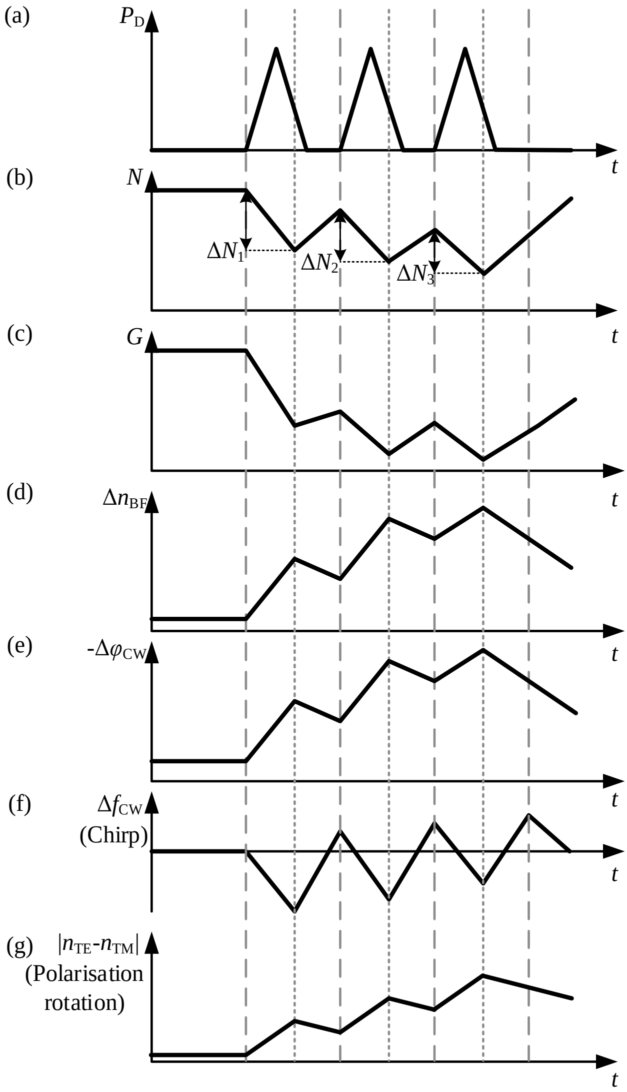

Fig. 5.4. Schematic description of (a) the input bit pattern 0111, (b) the evolution of the carrier density, (c) the gain, (d) the refractive index change, (e) the phase shift, (f) the chirp of the probe light, and (g) the induced birefringence.

The instantaneous frequency shift Δf_{CW} is proportional to the gain modulation

$$\Delta f_{\mathrm{CW}} = \frac{\alpha_{\mathrm{BF}}}{2} \frac{\mathrm{d}\left(\ln G\right)}{\mathrm{d}t} . \tag{5.2}$$

With a decreasing carrier density modulation in a sequence of marks the induced red chirp becomes smaller. The blue chirp does not change considerably due to an approximately constant carrier recovery rate.

The average carrier density N decreases with increasing bit order in the pattern and leads thus to a red-shift of all spectral components of the probe light. Consequently, in a mark sequence the absolute value of the red chirp gets larger, while the blue chirp becomes smaller.

The value of the red shift depends on the relation between P_{in} and P_{CW}, see Fig. 4.11 and Fig. 4.12. For $P_{\mathrm{CW}} > P_{\mathrm{in}}$ the red-shift becomes smaller (see Fig. 4.12) and can be neglected.

As the refractive index change is not the same for all polarizations, birefringence changes, leading to a polarization-rotation of the outcoming field (Fig. 5.4(g)). Therefore, stronger output pulses from the SOA are more polarization-rotated than weaker ones [45].

Since the ultrafast effect TPA is independent from carrier density fluctuations, its effect in SOAs [73] is also patterning independent.

A lot of concepts for pattern effect mitigation at highest bit rates have been proposed. In Section 5.3 a discussion about the performance limits of each method will be given.

5.3 All-optical wavelength conversion and regeneration

5.3.1 All-optical wavelength conversion and regeneration based on cross-gain modulation (XGM)

An intensity modulated optical data signal launched into an SOA modulates the saturated gain and subsequently the probe signal power at the output wavelength. The resulting probe signal is inverted with respect to the input signal, see Fig. 5.5. By operating long SOAs at a high current and at a bit rate of only 10 Gbit/s, a good performance for the inverted converted signal was achieved [84].

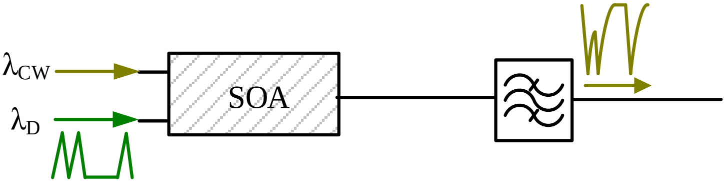

Fig. 5.5. AOWC based on Cross-Gain Modulation (XGM). The optical filter suppresses the data signal.

A technique for improving the signal quality is the use of an additional holding beam (either CW or clock) in the SOA [85]. Patterning effects are not eliminated, but their limiting effect on the modulation bandwidth is reduced.

A holding beam at the transparency wavelength limits the variation of the gain and probe phase by reducing the carrier density fluctuations. During a long series of spaces in the data signal, the carrier density inside of the SOA increases. The gain spectrum $g_{\mathrm{BF}}(\lambda)$ extends towards smaller wavelengths, and the holding beam wavelength is found in the extended gain domain. In this case the stimulated emission produced by the holding beam reduces the gain. During a long series of marks in the data signal, the carrier density decreases successively, the transparency point shifts towards longer wavelengths, and the holding beam becomes an optical pump due to its position in the absorption region. Patterning effect mitigation for signal data rates up to 40 Gbit/s has been successfully achieved [29] using a holding beam near the SOA transparency point.

Another technique to increase the response of SOAs, consists of two cascaded SOAs with a filter in-between to discard the data wavelength. Only the converted inverted signal after a first SOA, SOA$_1$, is launched into a second SOA, SOA$_2$. As long as the converted signal amplitude after SOA$_1$ is low, the gain of SOA$_2$ increases. In contrast, the gain reduces while the converted signal amplitude is large. This way SOA$_2$ improves the rising signal slope which is affected by the slow recovery of the first SOA. Error-free wavelength conversion at 170 Gbit/s has been demonstrated with this “turbo-switch” scheme [86].

A cross gain compression technique [87] for AOWC and 2R regeneration, based on cross saturation effects, has been demonstrated for bit rates up to 40 Gbit/s. Two complementary signals, i.e., an input signal and its inverted copy at another wavelength, propagate simultaneously in a highly saturated SOA sharing the same gain compression effects. The saturated gain acts as power equalizer on the marks and as gain compressor on the spaces of the output signal, improving thus the signal-to-noise ratio.

5.3.2 All-optical wavelength conversion and regeneration based on cross-phase modulation (XPM)

When performing a pump-probe experiment in the small-signal regime of an SOA, the gain remains constant while the refractive index changes. The data signal impresses the bit information on the phase of the probe signal by XPM. The phase modulation of the probe light is converted into amplitude modulation using an interferometric device, see Fig. 5.6. By splitting the input signal in two copies and delaying one copy versus the other by a delay time τ_d (corresponding to the difference in optical path) and by fine adjusting the phase of one arm towards the other by a phase shifter Φ, the signals on both arms get a phase difference of $\Delta\varphi_\mathrm{CW}$. By combining both signals, the interference leads to an amplitude modulated signal.

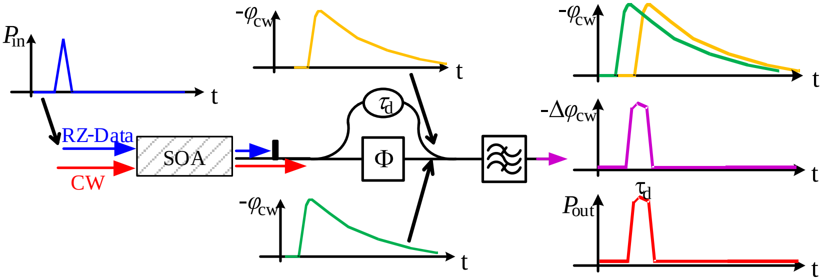

Fig. 5.6. Schematic AOWC with DI, phase evolution, switching window τ_d, phase shifter Φ and converted pulse. The optical filter blocks the input signal.

The interferometer introduces a temporal window between the phase modulated beams, allowing to switch a pulse. This switching time window is effectively shorter than the recovery time of the SOA. To ensure a good destructive interference, the phase difference during the pulse absence has to be as close as possible to π. The signal quality increases with increasing

CW power P_{CW} [51] and a bandpass filter (BPF) following the DI additionally reduces the noise.

Operating of the SOA in the small-signal regime makes a patterning-free AOWC possible, even though the carrier recovery remains incomplete within the time interval between pulses. This effect is known as linear patterning [88]. The phase difference $\Delta\varphi_{\mathrm{CW}}$ in the signal is constant for marks (Fig. 5.7).

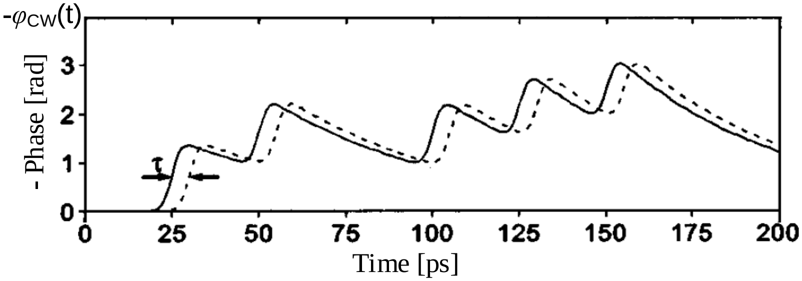

Fig. 5.7. *Temporal evolution of the probe light phase $\varphi_{\mathrm{CW}}(t)$ in the case of linear patterning [88].*

The delayed interference signal converter (DISC) has been used for wavelength conversion at bit rates of up to 168 Gbit/s [89] with only a minor signal degradation.

An AOWC at 40 Gbit/s with 2R regenerative properties and simultaneous format conversion was realized [78] using a bulk SOA and two consecutive delay interferometers, see Fig. 5.8. This experiment will in-depth be described in chapter 6.

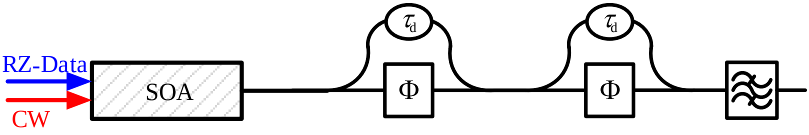

Fig. 5.8. *Schematic all-optical wavelength converter with regenerative properties.*

A 3R regenerator at 40 Gbit/s is realized using a 40 GHz optical clock instead of a CW signal in a scheme shown in [90] using a delay interferometer and a band pass filter. The clock pulse duration is set to be smaller than the length of the switching window.

Based on the same technique [91] a high speed 160 Gbit/s all-optical regenerator with retiming and reshaping potential has been reported.

An interferometer where signals travel in counter-propagating directions is called a Sagnac loop mirror. By placing a nonlinear medium like an SOA inside this loop a wavelength converter scheme can be realized. The SOA is offset from the loop center by a small distance which corresponds to a time delay Δt. As two CW light beams at the wavelength λ_{CW} and a data signal at the wavelength λ_{D} enter the SOA simultaneously, the data signal modulates the gain and refractive index of the SOA which in turn influences the amplitude and phase of both CW light beams. The co- and counter-propagating beams pass the SOA and travel different distances until they are combined. The propagation path difference corresponds to a time difference of $2\Delta t$. This time delay $\tau_{\mathrm{d}} = 2\Delta t$ represents the switching window for optical signals. The converted signal at λ_{CW} is optimal if the phase difference of the interfering beams in the absence of the data signal is π.

Such a conversion method has been demonstrated at 10 Gbit/s for non-return-to-zero (NRZ) [92] and return-to-zero (RZ) [93] modulated data formats. The amplitude and phase modulation experienced by the two counter-propagating beams must be identical. This can be only realized using a short SOA (0.5 mm to 0.6 mm) and for long pulses, i.e., low bit rates. Having pulses of long duration, slow interband effects dominate the nonlinearities in the SOA, leading to smooth amplitude and phase dynamics [94] for both beams.

Other AOWC methods are based on the nonlinear polarization-rotation. By injecting a strong data signal with a polarization of 45 degrees with respect to the SOA layers and a CW light, into an SOA, two perpendicular signals at λ_{CW} are generated due to the induced birefringence ($n_{\mathrm{TE}} \neq n_{\mathrm{TM}}$). The birefringence is also responsible for shifting the signals in time towards each other. By placing a polarization beam splitter after the SOA and aligning the CW correctly, one can combine the beams. This scheme has the same functionality as the delay interferometer. Since the polarization-rotation increases with gain saturation, a high degree of saturation is needed to achieve the necessary birefringence. Stronger pulses are therefore more rotated in polarization than weak ones. Using a polarimetric filter [95] a patterning-free wavelength conversion has been demonstrated for bit rates up to 10 Gbit/s.

5.3.3 SOA-based wavelength conversion using optical filtering

A converted signal obtained by cross-gain and cross-phase modulation (XGM+XPM) in the large signal regime is chirped. The spectra of such signals have two sidebands whose origin is described in chapter 4.

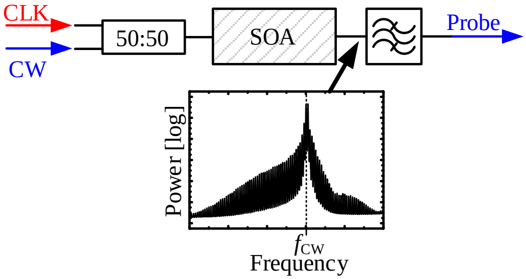

Fig. 5.9. Wavelength conversion scheme and optical spectrum of the converted clock signal (CLK) before the filter.

An input signal modulates the gain and the refractive index of the SOA. The probe beam senses both, gain and refractive index change. The converted signal at λ_{CW} is inverted, but at higher or lower wavelengths, the polarity is preserved [96]. The time development of the probe light frequency, i.e. the chirp, is illustrated in Fig. 5.10.

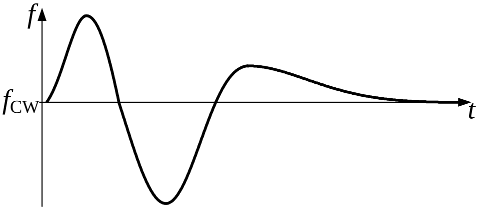

Fig. 5.10. Schematic representation of frequency chirp of the output probe light.

Optical filtering of the chirped output probe light can be used to get a converted non-inverted signal. The filter after the SOA has to perform two tasks, the re-inversion of the converted signal and the mitigation of the patterning effect of the signal.

The scheme shown in Fig. 5.9 can be generalized such that the SOA is followed by a single optical filter or by cascading different filter types. With $P_{CW} > P_D$ and with the CW probe light after the SOA being sufficiently suppressed, the converted signal is non-inverted. The SOA is employed for a wavelength conversion while keeping or simultaneously changing the modulation format. Our results concerning all-optical wavelength and modulation format conversion are presented in chapter 6.

AOWC based on SOA and a blue-shifted optical filter (BSOF)

An error-free wavelength conversion at a bit rate of 100 Gbit/s using a long SOA and a fiber Bragg filter has been demonstrated in [97]. A polarity preserving all-optical wavelength conversion at 40 Gbit/s has been realized by using a blue-shifted filter and a CW probe light with a power higher than the signal power ($P_{\mathrm{CW}} > P_{\mathrm{D}}$) [72]. SOA-based AOWC assisted by narrow blue-shifted optical filters at 40 Gbit/s [98], 80 Gbit/s [99, 100], 160 Gbit/s [101] and 320 Gbit/s [73] have been reported. The conversion schemes mentioned in these works are based on selecting a blue spectral component from the probe light spectrum (Fig. 5.11).

In accordance with our results (chapter 4), the weak ultrafast blue-shifted spectral component is due to TPA and $\mathrm{FCA}_{\mathrm{TPA}}$. Its intensity is independent on the carrier density and therefore the signal is not patterning affected. However, the signal is very weak, limiting the applicability of this method.

The blue-shifted (BS) spectral component corresponding to the carrier recovery, is one of the two beams used in the AOWC by means of a pulse reformatting optical filter (PROF) [74].

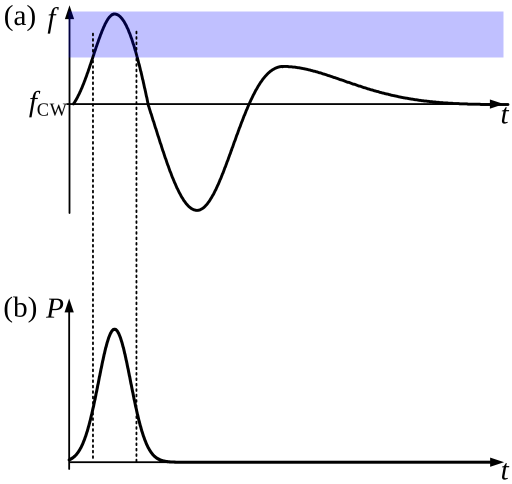

Fig. 5.11. (a) Schematic representation of the blue-shifted ultrafast spectral component filtered by a BSOF and (b) the temporal evolution of the output pulse after the filter.

AOWC based on an SOA and a red-shifted optical filter (RSOF)

The red-shifted (RS) spectral component can be separated with a RSOF [71] from the probe light spectrum. The converted non-inverted signal has a narrow spectral width (Fig. 5.12) and suffers a small dispersion in single mode fibers. This has been demonstrated in a transmission experiment of 16,800 km at a bit rate of 40 Gbit/s. We employed the RSOF for wavelength and modulation format conversion, see 6.

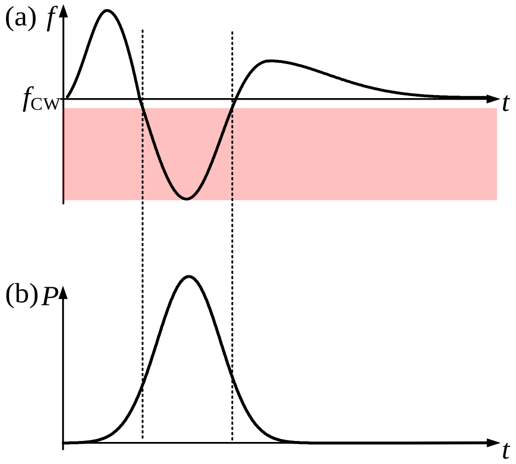

Fig. 5.12. (a) Schematic representation of the red-shifted spectral component filtered by an RSOF and (b) the temporal evolution of the output pulse after the filter.

AOWC based on an SOA and a pulse reformatting optical filter (PROF)

The separation of the red- and blue-shifted signal components as well as their combination has been realized within a filter structure named pulse reformatting optical filter (PROF) [74].

A technique for mitigating the patterning effect has been proposed in [75]:

> ***Pattern effect removal technique for semiconductor-optical-amplifier-based wavelength conversion,***
>
> J. Wang, A. Marculescu, J. Li, P. Vorreau, S. Tzadok, S. Ben-Ezra, S. Tsadka, W. Freude and J. Leuthold
> IEEE Photonics Technology Letters **19**, 1955-1957 (2007)

The method is based on optical filtering of the converted RZ signal after the SOA. The filter suppresses the central frequency of the converted inverted signal at λ_{CW} while passing red- and blue-shifted spectral components with complementary pattern effects. The superposition of the spectral components leads to an RZ signal of improved quality.

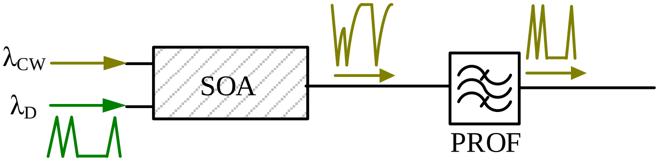

Fig. 5.13. Scheme of an all-optical wavelength conversion with a PROF.

By taking $P_{\mathrm{CW}} > P_{\mathrm{D}}$ and by suppressing the carrier at λ_{CW}, the converted signal will become non-inverted. Using a PROF, the data of an RZ signal are transferred towards another wavelength while keeping the shape of the pulse, Fig. 5.13. The input signal is split equally in two branches, one leading to a BSOF and the other one to a RSOF followed by an optical delay line (ODL) and a variable optical attenuator (VOA), see Fig. 5.14.

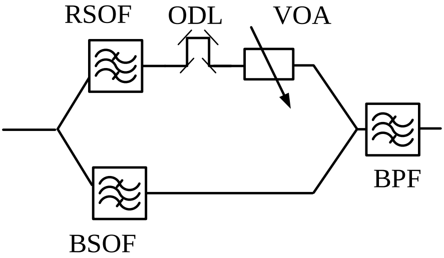

Fig. 5.14. Setup of the PROF. It consists of a RSOF, a BSOF, an optical delay line (ODL), a variable attenuator (VOA) and a bandpass filter (BPF).

The RS spectral component develops during the carrier depletion, the BS spectral component occurs later during the process of carrier recovery, see Fig. 5.10. As formations of these two signals occurs at different times and with differently resulting power levels, the superposition of the red- and blue-shifted signal components requires to have both equalized in amplitude and aligned such as to have no temporal delay towards each other. In our experiment the red-shifted component has been attenuated by 5 dB and delayed by 10 ps with respect to the blue-shifted spectral component. The PROF is followed by a band pass filter which helps suppressing the data signal after the SOA.

A 33% RZ input data signal is encoded with a PRBS of $2^7 - 1$ at a data rate of 42.7 Gbit/s was employed in the PROF experiment. The optimum operation point was found to be at the data wavelength of $\lambda_\mathrm{D} = 1530\,\mathrm{nm}$, data power of $P_\mathrm{D} = 12.7\,\mathrm{dBm}$, CW probe wavelength of $\lambda_\mathrm{CW} = 1536.1\,\mathrm{nm}$ and CW probe power of $P_\mathrm{CW} = 14.7\,\mathrm{dBm}$. The 2.6 mm long SOA was biased at $I = 750\,\mathrm{mA}$. The degree of saturation of an SOA grows in a long series of marks. The evolution of the SOA gain and chirp of the probe light after a sequence of 4 pulses is depicted in Fig. 5.15.

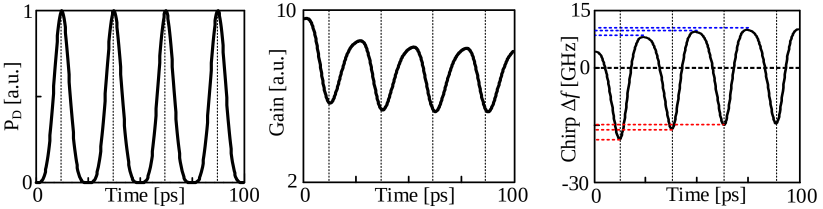

Fig. 5.15. Gain and chirp evolution depending on the mark bit order in a sequence of four RZ marks. For sake of clarity, we leave out here the temporal advance of the pulse peak compound with SOA gain dip.

By suitably exploiting the frequency-to-amplitude conversion of the RSOF and BSOF at the filter slope, both signals can develop opposite patterning effects for subsequent pulses (Fig. 5.15). The superposition of both signals results in a signal with even better quality (see Fig. 5.16).

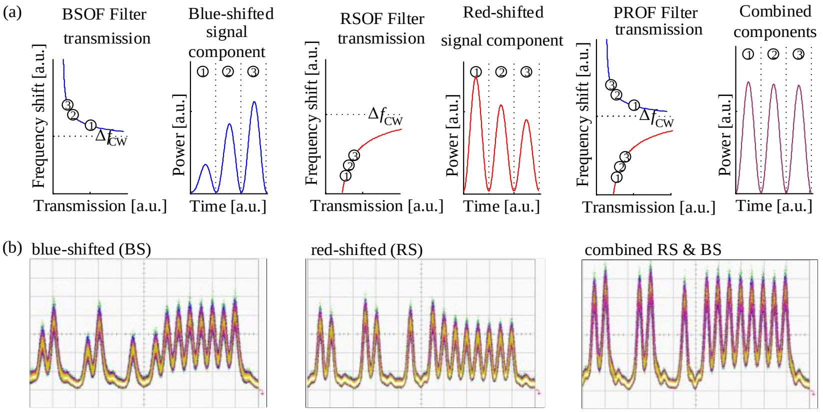

Fig. 5.16. (a) Description of BSOF and RSOF transmission, BS and RS combined signal after the PROF.
(b)The measured bit pattern of each spectral component and their combination.

The performance of the wavelength conversion with a PROF leads to a good Q^2-factor exceeding 15.6 dB for an output signal within a wavelength tolerance of $0.3\,\mathrm{nm}$ around the CW wavelength. The PROF scheme shown in Fig. 5.14, has been improved using a $1\,\mathrm{nm}$ BPF located after the PROF structure, see Fig. 5.17.

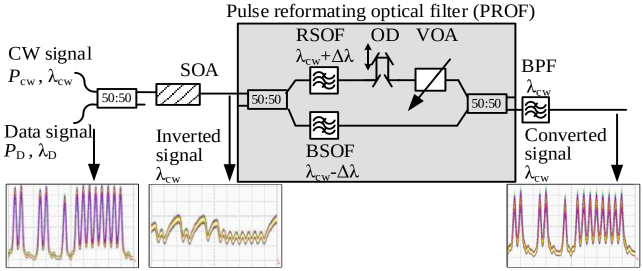

Fig. 5.17. Wavelength conversion setup consisting of an SOA, a PROF and a BPF of 1 nm.

The alignment tolerance has been determined by detuning the CW wavelength in the range of $1533.95\,\mathrm{nm}$ and $1536.4\,\mathrm{nm}$, while keeping the complete filter structure unchanged. The 1 nm wide BPF (Fig. 5.18) was chosen to equalize the amplitudes for RS and BS components.

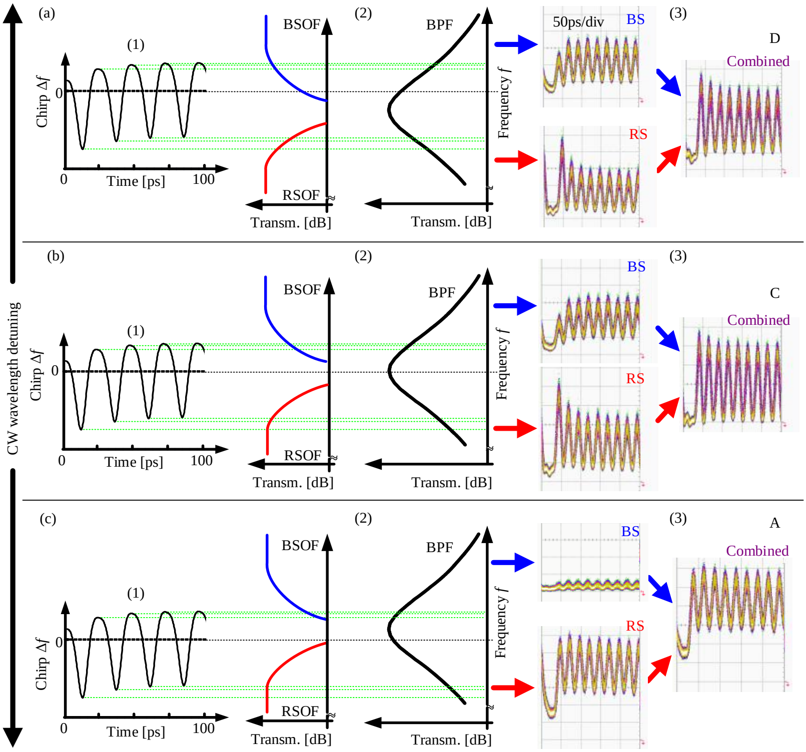

Fig. 5.18. (1) Schematic description of the induced frequency chirp in the wavelength converted inverted signal, (2) transmission spectra of RSOF, BSOF and BPF and (3) the measured bit pattern of RS and BS components and their combination for (a) $\lambda_{\mathrm{CW}} = 1536.0\,\mathrm{nm}$, *(b)* $\lambda_{\mathrm{CW}} = 1535.1\,\mathrm{nm}$ *and (c)* $\lambda_{\mathrm{CW}} = 1536.3\,\mathrm{nm}$.

At the optimum wavelength the mean power of both spectral components is the same. By shifting the CW from this position, the amplitude equalization is disturbed. If the CW is shifted towards longer wavelengths, the contribution of the red-shifted component gets stronger and the blue-shifted component gets simultaneously more attenuated. For $\lambda_{\mathrm{CW}} = 1536.3\,\mathrm{nm}$, the BS component does no longer play any role as its intensity becomes negligible. Fig. 5.18(c) shows a very small contribution of the BS component, while the RS component is patterning-free due to the combined slope of RSOF and BPF.

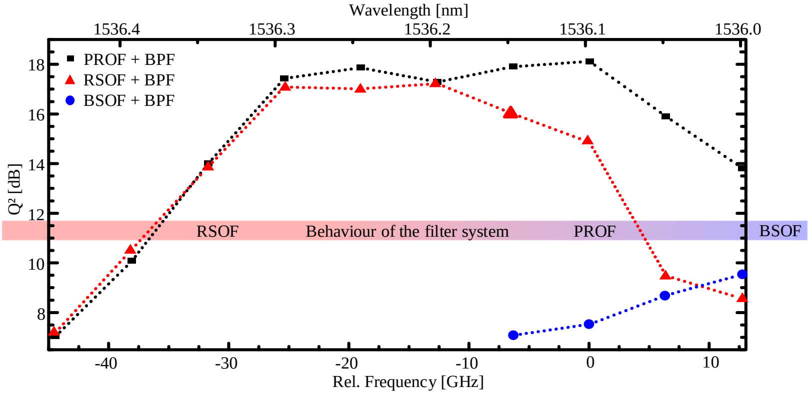

Fig. 5.19. Quality factors of converted signals at different wavelengths of RS (▲,RSOF+BPF), BS (●,BSOF+BPF) spectral component and for the combined signal (■,PROF+BPF). CW and input signal powers into the SOA are $P_{\mathrm{CW}} = 14.7\,\mathrm{dBm}$, $P_{\mathrm{D}} = 12.8\,\mathrm{dBm}$.

We can distinguish two regions in the spectral domain. A converted signal of good quality can be achieved by either employing the superposition of the RS and BS components within the region of $1536.0\,\mathrm{nm}$ to $1536.2\,\mathrm{nm}$, or by employing only the RS component in the region up to $1536.2\,\mathrm{nm}$.

At the wavelength $\lambda_{\mathrm{CW}} = 1536.3\,\mathrm{nm}$ the PROF filter structure operates in the RSOF-only regime. A simplified scheme of the converter is shown in Fig. 5.20.

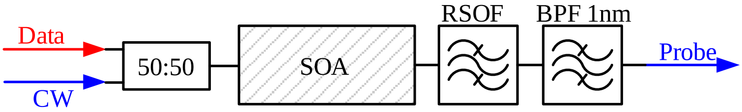

Fig. 5.20. Scheme of an all-optical wavelength converter utilizing a RSOF and BPF at $\lambda_{\mathrm{CW}} = 1536.3\,\mathrm{nm}, \lambda_{\mathrm{D}} = 1530.0\,\mathrm{nm}$.

The patterning effect mitigation in this filtering scheme is based on the dynamics of the red chirp as shown in Fig. 5.21. For the first mark in the pulse train, a large gain reduction gives a strong converted pulse and a large red chirp. For subsequent marks, the chirp and the intensities of the converted pulses are smaller. The transmission spectrum of the RSOF allows to suppress the spectral domain near the CW carrier in order to obtain a non-inverted pulse and to equalize the power of all marks in the signal.

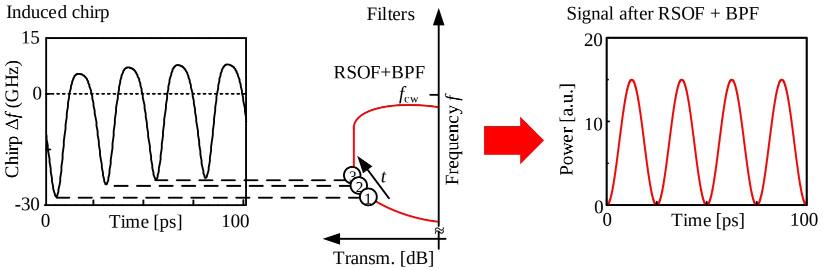

Fig. 5.21. Visualization of patterning mitigation technique of the AOWC signal utilizing the RSOF and BPF.

End of paper [75].

AOWC and 2R regeneration based on an SOA and two cascaded delay interferometers

This topic was addressed in [78]:

RZ to CSRZ format and wavelength conversion with regenerative properties

A. Marculescu, S. Sygletos, J. Li, D. Karki, D. Hillerkuss, S. Ben-Ezra,
S. Tsadka, W. Freude and J. Leuthold
Optical Fiber Communication Conference, OSA Technical Digest
Series (Optical Society of America, 2009), OThS1

By cascading two delay interferometers (DIs) of 8 ps delay each, and a band pass filter (BPF) of 3 nm bandwidth, another filtering scheme for a wavelength converter is realized.

The role of each filter component is shown in Fig. 5.22(b). The first delay interferometer (green curve) suppresses the CW carrier and re-inverts the signal. A part of the blue spectral component close to the CW corresponds to the slow recovery process that would lead to a patterning effect. This spectral domain gets also suppressed.

A second delay interferometer (blue curve) attenuates the red-shifted spectral component and mitigates the patterning effect by frequency-amplitude conversion on the filter slope.

In this experiment, the bulk SOA of 2.6 mm length was biased at a current of 1 A. The power levels for data and CW signals are $P_D = -6\ \mathrm{dBm}$ and $P_{CW} = 0\ \mathrm{dBm}$.

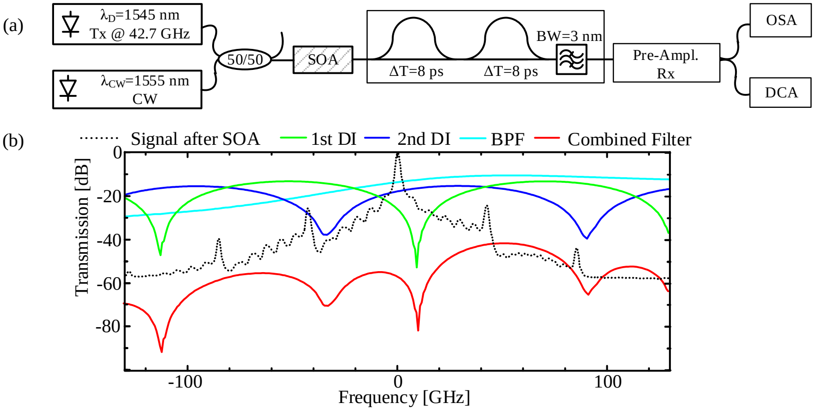

Fig. 5.22. (a) Scheme of AOWC, (b) Transmission functions for each component within the filter scheme and the spectrum of the signal after the SOA. The carrier frequency is taken as reference.

The output signal is converted, non-inverted and its quality is improved with respect to the input signal, i.e., the SOA and the filter system work as a AOWC with 2R regenerative properties. The signal quality improvement as well as a schematically depicted nonlinear transfer function $P^{out} = f\left(P_{in}\right)$ is depicted in Fig. 5.23.

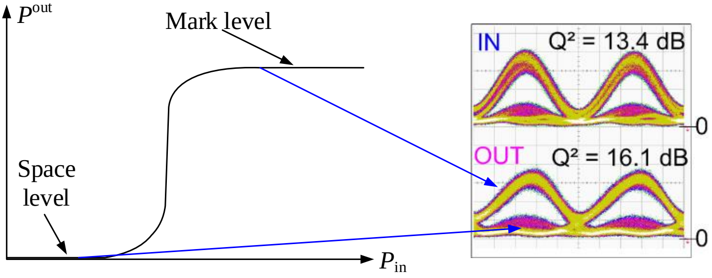

Fig. 5.23. Nonlinear transfer function of a 2R regenerator. The eye diagrams depict the improvement of the output signal quality.

It is known [83] that delay interferometers provide an S-shaped ($\sin^2$) transfer function. The length of each pulse in the signal is determined by the length of the delay within the DI. The bandpass-filter of 3 nm bandwidth suppresses the data signal and improves the extinction ratio.

A Q^2-factor improvement of more than 2 dB has been measured, see Fig. 5.24.

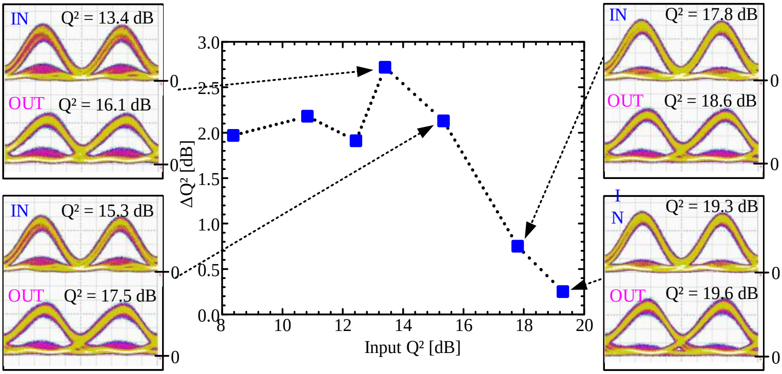

Fig. 5.24. Measurement of Q^2-factor improvement for extinction ratio degraded signals as results from eye diagrams, shown in the inset pictures.

Besides wavelength conversion and regeneration, this setup also performs a format conversion, see 6.

5.4 Summary

SOA-based wavelength conversion at high bit rates can be realized by utilizing two different methods to avoid patterning effects in the signal.

One method is to exploit the ultrafast refractive index decrease due to FCA$_{TPA}$ where the carrier density inside the SOA does not play any role. This ultrafast effect generates a blue-shifted spectral component within the blue region. By selecting this spectral component using a narrow band pass filter, a patterning-free wavelength converted non-inverted signal is achieved. The disadvantage of this method is that the signal has only little power after being filtered.

Alternatively, it is possible to employ "artifices" to improve the output signal quality. Artifices could be: the use of a holding beam, the "turbo-switch" technique (which makes use of two SOAs) and filtering schemes based on thin film filters and differential interferometry. These methods do not eliminate the patterning effect but increase threshold of the signal bandwidth.

Optical filtering techniques have been applied in detail in this work on all-optical wavelength conversions and regeneration at bit rates of 40 Gbit/s. 2R regeneration was realized using wavelength converter with a step-like or S-like transfer function, e.g., using delay interferometers.

End of paper [78].

6 All-optical wavelength and modulation format conversion

6.1 Introduction

The electric field of an optical signal can be described by

$$\vec{E}(t) = A(t)\cos\left[\omega(t)t + \varphi(t)\right]\vec{e}(t) \tag{6.1}$$

where $A(t)$ is the amplitude, $\omega(t)$ the angular frequency, $\varphi(t)$ the phase shift and $\vec{e}(t)$ the (real) polarization unit vector.

The various modulation formats can be classified into the following four categories, depending on which of the four parameters A, ω, φ, $\vec{e}$ are modulated specifying the electrical field of the optical carrier belongs:

Parameter	Modulation format
$A(t)$	Amplitude shift keying (ASK)
$\varphi(t)$	Phase shift keying (PSK)
$\omega(t)$	Frequency shift keying (FSK)
$\vec{e}(t)$	Polarization shift keying (PolSK)

Two of the most important unipolar intensity modulated formats are NRZ and RZ. In the NRZ format, each sequence of consecutive marks or spaces, is reflected by no signal level change. In the RZ format the marks occupy only 33% or 50% of the bit slot [102].

The optical signals with RZ and NRZ modulation formats show symmetrical spectra consisting of a central carrier and usually two tones mirroring each other at the distance of the modulation frequency away from the carrier (Fig. 6.1). The sidebands between the carrier and the tones carry the whole information. Each sideband between two tones carries the same redundant information. Therefore, it is possible to slice the spectrum and to utilize only a single sideband (SSB) without losing any information.

The spectral bandwidth of the signal is decisive for the channel spacing. The unwanted frequency domains are filtered to reduce the signal bandwidth and prevent thereby the spectral crosstalk between the adjacent channels.

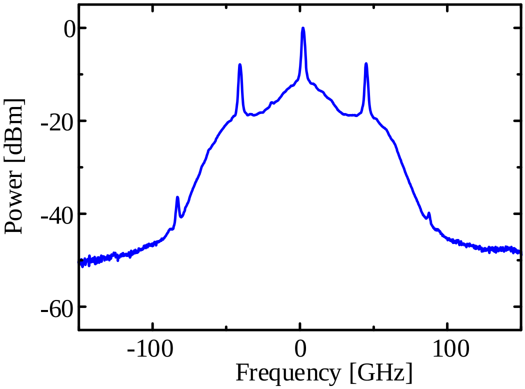

Fig. 6.1. The measured optical spectrum of an RZ signal at a bit rate of 40 Gbit/s.

In practice it is difficult to completely suppress a sideband, while not perturbing the other. The vestigial sideband (VSB) format uses only one complete sideband and the vestige of the other. The VSB format can be obtained from an RZ or NRZ signal by optical filtering. Its spectrum is asymmetric and depends on the filter shape and the wavelength detuning with respect to the carrier frequency of the initial signal [102].

VSB modulation formats have a non-vanishing progressive phase shift (PPS). In particular, a PPS of π is characteristic for a CSRZ format [78]. The CSRZ signal is an intensity-modulated RZ signal with an alternating phase of π. This bipolar format beneficially supports the transmission by reducing the influence of dispersion. Since two subsequent mark bits have alternating phases, their overlap due to pulse broadening at dispersion, leads to a destructive interference. Therefore, the inter-symbol-interference (ISI) can be minimized. A phase inversion between adjacent bits means that, on average half of the marks have a positive optical field, while the other half has a negative sign resulting in a zero mean-field envelope. As a consequence, the carrier at the optical center frequency is suppressed, giving the format its name carrier-suppressed RZ. The simplest CSRZ spectrum exhibits two tone frequencies differing by the modulation frequency [103].

Standard optoelectronic techniques are applied to obtain signals with a desired modulation format. Their optical spectra show characteristic shapes, reflecting the relationship to the autocorrelation function of the signal via Fourier transform.

6.2 All-optical format conversion

All-optical format conversion from CSRZ to NRZ at 40 Gbit/s [103] has been realized with a DI and a narrow band pass filter.

More modulation formats are obtained by detuning an optical filter with respect to the carrier frequency [76, 77, 104]. The format conversion from RZ to VSB and CSRZ was demonstrated on a Gaussian pulse and a Gaussian filter at the bit rate of 40 Gbit/s [76]. If the signal carrier frequency is the same as the filter central frequency, an RZ signal will result. By detuning the filter various VSB formats are obtained such that the phase relation between consecutive bits is proportional to the filter detuning. The PPS is 0 for an RZ modulation format, and π or $-\pi$ for a CSRZ modulation format. Other values between 0 and $\pm 2\pi$ correspond to the VSB modulation format. For practical applications $PPS = \pm \pi/2$ and $\pm 3\pi/2$ are most interesting. A unique identification of the modulation format from optical spectra is possible only for signals consisting of Fourier limited pulses. The modulation format can be determined by measuring the PPS as well as by characterizing the pulse using the FREAG technique [77, 105, 106].

6.3 All-optical wavelength and format conversion based on SOAs

The carrier density modulation in SOAs depends on the input pulse power and frequency, but not on the phase and polarization. For this reason, a wavelength and format conversion with SOAs is possible when the input data is modulated in amplitude. The probe light spectrum includes contributions of both cross-phase and amplitude modulations as can be seen in Fig. 6.2. The information carried in each sideband is influenced by SOA gain and refractive index dynamics. However, the carrier depletion is responsible for the phase modulation contributing to the red sideband, while the phase modulation contributing to the blue sideband close to the CW carrier frequency is caused by carrier recovery.

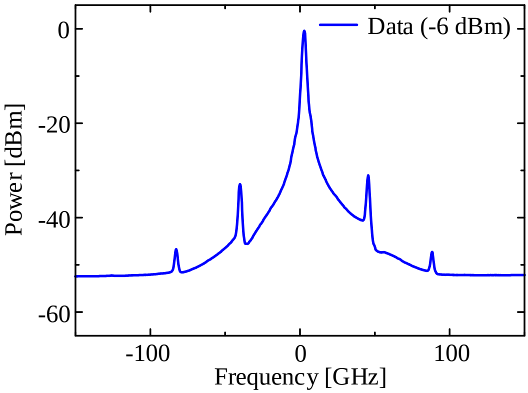

Fig. 6.2. Probe light spectra after the SOA using an 33% RZ data signal a bit rate of 40 Gbit/s.

A suitable filter after the SOA must mitigate the patterning effect, preserve the signal polarity and generate the desired modulation format.

The RZ signal has been converted into an NRZ signal at 100 Gbit/s by using an SOA and a DI with a switching window equal to the bit period [104]. Later, the conversion of an RZ into an inverted NRZ [71] signal at 40 Gbit/s has been realized.

Besides the amplitude modulation format changes, the SOA was employed in all-optical differential phase-shift keying wavelength converters [107].

6.3.1 All-optical wavelength conversion and RZ to VSB format change

The VSB-RZ signal generation behind the SOA has been demonstrated by means of a red-shifted optical filter (RSOF), see Fig. 6.3.

This topic was addressed in [77]:

All-optical vestigial-sideband signal generation and pattern effect mitigation with an SOA based red-shift optical filter wavelength converter

J. Wang, A. Marculescu, J. Li, Z. Zhang, W. Freude and J. Leuthold
34th European Conference on Optical Communication (ECOC), (IEEE, 2008), We.2C6.

VSB signals have three benefits in optical communications: short spectral domain allowing a dense wavelength division multiplex DWDM, improved tolerance to dispersion and reduced inter-symbol interference (ISI) for $PPS = \pm\pi/2$ between bits.

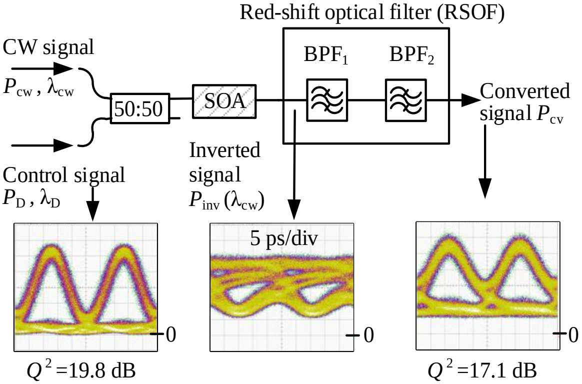

Fig. 6.3. *AOWC setup for VSB signal generation.*

The setup comprises an $2.6\,\mathrm{mm}$ long SOA, the applied bias current was $I = 750\,\mathrm{mA}$. The operation point for the data signal and CW light has been taken at $P_D = 12.7\,\mathrm{dBm}$, $\lambda_D = 1530\,\mathrm{nm}$ and $P_{CW} = 14.7\,\mathrm{dBm}$, $\lambda_{CW} = 1536.1\,\mathrm{nm}$. The conditions to obtain a converted non-inverted pulse are $P_{CW} > P_D$ and a strong suppression of the CW carrier.

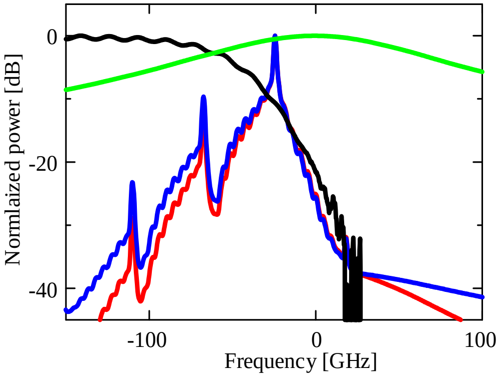

Fig. 6.4. *The filter transmission for each bandpass filter (BPF_1: black curve; BPF_2: green curve) and the measured signal spectra after the first filter BPF1 (blue curve) and after both filters BPF_1+BPF_2 (red line).*

The patterning effect mitigation is achieved by a frequency-amplitude conversion on the filter slope, see section 5.3.3. The filter and signal characteristics are shown in Fig. 6.4.

The Q²-factor is above $15.6\,\mathrm{dB}$ within an operation range of about $0.2\,\mathrm{nm}$ for λ_{CW} in the range of $1536.1\,\mathrm{nm}$ to $1536.3\,\mathrm{nm}$. If λ_{CW} lies outside this domain, the filter does not compensate the patterning effect any more.

By detuning the CW wavelength, VSB signals with different PPS are obtained. At $\lambda_{\mathrm{CW}} = 1536.3\,\mathrm{nm}$ a PPS of $-\pi/2$ has been found. The advantage of the PPS of $\pm\pi/2$ is having no ISI between the first and the third bit in a signal. The spectral bandwidth is reduced improving thereby the dispersion tolerance and spectral efficiency.

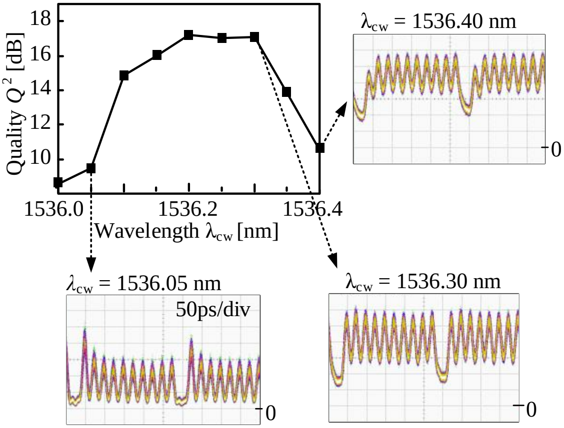

Fig. 6.5. Signal qualities for the wavelength converted signal within the wavelength range of $1536.0\,\mathrm{nm}$ *to* $1536.4\,\mathrm{nm}$.

To determine the temporal pulse profile, chirp and the phase profile of the signal, the FREAG technique was employed, which extracts both amplitude and phase from temporarily sampled spectrograms [77, 105, 106]. A progressive phase shift of $-\pi/2$ has been measured at a wavelength of $\lambda_{\mathrm{CW}} = 1536.30\,\mathrm{nm}$, see Fig. 6.6.

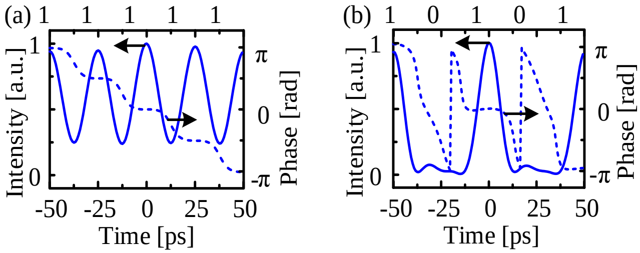

Fig. 6.6. *Measured amplitude and phase dynamics of a VSB signal with bit patterns (a) 1111 and (b) 1010 at the CW wavelength* $\lambda_{\mathrm{CW}} = 1536.30\,\mathrm{nm}$.

End of paper [77].

6.3.2 All-optical wavelength conversion and RZ to CSRZ format change

A simple scheme to perform an RZ-to-CSRZ format conversion relays on a single SOA followed by a filter.

This topic was addressed in [78]:

RZ to CSRZ format and wavelength conversion with regenerative properties

A. Marculescu, S. Sygletos, J. Li, D. Karki, D. Hillerkuss, S. Ben-Ezra, S. Tsadka, W. Freude and J. Leuthold

Optical Fiber Communication Conference, OSA Technical Digest Series (Optical Society of America, 2009), OThS1

The filter system consisting of two cascaded delay interferometers and a band pass filter (Fig. 6.7) has been described in section 5.3.3.

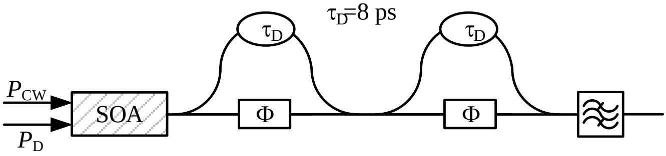

Fig. 6.7. *RZ-to-CSRZ format transformation setup.*

The filter system approximates the theoretical optimum filter with the RZ-to-CSRZ filter transfer function (Fig. 5.22).

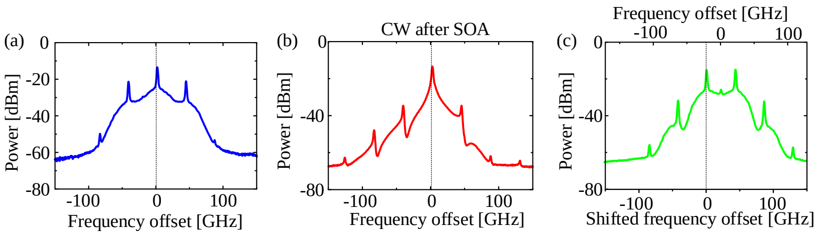

Fig. 6.8. Spectra of (a) the input RZ signal, (b) the CW signal after the SOA and (c) an ideal CSRZ signal

The DIs are adjusted to the same differential time delay $\tau_D = 8\,\mathrm{ps}$ between both arms. The generated signal is a $2^{31}-1$ PRBS encoded R $\lambda_D = 1545\,\mathrm{nm}$ Z 33% signal at a bit rate of 42.7 Gbit/s. The data signal at the wavelength of is launched together with a CW signal at the wavelength $\lambda_{CW} = 1555\,\mathrm{nm}$ into an SOA, which is biased at $I = 1\,\mathrm{A}$.

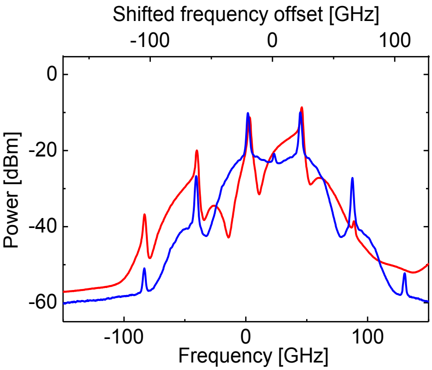

Fig. 6.9. Comparison of the probe light spectrum after the filter (red curve) with an ideal CSRZ signal (blue curve).

The power levels for the data and the CW signals are set to $P_D = -6\,\mathrm{dBm}$ and $P_{CW} = 0\,\mathrm{dBm}$, respectively. Since the carrier tone at the modulated CW signal gets suppressed, the converted pulse gets non-inverted. Both DIs and the band pass filter support the pattern effect mitigated wavelength conversion (see Section 5.3.3) and format conversion towards the CSRZ format.

The center frequency of the output pulse spectrum is shifted with about $21\,\mathrm{GHz}$ towards the blue side with respect to the carrier frequency. To verify whether the output signal shows a progressive phase shift of π between consecutive bits, the amplitude and phase characteristics of the signal have been determined using the FREAG with the two repetitive pattern sequences 1111 and 1010. The results of these measurements are depicted in Fig. 6.10.

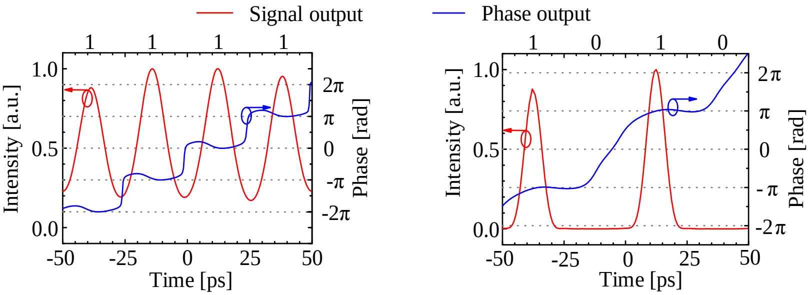

Fig. 6.10. Intensity and phase evolution of the repetitive pulse sequences 1111 and 1010.

The signal after the filter carries a PPS of π and shows a characteristic CSRZ spectrum (Fig. 6.9).

A high Q^2-factor of $20.6\,\mathrm{dB}$ has been achieved at the output of the filter for the wavelength conversion. The regenerative properties of the scheme have also been assessed and a significant improvement in terms of Q^2-factor has been demonstrated, see Section 5.3.3.

The CSRZ signal has a reduced bandwidth and the advantage of the PPS of π, i.e., there is no ISI between consecutive marks in the signal.

End of paper [78].

6.4 Evidence of phase patterning effects in the spectrum

The conversion of data signals at data rates of 40 Gbit/s does not allow a complete carrier recovery within a single bit slot. As carrier recovery between subsequent marks remains incomplete, a decreasing progressive phase shift gets induced on the output signal. The phase change reveals in characteristic features of the optical spectrum, which are a proof for a phase patterning.

We depict this observation in following section, which is transferred from Section 5 of the Optics Express paper [54]. The text has been altered with respect to variables, figures and figure positions to match the thesis.

Begin of paper [54], Section 5.

Spectral signature of nonlinear effects in semiconductor optical amplifiers

A. Marculescu, S. Ó'Dúill, C. Koos, W. Freude, and J. Leuthold
Opt. Express 25(24), (2017)

The spectra of the modulated probe light for a long sequence after the SOA alone, or followed by a filter have a characteristic shape in the region between consecutive tones. The continuous domains are less smooth than those of the standard formats; they show crevasses and shoulders, see Fig. 6.11. We will show below that they usually arise as a consequence of phase patterning.

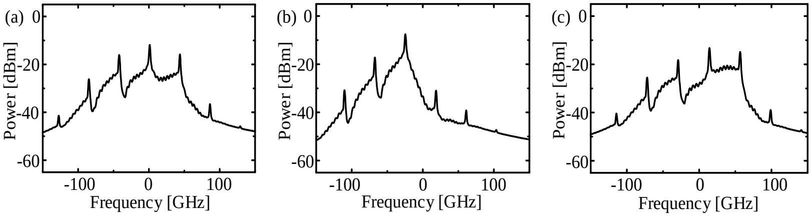

Fig. 6.11. Measured spectra after the SOA of a signal in an (a) RZ, (b) VSB and (c) CSRZ format at 40 Gbit/s modulation frequency.

We explain such a shape as a consequence of the incomplete restoration from bit to bit of the refractive index in an SOA. The power spectral density is the modulus squared of the Fourier transform of the signal carrying binary information. NRZ and RZ formats are only amplitude modulated signals, VSB and CSRZ signals are additionally phase modulated.

To demonstrate that phase patterning leads to inverted spikes and to contiguous S-shaped shoulders, we propose the following model: Every mark bit entering the SOA induces a decrease of carrier density and thus an increase of refractive index. As a consequence, the phase of each mark bit increases with a certain value $\phi_1 > 0$, while a space bit allows for a weak phase recovery $\phi_2 < \phi_1$. Each pulse entering the SOA experiences a phase accumulated from prior pulses.

Table 6.1. Total signal phase change for a bit sequence of a 110100 sequence with a filter set to generate a RZ signal and a filter offset to generate a progressive phase shifted.

Sequence	1	1	0	1	0	0
Total induced phase change	$+\phi_1$	$+2\phi_1$	$+2\phi_1-\phi_2$	$+3\phi_1-\phi_2$	$+3\phi_1-2\phi_2$	$+3\phi_1-3\phi_2$
Total signal phase with linear phase shift *PPS*	PPS $+\phi_1$	$2PPS$ $+2\phi_1$	$3PPS$ $+2\phi_1-\phi_2$	$4PPS$ $+3\phi_1-\phi_2$	$5PPS$ $+3\phi_1-2\phi_2$	$6PPS$ $+3\phi_1-3\phi_2$

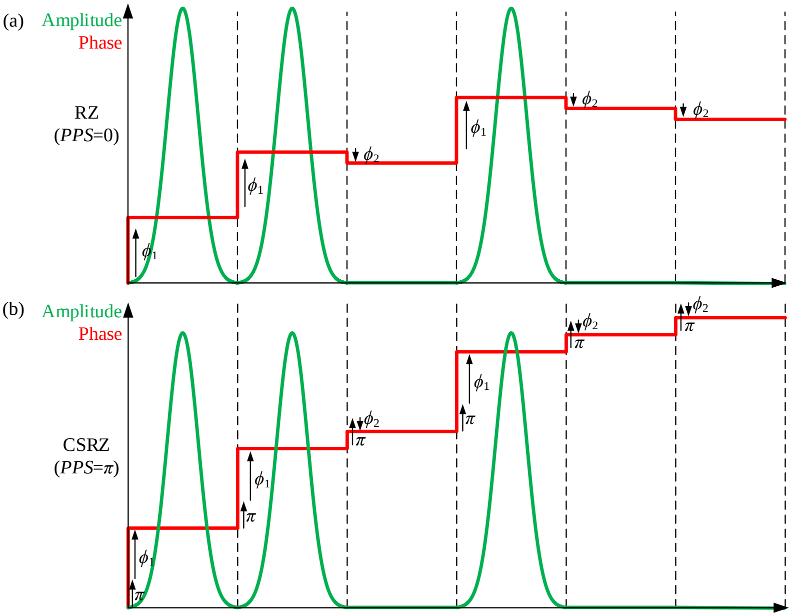

Fig. 6.12. Amplitude (green line) and phase (red line) evolution of (a) an RZ signal ($PPS = 0$) and (b) a CSRZ signal ($PPS = \pi$) after a filter supported wavelength conversion. A mark bit increases the phase by ϕ_1 and a space bit decreases the phase by ϕ_2 .

For simplicity, we assume constant phase shifts ϕ_1 and ϕ_2 . They might indeed be realized for weak signals where patterning effect might add up linearly [88]. The analysis can be extended to format and wavelength converted signals. In this case a progressive phase shift is added to the total phase.Table 6.1 shows the signal phase assignment for an exemplary bit sequence 110100. The time evolution of the amplitude and phase shift for the bit sequence is shown in Fig. 6.12 for (a) RZ and (b) a signal where the filter is offset such that a CSRZ signal is generated [78].

Fig. 6.13 shows the calculated spectra of the RZ and the CSRZ signals for $\phi_1 = \phi_2 = 0$ and for $\phi_1 = 1.875\pi$, $\phi_2 = \phi_1 / 8$.

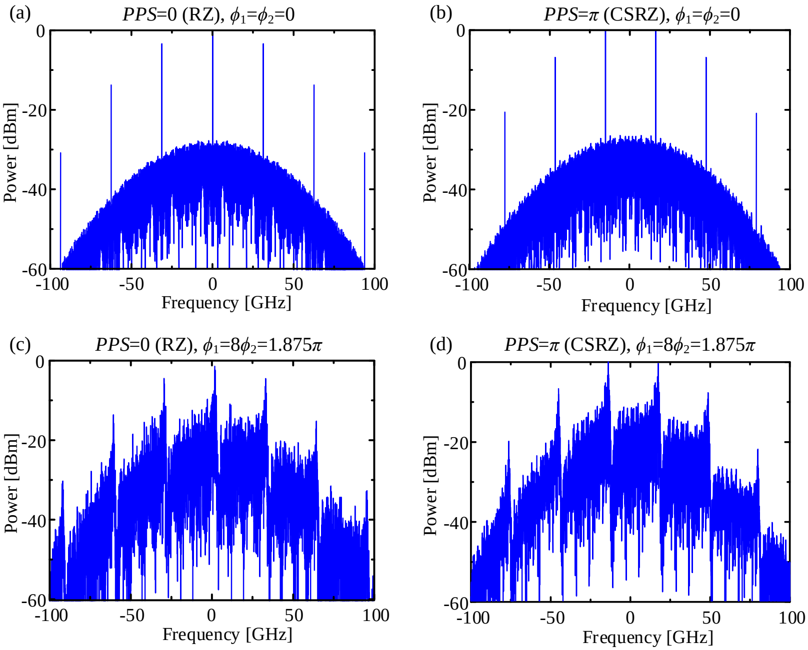

Fig. 6.13. Calculated spectra for standard (a) RZ and (b) CSRZ signals and for phase patterning affect (c) RZ and (d) CSRZ signals after wavelength conversion, respectively wavelength and format conversion.

The position of the tones does not change with ϕ_1, ϕ_2 but the spectral region in between tones shows the characteristic structure similar to the one observed in the experiment. The presence of the phase patterning effect thus leaves spectral traces in the signal spectrum.

Higher order pseudo-random bit sequences (e.g., $2^{31}-1$) will show a slightly different output spectrum due to saturation and recovery effects. Nevertheless, since longer mark-and-space sequences contribute only to the spectral components at rather low frequencies, it will be difficult to observe the difference in the output spectrum.

End of paper [54], Section 5.

6.5 Summary

By taking suitable values for the injected CW power, data powers and bias current of the SOA, it is possible to realize an all-optical wavelength conversion with simultaneous format change if the filter behind the SOA is properly chosen. Analyzing different optical spectra after the filter, one can unambiguously identify the modulation format of the output signal.

A spectral method can also provide information on whether significant patterning due to slow carrier recovery effects is present.

Appendix A
Correlation between refractive index and gain dynamics of the SOA and output pulse shape and phase

A.1 Correlation between refractive index dynamics of the SOA and output pulse shape

The power dynamics and phase dynamics of the pulse leaving an SOA have been simultaneously measured as described in chapter 3. To our knowledge, such measurements have not been repeated in literature.

The time relation between the output pulse shape and the dynamics of the refractive index of the active medium (as reflected in the change of the phase shift) is necessary for the calculation of the pulse optical spectrum.

The output pulse after the SOA has been analyzed with the two-dimensional technique utilizing the frequency resolved electro-absorption gating (FREAG) technique [106]. The time-resolved phase takes an almost constant value until about 1 ps after the pulse peak before it starts decreasing (Fig. A.1).

Thus the refractive index remains constant for a while indicating that the increase produced by depletion has to be compensated by refractive index decrease mainly due to TPA [61]. The strong decrease of the refractive index starts at 1 ps after the pulse maximum because of the delayed occurrence of the FCA_{TPA} effect.

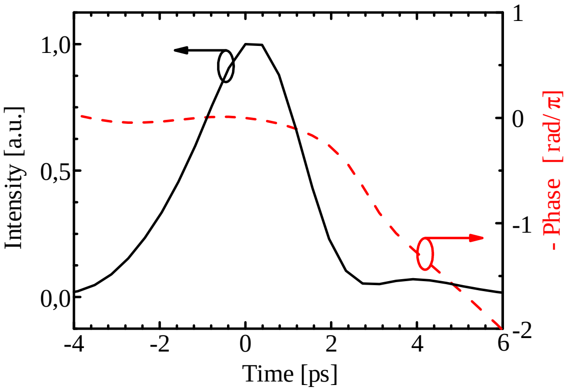

Fig. A.1. Measured pulse shape (black curve) and phase dynamics (red curve) using the FREAG

A.2 FCA$_{TPA}$ process

This section is transferred from Appendix A of the Optics Express paper [54]. The text has been altered with respect to variables, figures and figure positions to match the thesis.

Begin of paper [54], Appendix A.

Spectral signature of nonlinear effects in semiconductor optical amplifiers

A. Marculescu, S. Ó'Dúill, C. Koos, W. Freude, and J. Leuthold
Opt. Express **25**(24), 29526-29559 (2017)

The generation of a TPA-induced free carrier can occur either instantaneously (instantaneous FCA$_{TPA}$) by the absorption of a photon and a phonon, or via a two-stage process (delayed FCA$_{TPA}$), which we now describe. In the first stage, electrons are excited to the Γ-valley of the lowest conduction band (CB$_1$) at energies above the X-valley minima by the absorption of two photons. These photoexcited electrons are then scattered to the X-valley by short-wavelength phonons. The transfer to the X-valley (intervalley scattering $\Gamma \rightarrow \mathrm{X}$) is favored by the large density of states in the X-valley as compared to the Γ-valley.

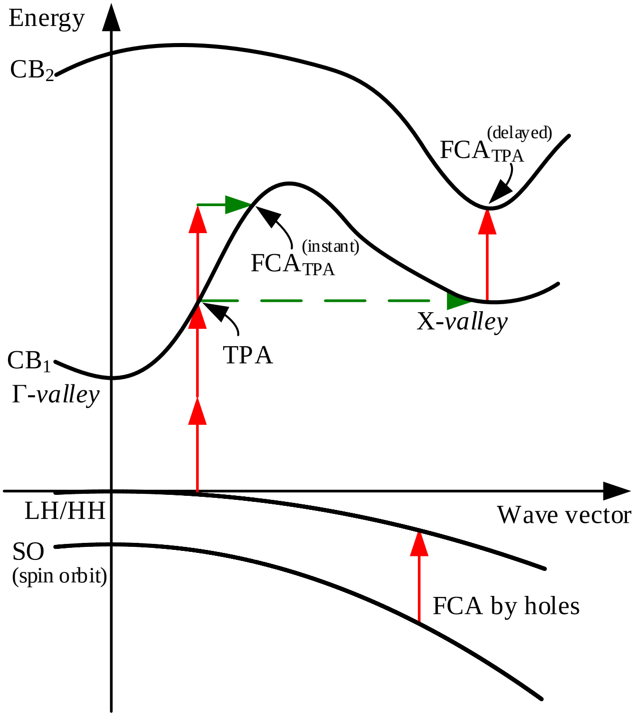

Fig. A.2. Schematic of energy band diagram with TPA, intervalley scattering, FCA induced by TPA and FCA by holes. Two photons promote an electron from the light or heavy hole (LH/HH) valence band to the Γ *- valley of the lowest conduction band (*CB_1*) at an energy above the X-valley minimum. The photoexcited electron can either remain in the* Γ *- valley by simultaneous absorption of one photon and one short wave vector phonon, or it can be first scattered by a long wave vector optical phonon into the X-valley and then be lifted to the next higher conduction band (*CB_2*) by absorbing a photon. In the FCA process by holes, an electron from spin orbit (SO) valence band absorbs a photon (without phonon assistance) and occupies a free hole in the LH/HH valence bands. The one- and two-photon absorptions are shown by red vertical arrows, the phonon absorption by a green arrow and the intervalley scattering by a green dashed arrow.*

Both steps of this two-stage process do not occur simultaneously as there is a short delay of a few picoseconds between these two processes. Due to the specific band structure of the semiconductor material, once in the X-valley, those electrons can absorb a photon, without a phonon, to reach the next higher conduction band (CB_2) [56-58]. Due to this last absorption process, the refractive index strongly decreases, leading to the observed blue sideband, see Fig. A.1.

Previous work may have encountered an FCA$_{\text{TPA}}$ process delayed by the intervalley scattering $\Gamma \to \mathrm{X}$, because the carrier density rate equation in [43] (Eq. (13)) needed a correction term for carrier leakage at high carrier energies. Let W_{X} and $W_{\mathrm{X,cl}}$ be the energy separations between X-valley of CB$_1$ and the top of the valence bands for the quaternary compound InGaAsP (see Fig. A.2) and for the cladding, respectively; $W_{\mathrm{X}} < W_{\mathrm{X,cl}}$. If by absorbing a photon of energy, the condition $W_{\mathrm{X}} + \hbar\omega_0 \geq W_{\mathrm{X,cl}}$ is fulfilled, FCA-excited electrons can drift into the cladding, accounting thus for the carrier leakage.

We have tried to describe the change in the refractive index due to FCA$_{\text{TPA}}$ by employing a minimum number of parameters, so we have neglected the FCA-coefficient $\left|\Delta g_{\mathrm{FCA}}(z,\tau)\right|$ compared to the change $\left|\Delta g_{\mathrm{BF}}(z,\tau)\right|$ in the BF gain,

$$\left|\Delta g_{\mathrm{FCA}}(z,\tau)\right| \ll \left|\Delta g_{\mathrm{BF}}(z,\tau)\right| . \tag{A.1}$$

By introducing the FCA cross-section σ_{FCA}, one can express the proportionality of $\Delta g_{\mathrm{FCA}}(z,\tau)$ to the concentration $N_{\mathrm{FCA}}(z,\tau)$ of FCA-excited electrons as

$$\Delta g_{\mathrm{FCA}}(z,\tau) = -\sigma_{\mathrm{FCA}} N_{\mathrm{FCA}}(z,\tau) . \tag{A.2}$$

A similar proportionality in terms of the concentration of depleted carriers $\left|N(z,\tau) - N_{\mathrm{st}}\right|$ is found for the change in the BF gain coefficient, see Eq. (4.23). Here $N(z,\tau)$ is the total carrier density and N_{st} its unsaturated value. By substituting Eqs. (4.23) and (A.2) in the inequality Eq. (A.1), one can obtain an upper bound for the ratio N_{FCA} to $\left|N - N_{\mathrm{st}}\right|$ (Γ is the confinement factor and a_0 the BF differential gain),

$$\frac{N_{\mathrm{FCA}}(z,\tau)}{\left|N(z,\tau) - N_{\mathrm{st}}\right|} \ll \frac{\Gamma a_0}{\sigma_{\mathrm{FCA}}} . \tag{A.3}$$

When the FCA cross-section and the BF differential gain are of the same order of magnitude, $10^{-20}\,\mathrm{m}^2$, the right-hand side of Eq. (A.3) is of order one and the number of free carriers produced by TPA cannot by far exceed the number of carriers removed by CD. As an example, let us assume for σ_{FCA} the value $10^{-20}\,\mathrm{m}^2$ calculated in [55] (Fig. 8) for GaAs at $\lambda_0 = 1.55\,\mu\mathrm{m}$. The product Γa_0 can be determined from the structural parameters of the employed SOA as well as from the data in Table 4.1, with help of the formula $\Gamma a_0 = 2\pi\hbar c A / (W_{\mathrm{sat}} \lambda_0)$. Substituting the numerical values for the area of the active region $A = 0.225\,\mu\mathrm{m}^2$, saturation energy $W_{\mathrm{sat}} = P_{\mathrm{sat}}\tau_s = 5\,\mathrm{pJ}$ and $\sigma_{\mathrm{FCA}} = 10^{-20}\,\mathrm{m}^2$ on the right-hand side of Eq. (A.3), one finds

$$\frac{N_{\mathrm{FCA}}(z,\tau)}{\left|N(z,\tau) - N_{\mathrm{st}}\right|} \ll 0.58\,. \tag{A.4}$$

Our SOA model is based upon the unique spectral component observed in the pump spectra and attributed to the FCA$_{\mathrm{TPA}}$ effect. This implies that during the pulse-SOA interaction the phase shift $\Delta\varphi_{\mathrm{FCA}}(\tau)$ associated to FCA$_{\mathrm{TPA}}$ becomes much stronger than the BF phase shift $\Delta\varphi_{\mathrm{BF}}(\tau)$. We will clarify now how such a large effect can come about with a relatively small number of FCA$_{\mathrm{TPA}}$-excited carriers, see e.g., Eq. (A.4). We introduce the α -factors α_{FCA} and α_{BF} associated to FCA$_{\mathrm{TPA}}$ and BF, respectively, and write the corresponding index-change, Δn_{FCA} and Δn_{BF}, as

$$\Delta n_{\mathrm{FCA}}(z,\tau) = -\frac{\alpha_{\mathrm{FCA}}}{2k_0}\Delta g_{\mathrm{FCA}}(z,\tau); \quad \Delta n_{\mathrm{BF}}(z,\tau) = -\frac{\alpha_{\mathrm{BF}}}{2k_0}\Delta g_{\mathrm{BF}}(z,\tau)\,. \tag{A.5}$$

By making use of the requirement Eq. (A.1) in Eq. (A.5), one can derive the inequality

$$\left|\Delta n_{\mathrm{FCA}}(z,\tau)\right| \ll \frac{\left|\alpha_{\mathrm{FCA}}\right|}{\alpha_{\mathrm{BF}}}\left|\Delta n_{\mathrm{BF}}(z,\tau)\right|\,. \tag{A.6}$$

We take into account that $\Delta n_{\mathrm{FCA}} < 0$ and $\Delta n_{\mathrm{BF}} > 0$ hold, multiply both sides of the inequality in Eq. (A.6) with $(-k_0)$, integrate over the SOA length, use the definitions of the partial phase shifts, Eq. (4.21), and obtain

$$\Delta\varphi_{\mathrm{FCA}}(\tau) \ll \frac{\left|\alpha_{\mathrm{FCA}}\right|}{\alpha_{\mathrm{BF}}}\left|\Delta\varphi_{\mathrm{BF}}(\tau)\right|\,. \tag{A.7}$$

Both phase shifts $\Delta\varphi_{\mathrm{FCA}}(\tau)$ and $\Delta\varphi_{\mathrm{BF}}(\tau)$ are known in our model, and we can thus establish the retarded time $\tau = \tau_{\mathrm{dip}}$ at which the ratio $\Delta\varphi_{\mathrm{FCA}}(\tau)/\left|\Delta\varphi_{\mathrm{BF}}(\tau)\right|$ reaches its highest value. The large effect in the FCA phase shift illustrated in Fig. 4.4(c) requires the following upper bound for the (negative) α -factor associated to FCA$_{\mathrm{TPA}}$,

$$\alpha_{\mathrm{FCA}} \ll -\frac{\Delta\varphi_{\mathrm{FCA}}(\tau_{\mathrm{dip}})}{\left|\Delta\varphi_{\mathrm{BF}}(\tau_{\mathrm{dip}})\right|}\alpha_{\mathrm{BF}}\,. \tag{A.8}$$

Substituting $\Delta\varphi_{\mathrm{FCA}}\left(\tau_{\mathrm{dip}}\right) / \left|\Delta\varphi_{\mathrm{BF}}\left(\tau_{\mathrm{dip}}\right)\right| = 2$ from Fig. 4.4(c) and $\alpha_{\mathrm{BF}} = 3.8$ from Table 4.1 in Eq. (A.8), one finds $\left|\alpha_{\mathrm{FCA}}\right| \gg 7.6$.

We close this appendix with the following remark: When the change in gain due to $\mathrm{FCA}_{\mathrm{TPA}}$ compared with the change in the BF gain coefficient can be neglected, less than 50% free carriers are produced by TPA than removed by BF (see Eq. (A.4)), while the FCA phase shift can become twice as large as the BF phase shift.

End of paper [54], Appendix A.

Appendix B
Calculation of integrals relevant to the analytical model from Section 4.3.3

This section is transferred from Appendix B of the Optics Express paper [54]. The text has been altered with respect to variables, figures and figure positions to match the thesis.

Begin of paper [54], Appendix B.

Spectral signature of nonlinear effects in semiconductor optical amplifiers

A. Marculescu, S. Ó'Dúill, C. Koos, W. Freude, and J. Leuthold
Opt. Express **25**(24), 29526-29559 (2017)

In this appendix we review the integration of the propagation equation for the pulse power $P_{\mathrm{CD}}(z,\tau)$ when CR and all ultrafast processes (including TPA) are neglected. Subsequently, we develop a method for integrating arbitrary positive powers of $P_{\mathrm{CD}}(z,\tau)$ over z.

We assume a given input pulse shape $P_{\mathrm{in}}(\tau)$. Then the differential equation

$$\frac{\partial}{\partial z} P_{\mathrm{CD}}(z,\tau) = g_{\mathrm{CD}}(z,\tau) P_{\mathrm{CD}}(z,\tau) \tag{B.1}$$

together with the initial condition

$$P_{\mathrm{CD}}(0,\tau) = P_{\mathrm{in}}(\tau) \tag{B.2}$$

is equivalent to the integral equation

$$P_{\mathrm{CD}}\left(z,\tau\right)=P_{\mathrm{in}}\left(\tau\right)\exp\left[\int_{0}^{z}\mathrm{g}_{\mathrm{CD}}\left(z',\tau\right)\mathrm{d}z'\right]. \tag{B.3}$$

The decrease of the local gain coefficient $g_{\mathrm{CD}}\left(z,\tau\right)$ from its small-signal value g_0, being due to CD, is described by the rate equation (the product $P_{\mathrm{sat}}\tau_s$ denotes the saturation energy)

$$\frac{\partial}{\partial\tau}g_{\mathrm{CD}}\left(z,\tau\right)=-g_{\mathrm{CD}}\left(z,\tau\right)\frac{P_{\mathrm{CD}}\left(z,\tau\right)}{P_{\mathrm{sat}}\tau_s}, \tag{B.4}$$

with the initial condition

$$g_{\mathrm{CD}}\left(z,-\infty\right)=g_0 . \tag{B.5}$$

In view of Eq. (B.3) we integrate both side of Eqs. (B.4) and (B.5) over z, consider instead of $g_{\mathrm{CD}}\left(z,\tau\right)$ the dimensionless integral

$$h_{\mathrm{CD}}\left(z,\tau\right)=\int_{0}^{z}\mathrm{g}_{\mathrm{CD}}\left(z',\tau\right)\mathrm{d}z' \tag{B.6}$$

and derive the differential equation

$$\frac{\partial}{\partial\tau}h_{\mathrm{CD}}\left(z,\tau\right)=-\frac{P_{\mathrm{in}}\left(\tau\right)\left\{\exp\left[h_{\mathrm{CD}}\left(z,\tau\right)\right]-1\right\}}{P_{\mathrm{sat}}\tau_s}, \tag{B.7}$$

with the initial condition

$$h_{\mathrm{CD}}\left(z,-\infty\right)=g_0 z . \tag{B.8}$$

One can integrate the differential equation Eq. (B.7) by separating the variables and by noting that

$$\frac{1}{\exp\left[h_{\mathrm{CD}}\left(z,\tau\right)\right]-1}\,\frac{\partial}{\partial\tau}h_{\mathrm{CD}}\left(z,\tau\right)=\frac{\partial}{\partial\tau}\ln\left\{1-\exp\left[-h_{\mathrm{CD}}\left(z,\tau\right)\right]\right\}. \tag{B.9}$$

By taking into account Eq. (B.8), the solution can be read off from

$$\ln\left\{\frac{1-\exp\left[-h_{\mathrm{CD}}\left(z,\tau\right)\right]}{1-\exp\left(-g_0 z\right)}\right\}=-\frac{1}{P_{\mathrm{sat}}\tau_s}\int_{-\infty}^{\tau}P_{\mathrm{in}}\left(\tau'\right)\mathrm{d}\tau' . \tag{B.10}$$

Eq. (B.10) makes apparent a gain compression depending on the energy of the pulse integrated over a time interval that is much longer than the pulse width. Introducing the abbreviation

$$\mathcal{P}(\tau)=\exp\left[-\frac{1}{P_{\text{sat}}\tau_s}\int_{-\infty}^{\tau}P_{\text{in}}(\tau')\,\mathrm{d}\tau'\right], \tag{B.11}$$

one can write the solution of Eq. (B.7) as

$$h_{\text{CD}}(z,\tau)=-\ln\left\{1-\left[1-\exp(-g_0z)\right]\mathcal{P}(\tau)\right\}. \tag{B.12}$$

By substituting Eq. (B.12) in the right-hand side of Eq. (B.3), one obtains the following explicit solution of the propagation equation Eq. (B.1):

$$P_{\text{CD}}(z,\tau)=\frac{P_{\text{in}}(\tau)}{1-\left[1-\exp(-g_0z)\right]\mathcal{P}(\tau)}. \tag{B.13}$$

In order to compute integrals of arbitrary positive power of P_{CD}, we introduce the time dependent, dimensionless coefficients

$$C_n(\tau)=\frac{g_0}{\left[\exp(h_0)-1\right]^n}\int_0^L\left[\frac{P_{\text{CD}}(z,\tau)}{P_{\text{in}}(\tau)}\right]^n\mathrm{d}z\ , \tag{B.14}$$

for $n=1,2,3...$. For further convenience we set $G_0=\exp(h_0)$, $h_0+\Delta h_{\text{CD}}(\tau)=h_{\text{CD}}(L,\tau)$, and $\mathrm{G}_{\text{CD}}(\tau)=\exp\left[h_{\text{CD}}(L,\tau)\right]$. Then with help of Eq. (B.13) the coefficient $C_n(\tau)$ takes the form

$$C_n(\tau)=\frac{g_0}{(G_0-1)^n}\int_0^L\frac{\mathrm{d}z}{\left\{1-\left[1-\exp(-g_0z)\right]\mathcal{P}(\tau)\right\}^n}. \tag{B.15}$$

We provisorily suppress the time dependency and change the integration variable in Eq. (B.15) according to

$$u=1-\left[1-\exp(-g_0z)\right]\mathcal{P}. \tag{B.16}$$

We note that $u\big|_{z=0}=1$ and

$$u\big|_{z=L}=1-\left[1-\exp(-h_0)\right]\mathcal{P}=G_{\text{CD}}^{-1}, \tag{B.17}$$

where the last equality in Eq. (B.17) immediately follows from Eq. (B.12) with $z=L$. Using

$$g_0 \mathrm{d}z = -\frac{\mathrm{d}u}{u-(1-\mathcal{P})} \tag{B.18}$$

and getting back the time dependency, one finds

$$C_n(\tau) = (G_0-1)^{-n} \int_{G_{\mathrm{CD}}^{-1}(\tau)}^{1} \frac{\mathrm{d}u}{u^n\left[u-1+\mathcal{P}(\tau)\right]}. \tag{B.19}$$

Such integrals can be calculated by partial fraction expansion. For $n=1$ the integral in Eq. (B.19) gives

$$\int \frac{\mathrm{d}u}{u(u-b)} = \frac{1}{b}\int\left(\frac{1}{u-b}-\frac{1}{u}\right)\mathrm{d}u = \frac{1}{b}\ln\left(1-bu^{-1}\right) \tag{B.20}$$

with $b=1-\mathcal{P}$. By using the integration limits $u=1$ and $u=G_{\mathrm{CD}}^{-1}$ in Eq. (B.20), the equality on the right-hand side of Eq. (B.17) and the identity

$$b(G_0-1) = \frac{G_0}{G_{\mathrm{CD}}}-1, \tag{B.21}$$

one obtains $C_1(\tau)$ in the form announced by Eq. (4.49)

$$C_1(\tau) = \left[\frac{G_0}{G_{\mathrm{CD}}(\tau)}-1\right]^{-1} \ln\left[\frac{G_0}{G_{\mathrm{CD}}(\tau)}\right]. \tag{B.22}$$

For higher n one can derive a recurrence relation by noting the identity

$$\begin{aligned} \int \frac{\mathrm{d}u}{u^n(u-b)} &= \int \frac{u-b+b}{u^{n+1}(u-b)}\mathrm{d}u \\ &= -\frac{1}{n\,u^n} + b\int \frac{\mathrm{d}u}{u^{n+1}(u-b)}. \end{aligned} \tag{B.23}$$

One finds that the coefficients $C_{n+1}(\tau)$ and $C_n(\tau)$ are related by

$$C_{n+1}(\tau) = \left[\frac{G_0}{G_{\mathrm{CD}}(\tau)}-1\right]^{-1}\left[C_n(\tau)-\frac{G_{\mathrm{CD}}^n(\tau)-1}{n(G_0-1)^n}\right]. \tag{B.24}$$

Eq. (B.24) shows that all $C_n(\tau)$ can be expressed in terms of the gain contribution $\Delta h_{\mathrm{CD}}(\tau)$ given by Eq. (4.29). In particular, for $n=2$, one finds Eq. (4.58)

$$C_2(\tau) = \left[\frac{G_0}{G_{\mathrm{CD}}(\tau)} - 1 \right]^{-1} \left[C_1(\tau) - \frac{G_{\mathrm{CD}}(\tau) - 1}{G_0 - 1} \right]. \tag{B.25}$$

Some properties of the functions $C_n(\tau)$ are useful for recognizing their role in the gain and phase shift dynamics. From the definition Eq. (B.14) it follows immediately that all $C_n(\tau)$ are positive

$$C_n(\tau) > 0. \tag{B.26}$$

By differentiating both sides of Eq. (B.15) with respect to τ and by taking into account the definition of $\mathcal{P}(\tau)$, Eq. (B.11), one obtains

$$\frac{\mathrm{d}}{\mathrm{d}\tau} C_n(\tau) = -\frac{n g_0}{(G_0 - 1)^n} \frac{P_{\mathrm{in}}(\tau)}{P_{\mathrm{sat}}\,\tau_s} \mathcal{P}(\tau) \int_0^L \frac{\left[1 - \exp(-g_0 z)\right]\mathrm{d}z}{\left\{1 - \left[1 - \exp(-g_0 z)\mathcal{P}(\tau)\right]\right\}^{n+1}}. \tag{B.27}$$

Obviously, the right-hand side of Eq. (B.27) is negative implying that $C_n(\tau)$ is a decreasing monotonic function of time with its largest value reached at $\tau = -\infty$. Substituting $\mathcal{P}(-\infty) = 1$ and $G_{\mathrm{CD}}(-\infty) = G_0$ into Eq. (B.19), one can readily perform the integral over u with the result

$$C_n(-\infty) = \frac{G_0^n - 1}{n(G_0 - 1)^n}. \tag{B.28}$$

In particular, $C_1(-\infty) = 1$ and $C_2(-\infty) = (G_0 + 1)/\left[2(G_0 - 1)\right]$. For an unsaturated SOA gain $G_0 > 20\,\mathrm{dB}$, the right-hand side of Eq. (B.28) can be approximated by $1/n$.

End of paper [54], Appendix B.

Appendix C
Degenerate and nondegenerate TPA-processes

C.1 Absorption coefficient

In this appendix we give a detailed description of the degenerate and nondegenerate TPA process in terms of positive absorption coefficients, in contrast with the form in the main text, where the absorption coefficients are considered as negative gain coefficients.

A light beam of power $P(z,\tau)$ propagating through an SOA along the z-axis undergoes an absorption process [65, 67-69, 108]. The waveguide structure of the SOA provides for each specific absorption process a well-defined area A_{eff}, which is usually larger than the area A of the active region, because it always includes some adjacent layers within the cladding region. Let us consider a light beam of central angular frequency ω, polarization unit-vector $\vec{e}$ and intensity $I(z,\tau)$,

$$I(z,\tau)=\frac{P(z,\tau)}{A_{\text{eff}}}\,. \tag{C.1}$$

By definition, the absorption coefficient $a(z,\tau)$ is the fractional decrease of the light intensity per unit beam path,

$$a(z,\tau)=-\frac{1}{I(z,\tau)}\frac{\partial}{\partial z}I(z,\tau)\,. \tag{C.2}$$

With help of Eq. (C.1), one can express Eq. (C.2) in the form

$$-\frac{1}{A_{\text{eff}}}\frac{\partial}{\partial z}P(z,\tau)=a(z,\tau)I(z,\tau)\,. \tag{C.3}$$

The left-hand side of Eq. (C.3) represents the power loss per unit volume. If this power is divided by the photon energy $\hbar\omega$, one finds the density $N(z,\tau)$ of photons absorbed per second,

$$N(z,\tau)=\frac{a(z,\tau)I(z,\tau)}{\hbar\omega}\,. \tag{C.4}$$

Conversely, if the density of photons absorbed per second is known, the absorption coefficient can be found from

$$a(z,\tau)=\frac{\hbar\omega N(z,\tau)}{I(z,\tau)}\,. \tag{C.5}$$

Example: Linear absorption. The absorption coefficient does not depend on the light intensity. Eq. (C.2) can be integrated and gives the Beer-Lambert law

$$I(z,\tau)=I(0,\tau)\exp\left[-\int_0^z a(z',\tau)\,\mathrm{d}z'\right]. \tag{C.6}$$

C.2 Degenerate two-photon absorption (TPA)

In a degenerate TPA process, the absorption coefficient is proportional to the light intensity with a proportionality factor $\beta(\omega)$ called the TPA coefficient at angular frequency ω,

$$a_{\mathrm{TPA}}(z,\tau)=\beta(\omega)I(z,\tau)\,. \tag{C.7}$$

The density of photons $N_2(z,\tau)$ absorbed per second is found by substituting Eq. (C.7) in Eq. (C.4),

$$N_2(z,\tau)=\frac{\beta(z,\tau)I^2(z,\tau)}{\hbar\omega}\,. \tag{C.8}$$

Since now photons are absorbed in pairs, the absorption rate per unit volume is given by $1/2\,N_2(z,\tau)$.

We consider now two light beams propagating through the SOA, a pump (labeled by S) and a probe light (labeled by $\times$). The i -th beam ($i=S,\times$) has a central angular frequency ω_i , a polarization unit-vector $\vec{e}_i$ and an intensity $I_i(z,\tau)$. Each beam undergoes separately a degenerate TPA process. Denoting with $\beta_i=\beta(\omega_i)$ the TPA coefficient at angular frequencies ω_i , one can express the degenerate absorption coefficient $a_{\mathrm{TPA},i}(z,\tau)$ and the density of photons absorbed per second $N_{2i}(z,\tau)$ as

$$a_{\mathrm{TPA},i}\left(z,\tau\right)=\beta_i I_i\left(z,\tau\right) \tag{C.9}$$

and

$$N_{2i}\left(z,\tau\right)=\frac{a_{\mathrm{TPA},i}\left(z,\tau\right)I_i\left(z,\tau\right)}{\hbar\omega_i}=\frac{\beta_i I_i^2\left(z,\tau\right)}{\hbar\omega_i}\,, \tag{C.10}$$

respectively.

C.3 Nondegenerate TPA process

In the pump-probe experiment above, nondegenerate photon pairs consisting of one photon from the pump and another photon from the probe light, can simultaneously be absorbed. In order to have a nondegenerate TPA process the densities of photons absorbed per second from the pump and probe light, $N_{1S}\left(z,\tau\right)$ and $N_{1\times}\left(z,\tau\right)$, must be equal

$$N_{1S}\left(z,\tau\right)=N_{1\times}\left(z,\tau\right). \tag{C.11}$$

In contrast with the degenerate case, the photons are now absorbed one-by-one, i.e., through a single-photon absorption process from each beam. The quantity $N_{1i}\left(z,\tau\right)$ represents the absorption rate per unit volume experienced in a nondegenerate TPA-process by the i-th beam, while the absorption rate is $N_{2i}/2$ for a degenerate process. The total number of photons absorbed from the i-th beam per second and unit volume is

$$N_i\left(z,\tau\right)=N_{2i}\left(z,\tau\right)+N_{1i}\left(z,\tau\right). \tag{C.12}$$

According to Eq. (C.4), $N_i\left(z,\tau\right)$ determines the absorption coefficient $a_i\left(z,\tau\right)$ experienced by the i-th beam as

$$N_i\left(z,\tau\right)=\frac{a_i\left(z,\tau\right)I_i\left(z,\tau\right)}{\hbar\omega_i}. \tag{C.13}$$

We now combine Eqs. (C.10), (C.12) and (C.13) to find $N_{1S}\left(z,\tau\right)$ and $N_{1\times}\left(z,\tau\right)$, and substitute these results in Eq. (C.11),

$$\frac{\left[a_S\left(z,\tau\right)-\beta_S I_S\left(z,\tau\right)\right]I_S\left(z,\tau\right)}{\hbar\omega_S}=\frac{\left[a_\times\left(z,\tau\right)-\beta_\times I_\times\left(z,\tau\right)\right]I_\times\left(z,\tau\right)}{\hbar\omega_\times}. \tag{C.14}$$

The only way to satisfy Eq. (C.14) is to assume

$$\begin{aligned} a_S(z,\tau) &= \beta_S I_S(z,\tau) + \beta_{S\times} I_\times(z,\tau), \\ a_\times(z,\tau) &= \beta_\times I_\times(z,\tau) + \beta_{\times S} I_S(z,\tau). \end{aligned} \tag{C.15}$$

The coefficients $\beta_{S\times}$ and $\beta_{\times S}$ depend on both angular frequencies ω_S, $\omega_\times$ and on the relative polarization angle $\cos^{-1}(\vec{e}_S \cdot \vec{e}_\times)$ and are related by

$$\frac{\beta_{S\times}}{\omega_S} = \frac{\beta_{\times S}}{\omega_\times}. \tag{C.16}$$

From Eq. (C.14) and Eq. (C.15) we obtain the following explicit expressions for N_{1S} and $N_{1\times}$,

$$\begin{aligned} N_{1S}(z,\tau) &= \frac{\beta_{S\times} I_S(z,\tau) I_\times(z,\tau)}{\hbar\omega_S}; \\ N_{2S}(z,\tau) &= \frac{\beta_{\times S} I_S(z,\tau) I_\times(z,\tau)}{\hbar\omega_\times}. \end{aligned} \tag{C.17}$$

The previous relations simplify when the beams have neighboring angular frequencies $\omega_S \approx \omega_\times \approx \omega_0$ [69]. Then $\beta_{S\times}$ and $\beta_{\times S}$ as well as β_S and $\beta_\times$ become respectively equal. A convenient parametrization can be obtained with the help of the TPA coefficient $\beta_2 = \beta(\omega_0)$ and the TPA non-degeneracy factor r_{TPA},

$$\beta_S \approx \beta_\times \approx \beta_2; \quad \beta_{S\times} \approx \beta_{\times S} \approx r_{\mathrm{TPA}}\beta_2. \tag{C.18}$$

C.4 Sufficiently weak probe light

By definition, a sufficiently weak probe light satisfies the following three conditions:

$$I_\times(z,\tau) \approx I_S(z,\tau); \tag{C.19}$$

$$\frac{1}{2} N_{2S}(z,\tau) \gg N_{1S}(z,\tau); \tag{C.20}$$

$$\frac{1}{2} N_{2\times}(z,\tau) \gg N_{1\times}(z,\tau). \tag{C.21}$$

Since the meaning of Eq. (C.19) is obvious, we consider only the other two requirements in the light of the discussion following Eq. (C.11). Eq. (C.20) tells us that the absorption rate experienced by the pump in a degenerate TPA process exceeds by far the absorption rate in the nondegenerate process.

Supposing that the probe photons absorbed per second and unit volume in the nondegenerate process ($N_{1\times}$) would actually be absorbed in a degenerate process, while the probe photons occurring in the degenerate TPA process ($N_{2\times}$) would be absorbed one-by-one as in a nondegenerate process. According to Eq. (C.21) the absorption rate in the former case, $N_{1\times}/2$, would remain larger than the absorption rate in the latter case, $N_{2\times}$.

By making use of Eq. (C.17), one can express Eqs. (C.19) and (C.20) as requirements involving the beam intensities,

$$\frac{2\beta_{S\times}}{\beta_S} I_\times(z,\tau) \ll I_S(z,\tau); \quad \frac{2\beta_\times}{\beta_{\times S}} I_\times(z,\tau) \ll I_S(z,\tau) . \tag{C.22}$$

These inequalities trivially follow from Eq. (C.18), except when the nonlinear TPA coefficients were restricted by

$$\frac{\beta_{S\times}}{\beta_S} \geq \frac{1}{2} \text{ and } \frac{\beta_{\times S}}{\beta_\times} \leq 2 . \tag{C.23}$$

For neighboring angular frequencies $\omega_S \approx \omega_\times \approx \omega_0$, one can use the parametrization in Eq. (C.18) and restrict the values of the non-degeneracy factor r_{TPA} to the range (see also [69, 108])

$$\frac{1}{2} \leq r_{\mathrm{TPA}} \leq 2 . \tag{C.24}$$

In the case of a sufficiently weak probe light the absorption coefficients $a_S(z,\tau)$ and $a_\times(z,\tau)$ depend only on the pump intensity and the non-degeneracy factor. From Eq. (C.15), it follows

$$a_S(z,\tau) \approx \beta_2 I_S(z,\tau); \quad a_\times(z,\tau) \approx \beta_2 r_{\mathrm{TPA}} I_S(z,\tau) . \tag{C.25}$$

C.5 Kerr nonlinearity

The changes of the refractive index due to TPA in a pump-probe experiment, $\Delta n_{\mathrm{TPA},i}(z,\tau)$, with $i = S,\times$, can be described along the same pattern as the absorption coefficients $a_i(z,\tau)$. For neighboring angular frequencies and a sufficiently weak probe light these changes take a form similar to Eq. (C.25),

$$\Delta n_{\mathrm{TPA},S}(z,\tau) = n_2 I_S(z,\tau); \quad \Delta n_{\mathrm{TPA},\times}(z,\tau) = r_{\mathrm{TPA}} n_2 I_S(z,\tau) \tag{C.26}$$

Here n_2 is known as the Kerr nonlinearity. As thoroughly discussed in Ref. [67], Kramers-Kronig dispersion relations can be used to connect nonlinear absorption and refraction. Although not always correct as absorption spectra cover a large frequency range, sometimes it is possible and convenient to use a TPA α -factor at angular frequency $\omega_0 \approx \omega_S \approx \omega_\times$, defined as

$$\alpha_{\mathrm{TPA}} = \alpha_{\mathrm{TPA}}\left(\omega_0\right) = 2k_0 \frac{n_2}{\beta_2}, \quad k_0 = \frac{\omega_0}{c}. \tag{C.27}$$

For bulk SOAs based on InGaAsP which are operated near the wavelength $\lambda_0 = 2\pi/k_0 = 1550\,\mathrm{nm}$, one can take $\beta_2 = 35\,\mathrm{cm/GW}$ and $\alpha_{\mathrm{TPA}} = -3$. Eq. (C.27) gives then $n_2 = -1.295\times10^{-16}\ \mathrm{m^2/W}$.

List of abbreviations

Special symbols

$\mathbb{P}$	Cauchy principal value Eq. (3.9)

Calligraphic symbols

$\mathcal{E}_{\gamma}$	Slowly-varying complex-valued electric field envelope, unit $\sqrt{\mathrm{W}}$ Eq. (4.5)
$\mathscr{L}(W)$	Lorentzian lineshape function, unit J^{-1} Eq. (2.10)

Greek symbols

α_{x}	Alpha factor associated with the process “x”, x=BF,CH,TPA Eq. (3.20)
α_{int}	Loss coefficient, unit m^{-1} Eq. (2.13)
β_2	TPA coefficient, unit $\mathrm{cm/GW}$ Eq. (4.39)
$\bar{\beta}_2$	TPA coefficient, unit m^2 Eq. (3.1)
Γ	Confinement factor, unit m^{-1} Eq. (2.13)
ε_0	Electric permittivity of the vacuum, $\varepsilon_0 = 8.85419 \times 10^{-12}\ \mathrm{As/Vm}$ Eq. (1.1)
ε , $\bar{\varepsilon}$	Ultrafast compression coefficient, unit $\mathrm{W}^{-1}, \mathrm{m}^3$ Eq. (2.27), Eq. (3.3)
ε_{x}	Compression coefficient associated with the process “x”, unit W^{-1} x=CH,SHB Eq. (4.34) x=TPA Eq. (4.48)
η_{FCA}	Nonlinear optical parameter associated with the change in the refractive index due to FCA$_{\mathrm{TPA}}$, unit W^{-1} Eq. (4.56)
Θ	Power spectrum, unit Js Eq. (4.64)
λ	Wavelength, unit m
ρ_{e}	Density of energy states for electrons, unit $\mathrm{J}^{-1}\mathrm{m}^{-3}$ Eq. (2.3)
ρ_{h}	Density of energy states for holes, unit $\mathrm{J}^{-1}\mathrm{m}^{-3}$ Eq. (2.4)

σ_β	Cross-section for FCA$_{\mathrm{BF}}$ in the band β , β =CB,VB, unit m^2 Eq. (2.19)
τ	Retarded time, unit s
τ_s	Spontaneous carrier lifetime, unit s Eq. (2.19)
τ_0	Intervalley scattering time, unit s Table 4.1
τ_{cr}	Critical pulse length, unit s
τ_{BF}	Time constant for carrier recovery, unit s Eq. (3.5)
τ_{delay}	Time interval between the arrival of the pulse and the onset of ultrafast recovery, unit s Eq. (3.5)
τ_{uf}	Burning time constant for an intraband spectral hole, unit s Eq. (3.5)
τ_{x}	Relaxation or characteristic time constant for the process “x”, unit s x=CD,CH,CI,FCA,SHB,TPA Fig. 3.4
τ_{ex}	Average lifetime of photoexcited electrons, unit s Eq. (4.53)
ϕ	Complete phase Eq. (3.25)
ϕ_1	Constant phase shift for each mark bit Fig. 6.12
ϕ_2	Constant phase shift for each space bit Fig. 6.12
φ	Phase shift Eq. (3.25)
$\chi^{(N)}_{i\,j_1\ldots j_N}$	Tensor component of the N-th order influence function, unit $(\mathrm{m/V})^{\mathrm{N\text{-}1}}$ Eq. (1.1)
$\underline{\chi}^{(1)}(\omega)$	Linear susceptibility, Eq. (1.4)
ω	Angular frequency, unit $\mathrm{rad/s}$
ω_0	Central angular frequency, unit $\mathrm{rad/s}$
ω_S	Angular frequency of the pump signal, unit $\mathrm{rad/s}$
$\omega_\times$	Angular frequency of the probe signal, unit $\mathrm{rad/s}$

Latin symbols

A	Cross-section area, unit m^2
A_{eff}	Effective cross-section, unit m^2 Eq. (2.17)

A_{TPA}	TPA cross-section, unit m^2 Eq. (4.39)
a	Absorption coefficient, unit m^{-1} Eq. (1.8)
a_0	Differential gain, unit m^2 Eq. (2.16)
$C_1(\tau)$	Coefficient function associated with TPA Eq. (4.49)
$C_2(\tau)$	Coefficient function associated with FCA$_{\mathrm{TPA}}$ Eq. (4.58)
c	Vacuum speed of light, $c = 299792458\,\mathrm{m/s}$ Eq. (1.8)
$\vec{E}$	Electric vector field, unit $\mathrm{V/m}$ Eq. (1.1)
E_γ	Normalized root-mean-squared electric field, unit $\sqrt{\mathrm{W}}$ Eq. (4.2)
E_γ^{in}	Normalized root-mean-squared electric field at SOA input, unit $\sqrt{\mathrm{W}}$ Eq. (4.3)
E_γ^{out}	Normalized root-mean-squared electric field at SOA output, unit $\sqrt{\mathrm{W}}$ Eq. (4.4)
e	Elementary charge, $e = 1.6 \times 10^{-19}\,\mathrm{As}$ Eq. (2.30)
$\vec{e}_y$	Unit vector along the y-axis, Eq. (3.24)
FLS	Fermi-level separation, unit J Fig. 2.3
f	Instantaneous frequency, unit Hz
f_{rep}	Pulse repetition frequency, unit Hz Fig. 3.3
f_{e}	Fermi-Dirac distribution for electrons Eq. (2.1)
f_{h}	Fermi-Dirac distribution for holes Eq. (2.2)
G	SOA power gain Eq. (2.12)
G_0	SOA small-signal gain Eq. (2.15)
$g_\gamma(z,t)$	Modal gain coefficient, unit m^{-1} Eq. (4.6)
$\bar{g}_0$	Small-signal gain coefficient, unit m^{-1} Eq. (2.11)
g_0	Small-signal gain coefficient including the field confinement factor, unit m^{-1} Eq. (2.11)
g_{m}	Material power gain coefficient, unit m^{-1} Eq. (2.13)
g_{BF}	BF gain contribution, unit m^{-1} Eq. (2.27)

Δg_x	Change in the modal gain due to the process “ x ” x=BF,CH,SHB,TPA, unit m^{-1} Eq. (4.18)
h	Logarithmic power gain Eq. (4.13)
h_0	Unsaturated device gain Eq. (4.15)
Δh_x	Change in the integrated gain coefficient due to the process “ x ” x=BF,CH,SHB,TPA, unit m^{-1} Eq. (4.18)
$\hbar$	Reduced Planck constant, $\hbar = 1.05457 \times 10^{-34}\ \mathrm{Js}$ Eq. (2.3)
I	Bias current, unit A Eq. (2.17)
j	Imaginary unit, $\mathrm{j}^2 = -1$
$\vec{\mathrm{K}}$	Electron wave vector, unit m^{-1} Fig. 2.3
k_0	Free-space wave vector, unit m^{-1}
k_{B}	Boltzmann constant, $k_{\mathrm{B}} = 1.38065 \times 10^{-23}\ \mathrm{J/K}$ Eq. (2.1)
L	SOA length, unit m
$M(W)$	Dipole matrix element, unit Asm Eq. (2.9)
m_{e}	Effective mass of electron, unit free electron mass $m_0 = 9.109 \times 10^{-31}\ \mathrm{kg}$ Eq. (2.3)
m_{h}	Effective mass of hole, unit free electron mass m_0 Eq. (2.4)
m_{FCA}	Effective mass of FCA$_{\text{TPA}}$ excited electron, unit free electron mass m_0 Eq. (4.51)
N	Carrier concentration, unit m^{-3} Eq. (2.16)
N_{e}	Electron concentration, unit m^{-3} Eq. (2.5)
N_{h}	Hole concentration, unit m^{-3} Eq. (2.6)
N_{ex}	Density of photoexcited, unit m^{-3} Eq. (4.52)
N_{FCA}	Density of FCA$_{\text{TPA}}$ excited electrons, unit m^{-3} Eq. (4.51)
N_{tr}	Carrier density at transparency, unit m^{-3} Eq. (2.16)
n	Refractive index Eq. (1.8)
$\underline{n}$	Complex-valued refractive index Eq. (1.7)

n_i	Imaginary part of the complex refractive index Eq. (3.7)
n_0	Effective refractive index at central angular frequency Eq. (2.11)
n_2	Kerr nonlinear index coefficient, unit $\mathrm{m^2/W}$ Eq. (3.21)
Δn	Change in the refractive index, Eq. (2.29)
Δn_{FCA}	Change in the refractive index due to the FCA$_{\text{TPA}}$ process, Eq. (4.51)
$\vec{P}$	Electric polarization vector, unit $\mathrm{As/m^2}$ Eq. (1.1)
$\vec{P}_{\mathrm{L}}$	Linear electric polarization vector, unit $\mathrm{As/m^2}$ Eq. (1.2)
P	Power, unit W Eq. (2.13)
P_{in}	Input power, unit W Eq. (2.12)
P^{out}	Output power, unit W Eq. (2.12)
P_{CW}	CW probe light power, unit W Fig. 3.8
P_{D}	Power of the control signal, unit W Fig. 4.15
P_{sat}	Saturation power, unit W Eq. (2.23)
$P_{\mathrm{sat}}^{\mathrm{out}}$	3 dB saturation power, unit W Eq. (2.25)
Q^2	Quality factor
q	Gain reduction at saturation onset Eq. (4.30)
r_{TPA}	TPA non-degeneracy factor Eq. (4.42)
S	Photon density, unit $\mathrm{m^{-3}}$ Eq. (2.28)
T	Absolute temperature, unit K
t	Time, unit s
v_g	Group velocity, unit $\mathrm{m/s}$ Eq. (2.28)
x , y , z	Spatial coordinates, unit m
V	Active volume, unit $\mathrm{m^3}$
W	Carrier energy, unit J Fig. 2.3
W_{e} , W_{h}	Kinetic energy of charged carriers, unit J Fig. 2.3
$W_{\mathrm{F,e}}$, $W_{\mathrm{F,h}}$	Quasi-Fermi level energy of charged carriers, unit J Fig. 2.3

W_G	Bandgap energy, unit J	Fig. 2.3

Acronyms

1R	Re-amplification
2R	1R + Re-shaping
3R	2R + Re-timing
AOWC	All-optical wavelength conversion
AND	Logic AND function
ASE	Amplified spontaneous emission
BER	Bit error-rate
BF	Band filling
BPF	Bandpass filter
BS	Blue-shifted
BSOF	Blue-shifted optical filter
CB	Conduction band
CC	Carrier cooling
CD	Carrier depletion
CH	Carrier heating
CI	Carrier injection
CR	Carrier recovery
CSRZ	Carrier-suppressed return-to-zero
CW	Continuous wave
DI	Delay interferometer
DWDM	Dense wavelength division multiplex
EDFA	Erbium-doped fiber amplifier
$\mathrm{FCA}_{\mathrm{BF}}$	Free carrier absorption
$\mathrm{FCA}_{\mathrm{TPA}}$	TPA-induced free carrier absorption

FCI	Free carrier index change
FREAG	Frequency resolved electro-absorption gating
FWHM	Full width at half maximum
ISI	Inter-symbol-interference
NRZ	Non-return-to-zero
ODL	Optical delay line
OR	Logic OR function
OSA	Optical spectrum analyzer
OSNR	Optical signal-to-noise-ratio
P	Power meter
PMD	Polarization mode dispersion
PPS	Progressive phase shift
PRBS	Pseudo-random bit sequence
PROF	Pulse reformatting optical filter
RS	Red-shifted
RSOF	Red-shifted optical filter
RZ	Return-to-zero
SHB	Spectral hole burning
SOA	Semiconductor optical amplifier
SPM	Self-phase modulation
SSB	Single side band
TOAD	Terahertz optical asymmetric demultiplexer
TPA	Two-photon absorption
TE	Transverse electric (mode)
TM	Transverse magnetic (mode)
VB	Valence band
VOA	Variable optical attenuator

VSB	Vestigial sideband
WDM	Wavelength division multiplexing
XGM	Cross-gain modulation
XOR	Exclusive OR logic gate
XPM	Cross-phase modulation

Bibliography

[1] R. W. Boyd, *Nonlinear Optics,* first ed. (Academic Press, 1992).

[2] B. S. Wherrett, "From linear dispersion to self-induced transparency: An introduction to nonlinear optics," in *Nonlinear Optics: Proceedings of the Sixteenth Scottish Universities Summer School in Physics, 1975*, P. G. Harper and B. S. Wherrett, eds. (Academic Press, 1977).

[3] W. Freude "Volterra-Reihen," (University of Karlsruhe, 1998).

[4] K. Batselier, Z. Chen, H. Liu, and N. Wong, "A tensor-based volterra series black-box nonlinear system identification and simulation framework," in *IEEE/ACM International Conference on Computer-Aided Design (ICCAD)*, (IEEE, 2016), 1-7.

[5] J. L. Oudar, "Transient Optical Effects in Semiconductors," in Nonlinear Optics: Materials and Devices: Proceedings of the International School of Materials Science and Technology, Erice, Sicily, July 1-14, 1985, C. Flytzanis and J. L. Oudar, eds. (Springer, 1986).

[6] A. D'Ottavi, "Investigation of carrier heating and spectral hole burning in semiconductor amplifiers by highly nondegenerate four-wave mixing," Appl. Phys. Lett. **64**(19), 2492 (1994).

[7] M. J. Connelly, *Semiconductor Optical Amplifiers* (Kluwer Academic Publishers, 2002).

[8] N. M. Ravindra, P. Ganapathy, and J. Choi, "Energy gap–refractive index relations in semiconductors – An overview," Infrared Phys. Technol. **50**(1), 21-29 (2007).

[9] H. G. Weber, "Nichtlineare Optik und optische Signalverarbeitung," in *Optische Kommunikationstechnik - Handbuch für Wissenschaft und Industrie*, E. Voges and K. Petermann, eds. (Springer, 2002).

[10] J. Leuthold, Advanced InP Waveguide MZI All-Optical Switches and Wavelength Converters (Hartung-Gorre Verlag, Konstanz, 1999).

[11] G. P. Agrawal, *Fiber-Optic Communication Systems* (John Wiley & Sons, 2002).

[12] G. Grau and W. Freude, *Optische Nachrichtentechnik: Eine Einführung* (Springer, 1991).Since 1997 out of print; corrected KIT reprint available 1998, 1999, 2005 (send email to w.freude@kit.edu).

[13] B. R. Bennett, R. A. Soref, and J. A. Del Alamo, "Carrier-induced change in refractive index of InP, GaAs and InGaAsP," IEEE J. Quantum Electron. **26**(1), 113-122 (1990).

[14] A. Matsumoto, K. Nishimura, K. Utaka, and M. Usami, "Operational design on high-speed semiconductor optical amplifier with assist light for application to wavelength converters using cross-phase modulation," IEEE J. Quantum Electron. **42**(3), 313-323 (2006).

[15] R. J. Manning and D. A. O. Davies, "Three-wavelength device for all-optical signal processing," Opt. Lett. **19**(12), 889-891 (1994).

[16] J. Mørk, J. Mark, and C. P. Seltzer, "Carrier heating in InGaAsP laser amplifiers due to two-photon absorption," Appl. Phys. Lett. **64**(17), 2206-2208 (1994).

[17] G. P. Agrawal and N. A. Olsson, "Self-phase modulation and spectral broadening of optical pulses in semiconductor laser amplifiers," IEEE J. Quantum Electron. **25**(11), 2297-2306 (1989).

[18] M. J. Adams, D. A. O. Davies, M. C. Tatham, and M. A. Fisher, "Nonlinearities in semiconductor laser amplifiers," Opt. Quantum Electron. **27**(1), 1-13 (1995).

[19] K. L. Hall, E. R. Thoen, and E. P. Ippen, "Nonlinearities in active media," in *Nonlinear Optics in Semiconductors II, Semiconductors & Semimetals*, E. Garmire and A. Kost, eds. (Academic Press, 1999).

[20] K. L. Hall, G. Lenz, A. M. Darwish, and E. P. Ippen, "Subpicosecond gain and index nonlinearities in InGaAsP diode lasers," Opt. Commun. **111**(5-6), 589-612 (1994).

[21] J. Mørk, W. Berg, M. L. Nielsen, and A. V. Uskov, "The role of fast carrier dynamics in SOA based devices," IEICE Trans. Electron. **E87-C**(7), 1126-1133 (2004).

[22] M. Willatzen, A. Uskov, J. Mork, H. Olsen, B. Tromborg, and A. P. Jauho, "Nonlinear gain suppression in semiconductor lasers due to carrier heating," IEEE Photonics Technol. Lett. **3**(7), 606-609 (1991).

[23] J. Mark and J. Mørk, "Subpicosecond gain dynamics in InGaAsP optical amplifiers: Experiment and theory," Appl. Phys. Lett. **61**(19), 2281-2283 (1992).

[24] P. Borri, S. Scaffetti, J. Mork, W. Langbein, J. M. Hvam, A. Mecozzi, and F. Martelli, "Measurement and calculation of the critical pulsewidth for gain saturation in semiconductor optical amplifiers," Opt. Commun. **164**(1-3), 51-55 (1999).

[25] M. L. Nielsen, J. Mørk, R. Suzuki, J. Sakaguchi, and Y. Ueno, "Experimental and theoretical investigation of the impact of ultra-fast carrier dynamics on high-speed SOA-based all-optical switches," Opt. Express **14**(1), 331-347 (2006).

[26] F. Ginovart, J. C. Simon, and I. Valiente, "Gain recovery dynamics in semiconductor amplifiers," Opt. Commun. **199**(1-4), 111-115 (2001).

[27] G. Talli and M. J. Adams, "Gain dynamics of semiconductor optical amplifiers and three-wavelength devices," IEEE J. Quant. Electron. **39**(10), 1305-1313 (2003).

[28] F. Ginovart and J. C. Simon, "Semiconductor optical amplifier length effects on gain dynamics," J. Phys. D **36**(13), 1473-1476 (2003).

[29] J. L. Pleumeekers, M. Kauer, K. Dreyer, C. Burrus, A. G. Dentai, S. Shunk, J. Leuthold, and C. H. Joyner, "Acceleration of gain recovery in semiconductor optical amplifiers by optical injection near transparency wavelength," IEEE Photonics Technol. Lett. **14**(1), 12-14 (2002).

[30] M. T. Hill, E. Tangdiongga, H. d. Waardt, G. D. Khoe, and H. J. S. Dorren, "Carrier recovery time in semiconductor optical amplifiers that employ holding beams," Opt. Lett. **27**(18), 1625-1627 (2002).

[31] R. Inohara, K. Nishimura, M. Tsurusawa, and M. Usami, "Experimental analysis of cross-phase modulation and cross-gain modulation in SOA-injecting CW assist light," IEEE Photonics Technol. Lett. **15**(9), 1192-1194 (2003).

[32] X. Li, M. J. Adams, D. Alexandropoulos, and I. F. Lealman, "Gain recovery in semiconductor optical amplifiers," Opt. Commun. **281**(13), 3466-3470 (2008).

[33] R. Giller, R. J. Manning, G. Talli, R. P. Webb, and M. J. Adams, "Analysis of the dimensional dependence of semiconductor optical amplifier recovery speeds," Opt. Express **15**(4), 1773-1782 (2007).

[34] R. Giller and R. J. Manning, "Recovery dynamics of optically excited semiconductor optical amplifiers," in *Optical Fiber Communication*

Conference, OSA Technical Digest Series (Optical Society of America, 2006), OWI74.

[35] R. Giller, R. J. Manning, and D. Cotter, "Gain and phase recovery of optically excited semiconductor optical amplifiers," IEEE Photonics Technol. Lett. **18**(9), 1061-1063 (2006).

[36] V. Lucarini, J. J. Saarinen, K. E. Peiponen, and E. M. Vartiainen, *Kramers-Kronig Relations in Optical Materials Research* (Springer, 2005).

[37] C. H. Henry, R. A. Logan, and K. A. Bertness, "Spectral dependence of the change in refractive index due to carrier injection in GaAs lasers," J. Appl. Phys. **52**(7), 4457-4461 (1981).

[38] J. Mørk and A. Mecozzi, "Response function for gain and refractive index dynamics in active semiconductor waveguides," Appl. Phys. Lett. **65**(14), 1736-1738 (1994).

[39] C. T. Hultgren and E. P. Ippen, "Ultrafast refractive index dynamics in AlGaAs diode laser amplifiers," Appl. Phys. Lett. **59**(6), 635 (1991).

[40] J. M. Dailey and T. L. Koch, "Impact of carrier heating on SOA transmission dynamics for wavelength conversion," IEEE Photonics Technol. Lett. **19**(14), 1078-1080 (2007).

[41] C. Dorrer and I. Kang, "Simultaneous temporal characterization of telecommunication optical pulses and modulators by use of spectrograms," Opt. Lett. **27**(15), 1315-1317 (2002).

[42] I. Kang and C. Dorrer, "Measurements of gain and phase dynamics of a semiconductor optical amplifier using spectrograms," in *Optical Fiber Communications Conference*, OSA Technical Digest Series (Optical Society of America, 2004), MF43.

[43] J. Wang, A. Maitra, C. G. Poulton, W. Freude, and J. Leuthold, "Temporal dynamics of the alpha factor in semiconductor optical amplifiers," J. Lightwave Technol. **25**(3), 891-900 (2007).

[44] X. Yang, D. Lenstra, G. D. Khoe, and H. J. S. Dorren, "Nonlinear polarization rotation induced by ultrashort optical pulses in a semiconductor optical amplifier," Opt. Commun. **223**(1–3), 169-179 (2003).

[45] S. Kumar, B. Zhang, and A. E. Willner, "Elimination of data pattern dependence in SOA-based differential-mode wavelength converters using optically-induced birefringence," in *Optical Fiber Communications*

Conference, OSA Technical Digest Series (Optical Society of America, 2006), OThB3.

[46] C. T. Hultgren, D. J. Dougherty, and E. P. Ippen, "Above- and below-band femtosecond nonlinearities in active AlGaAs waveguides," Appl. Phys. Lett. **61**(23), 2767-2769 (1992).

[47] N. Y. Kim, X. Tang, J. C. Cartledge, and A. K. Atieh, "Design and performance of an all-pptical wavelength converter based on a semiconductor optical amplifier and delay interferometer," J. Lightwave Technol. **25**(12), 3730-3738 (2007).

[48] J. Mørk and A. Mecozzi, "Theory of the ultrafast optical response of active semiconductor waveguides," J. Opt. Soc. Am. B **13**(8), 1803-1816 (1996).

[49] T. P. Hessler, P. E. Selbmann, J. L. Pleumeekers, M. A. Dupertuis, B. Deveaud, R. Schreieck, J. Y. Emery, and B. Dagens, "Propagation effects on the ultrafast cross-gain modulation in semiconductor optical amplifiers," Opt. Commun. **248**(1-3), 267-280 (2005).

[50] R. S. Grant and W. Sibbett, "Observations of ultrafast nonlinear refraction in an InGaAsP optical amplifier," Appl. Phys. Lett. **58**(11), 1119-1121 (1991).

[51] Y. Ueno, S. Nakamura, and K. Tajima, "Nonlinear phase shifts induced by semiconductor optical amplifiers with control pulses at repetition frequencies in the 40-160-GHz range for use in ultrahigh-speed all-optical signal processing," J. Opt. Soc. Am. B **19**(11), 2573-2589 (2002).

[52] M. A. Fisher, H. Wickes, G. T. Kennedy, R. S. Grant, and W. Sibbett, "Ultrafast nonlinear refraction in an active MQW waveguide," Electron. Lett. **29**(13), 1185-1186 (1993).

[53] A. E. Siegman, *Lasers* (University Science Books, Mill Valley, 1986).

[54] A. Marculescu, S. Ó'Dúill, C. Koos, W. Freude, and J. Leuthold, "Spectral signature of nonlinear effects in semiconductor optical amplifiers," Opt. Express **25**(24), 29526-29559 (2017).

[55] S. Krishnamurthy, Z. G. Yu, L. P. Gonzalez, and S. Guha, "Temperature- and wavelength-dependent two-photon and free-carrier absorption in GaAs, InP, GaInAs, and InAsP," J. Appl. Phys. **109**(3), 033102-033109 (2011).

[56] P. Y. Yu and M. Cardona, *Fundamentals of Semiconductors,* fourth ed. (Springer, 2010).

[57] E. M. Conwell and M. O. Vassell, "High-field distribution function in GaAs," IEEE Trans. Electron Dev. **13**(1), 22-26 (1966).

[58] G. Klimeck, R. C. Bowen, T. B. Boykin, and T. A. Cwik, "sp3s* tight-binding parameters for transport simulations in compound semiconductors," Superlattices Microstruct. **27**(5-6), 519-524 (2000).

[59] P. Lunnemann, S. Ek, K. Yvind, R. Piron, and J. Mørk, "Nonlinear carrier dynamics in a quantum dash optical amplifier," New J. Phys. **14**(1), 013042 (2012).

[60] A. Mecozzi and J. Mørk, "Theory of heterodyne pump–probe experiments with femtosecond pulses," J. Opt. Soc. Am. B **13**(11), 2437-2452 (1996).

[61] A. Mecozzi and J. Mørk, "Saturation induced by picosecond pulses in semiconductor optical amplifiers," J. Opt. Soc. Am. B **14**(4), 761-770 (1997).

[62] M. Premaratne, D. Nesic, and G. P. Agrawal, "Pulse Amplification and gain recovery in semiconductor optical amplifiers: A systematic analytical approach," J. Lightwave Technol. **26**(12), 1653-1660 (2008).

[63] I. D. Rukhlenko, M. Premaratne, and G. P. Agrawal, "Nonlinear silicon photonics: Analytical tools," IEEE J. Sel. Top. Quantum Electron. **16**(1), 200-215 (2010).

[64] J. E. Carroll, J. Whiteaway, and D. Plumb, *Distributed Feedback Semiconductor Lasers* (IEEE, 1998).

[65] J. M. Tang and K. A. Shore, "Strong picosecond optical pulse propagation in semiconductor optical amplifiers at transparency," IEEE J. Quantum Electron. **34**(7), 1263-1269 (1998).

[66] A. Mecozzi and J. Mørk, "Saturation effects in nondegenerate four-wave mixing between short optical pulses in semiconductor laser amplifiers," IEEE J. Sel. Top. Quantum Electron. **3**(5), 1190-1207 (1997).

[67] M. Sheik-Bahae and E. W. Van Stryland, "Optical nonlinearities in the transparency region of bulk semiconductors," in *Nonlinear Optics in Semiconductors I*, E. Garmire and A. Kost, eds. (Academic Press, 1998).

[68] D. C. Hutchings and E. W. Van Stryland, "Nondegenerate two-photon absorption in zinc blende semiconductors," J. Opt. Soc. Am. B **9**(11), 2065-2074 (1992).

[69] B. V. Olson, M. P. Gehlsen, and T. F. Boggess, "Nondegenerate two-photon absorption in GaSb," Opt. Commun. **304**, 54-57 (2013).

[70] O. Raz, J. Herrera, and H. J. S. Dorren, "Enhanced 40 and 80 Gb/s wavelength conversion using a rectangular shaped optical filter for both red and blue spectral slicing," Opt. Express **17**(3), 1184-1193 (2009).

[71] J. Leuthold, R. Ryf, D. N. Maywar, S. Cabot, J. Jaques, and S. S. Patel, "Nonblocking all-optical cross connect based on regenerative all-optical wavelength converter in a transparent demonstration over 42 nodes and 16800 km," J. Lightwave Technol. **21**(11), 2863-2870 (2003).

[72] M. L. Nielsen, B. Lavigne, and B. Dagens, "Polarity-preserving SOA-based wavelength conversion at 40 Gbit/s using bandpass filtering," Electron. Lett. **39**(18), 1334 (2003).

[73] Y. Liu, E. Tangdiongga, Z. Li, H. de Waardt, A. M. J. Koonen, G. D. Khoe, X. Shu, I. Bennion, and H. J. S. Dorren, "Error-free 320-Gb/s all-optical wavelength conversion using a single semiconductor optical amplifier," J. Lightwave Technol. **25**(1), 103-108 (2007).

[74] J. Leuthold, D. M. Marom, S. Cabot, J. J. Jaques, R. Ryf, and C. R. Giles, "All-optical wavelength conversion using a pulse reformatting optical filter," J. Lightwave Technol. **22**(1), 186-192 (2004).

[75] J. Wang, A. Marculescu, J. Li, P. Vorreau, S. Tzadok, S. Ben-Ezra, S. Tsadka, W. Freude, and J. Leuthold, "Pattern effect removal technique for semiconductor-optical-amplifier-based wavelength conversion," IEEE Photonics Technol. Lett. **19**(24), 1955-1957 (2007).

[76] X. Wei and J. Leuthold, "Relation between vestigial-sideband filtering and pi/2 progressive phase shift," Opt. Lett. **29**(14), 1599-1601 (2004).

[77] J. Wang, A. Marculescu, J. Li, Z. Zhang, W. Freude, and J. Leuthold, "All-optical vestigial-sideband signal generation and pattern effect mitigation with an SOA based red-shift optical filter wavelength converter," in *34th European Conference on Optical Communication (ECOC)*, (IEEE, 2008), We.2C6.

[78] A. Marculescu, S. Sygletos, J. Li, D. Karki, D. Hillerkuss, S. Ben-Ezra, S. Tsadka, W. Freude, and J. Leuthold, "RZ to CSRZ format and wavelength conversion with regenerative properties," in *Optical Fiber Communication*

Conference, OSA Technical Digest Series (Optical Society of America, 2009), OThS1.

[79] Z. Li, Y. Liu, S. Zhang, H. Ju, H. de Waardt, G. D. Khoe, H. J. S. Dorren, and D. Lenstra, "All-optical logic gates using semiconductor optical amplifier assisted by optical filter," Electron. Lett. **41**(25), 1397-1399 (2005).

[80] J. Leuthold, W. Freude, S. Sygletos, R. Bonk, T. Vallaitis, and A. Marculescu, "All-optical regeneration," in *Asia Communications and Photonics Conference*, OSA Technical Digest Series (Optical Society of America, 2009), TuK1.

[81] P. V. Mamyshev, "All-optical data regeneration based on self-phase modulation effect," in *24th European Conference on Optical Communication (ECOC)*, (IEEE, 1998), 475-476.

[82] M. L. Nielsen, B. E. Olsson, and D. J. Blumenthal, "Pulse extinction ratio improvement using SPM in an SOA for OTDM systems applications," IEEE Photonics Technol. Lett. **14**(2), 245-247 (2002).

[83] J. Leuthold, "Signal regeneration and all-optical wavelength conversion," in *15th Annual Meeting of the IEEE Lasers and Electro-Optics Society (LEOS)*, (IEEE, 2002), 107-108.

[84] T. Durhuus, B. Mikkelsen, C. Joergensen, S. L. Danielsen, and K. E. Stubkjaer, "All-optical wavelength conversion by semiconductor optical amplifiers," J. Lightwave Technol. **14**(6), 942-954 (1996).

[85] R. J. Manning, A. D. Ellis, A. J. Poustie, and K. J. Blow, "Semiconductor laser amplifiers for ultrafast all-optical signal processing," J. Opt. Soc. Am. B **14**(11), 3204-3216 (1997).

[86] R. J. Manning, X. Yang, R. P. Webb, and R. Giller, "The ‘turbo-switch’ - a novel technique to increase the high-speed response of SOAs for wavelength conversion," in *Optical Fiber Communications Conference*, OSA Technical Digest Series (Optical Society of America, 2006), OWS8.

[87] G. Contestabile, R. Proietti, N. Calabretta, and E. Ciaramella, "Cross-gain compression in semiconductor optical amplifiers," J. Lightwave Technol. **25**(3), 915-921 (2007).

[88] M. L. Nielsen and J. Mørk, "Increasing the modulation bandwidth of semiconductor-optical-amplifier-based switches by using optical filtering," J. Opt. Soc. Am. B **21**(9), 1606-1619 (2004).

[89] S. Nakamura, Y. Ueno, and K. Tajima, "168-Gb/s all-optical wavelength conversion with asymmetric-Mach-Zehnder-type switch," IEEE Photonics Technol. Lett. **13**(10), 1091-1093 (2001).

[90] J. Leuthold, B. Mikkelsen, R. E. Behringer, G. Raybon, C. H. Joyner, and P. A. Besse, "Novel 3R regenerator based on semiconductor optical amplifier delayed-interference configuration," IEEE Photonics Technol. Lett. **13**(8), 860-862 (2001).

[91] J. Leuthold, L. Moller, J. Jaques, S. Cabot, L. Zhang, P. Bernasconi, M. Cappuzzo, L. Gomez, E. Laskowski, E. Chen, A. Wong-Foy, and A. Griffin, "160 Gbit/s SOA all-optical wavelength converter and assessment of its regenerative properties," Electron. Lett. **40**(9), 554-555 (2004).

[92] E. Granot, R. Zaibel, N. Narkiss, S. Ben-Ezra, H. Chayet, N. Shahar, S. Sternklar, S. Tsadka, and P. R. Prucnal, "Tunable all-optical signal regenerator with a semiconductor optical amplifier and a Sagnac loop: principles of operation," J. Opt. Soc. Am. B **22**(12), 2534-2541 (2005).

[93] Z. Chen, J. Wu, K. Xu, and J. Lin, "Simultaneously all-optical inverted and noninverted wavelength conversion employing SOA-based Sagnac interferometer," Microwave Opt. Technol. Lett. **49**(3), 547-551 (2007).

[94] A. Gomez-Iglesias, J. G. Fenn, M. Mazilu, R. J. Manning, and A. Miller, "Carrier heating in semiconductor optical amplifier-based Sagnac-type all-optical switches," Semicond. Sci. Technol. **21**(12), 1703-1708 (2006).

[95] Y. Liu, M. T. Hill, E. Tangdiongga, H. de Waardt, N. Calabretta, G. D. Khoe, and H. J. S. Dorren, "Wavelength conversion using nonlinear polarization rotation in a single semiconductor optical amplifier," IEEE Photonics Technol. Lett. **15**(1), 90-92 (2003).

[96] S. Fu, J. Dong, P. Shum, L. Zhang, X. Zhang, and D. Huang, "Experimental demonstration of both inverted and non-inverted wavelength conversion based on transient cross phase modulation of SOA," Opt. Express **14**(17), 7587-7593 (2006).

[97] A. D. Ellis, A. E. Kelly, D. Nesset, D. Pitcher, D. G. Moodie, and R. Kashyap, "Error free 100 Gbit/s wavelength conversion using grating assisted cross-gain modulation in 2 mm long semiconductor amplifier," Electron. Lett. **34**(20), 1958-1959 (1998).

[98] Y. Liu, J. P. Turkiewicz, S. Zhang, E. Tangdiongga, E. J. M. Verdurmen, H. de Waardt, Z. Li, D. Lenstra, G. D. Khoe, and H. J. S. Dorren, "40 Gbit/s SOA-

based wavelength conversion assisted by a narrow optical bandpass filter," in *Proceedings Symposium IEEE/LEOS Benelux Chapter*, (IEEE, 2004), 251-254.

[99] Y. Liu, E. Tangdiongga, Z. Li, S. Zhang, H. de Waardt, G. D. Khoe, and H. J. S. Dorren, "80 Gbit/s wavelength conversion using semiconductor optical amplifier and optical bandpass filter," Electron. Lett. **41**(8), 487-489 (2005).

[100] L. Bramerie, A. Clarke, G. Girault, S. Lobo, M. Gay, C. Guignard, V. Roncin, B. Kennedy, P. Maguire, S. Feve, B. Clouet, F. Ginovart, L. P. Barry, J. C. Simon, and P. Anandarajah, "Investigation of SOA-based wavelength conversion at 80 Gb/s using bandpass filtering," in *Conference on Lasers and Electro-Optics / Quantum Electronics and Laser Science (CLEO/QELS)*, (Optical Society of America, 2006), CMT7.

[101] Y. Liu, E. Tangdiongga, Z. Li, Z. Shaoxian, W. Huug de, G. D. Khoe, and H. J. S. Dorren, "Error-free all-optical wavelength conversion at 160 Gb/s using a semiconductor optical amplifier and an optical bandpass filter," J. Lightwave Technol. **24**(1), 230-236 (2006).

[102] P. J. Winzer and R. J. Essiambre, "Advanced optical modulation formats," Proc. IEEE **94**(5), 952-985 (2006).

[103] Y. Yu, X. L. Zhang, and D. X. Huang, "All-optical format conversion from CS-RZ to NRZ at 40 Gbit/s," Opt. Express **15**(9), 5693-5698 (2007).

[104] J. Leuthold, C. H. Joyner, B. Mikkelsen, G. Raybon, J. L. Pleumeekers, B. I. Miller, K. Dreyer, and C. A. Burrus, "100 Gbit/s all-optical wavelength conversion with integrated SOA delayed-interference configuration," Electron. Lett. **36**(13), 1129-1130 (2000).

[105] G. Girault, A. M. Clarke, D. Reid, C. Guignard, L. Bramerie, P. Anandarajah, L. P. Barry, J. C. Simon, and J. Harvey, "Analysis of bit rate dependence up to 80 Gbit/s of a simple wavelength converter based on XPM in a SOA and a shifted filtering," Opt. Commun. **281**(23), 5731-5738 (2008).

[106] R. Trebino, Frequency-Resolved Optical Gating: The Measurement of Ultrashort Laser Pulses (Springer, 2000).

[107] P. Vorreau, A. Marculescu, J. Wang, G. Boettger, B. Sartorius, C. Bornholdt, J. Slovak, M. Schlak, C. Schmidt, S. Tsadka, W. Freude, and J. Leuthold, "Cascadability and regenerative properties of SOA all-optical DPSK wavelength converters," IEEE Photonics Technol. Lett. **18**(18), 1970-1972 (2006).

[108] Y. M. Liu, M. R. Lin, X. N. Pan, B. Z. Zhang, and W. J. Chen, "Systematic study of polarization of two-photon absorption in symmetry assignments," Acta Phys. Sin. (Overseas Edition) **3**(11), 801-808 (1994).

Conference contributions and publications

1. J. Leuthold, W. Freude, G. Boettger, J. Wang, P. Vorreau, and A. Marculescu, "Trends in the field of all-optical wavelength conversion and regeneration for communication up to 160 Gb/s," in *31st European Conference on Optical Communications (ECOC),* (IEEE, 2005), Tu3.3.6.
2. J. Leuthold, W. Freude, G. Boettger, P. Vorreau, A. Marculescu, and J. Wang, "Transparent networks and the role of SOA based all-optical wavelength converters and signal regenerators," in *SPIE Asia-Pacific Optical Communications (APOC)*, (SPIE, 2005), 6021-6095.
3. J. Leuthold, W. Freude, G. Boettger, J. Wang, P. Vorreau, and A. Marculescu, "Trends in the field of all-optical wavelength conversion and regeneration," in *Workshop on Optical Transmission and Equalization (WOTE)*, (Shanghai Jiao Tong University, 2005), C4.
4. J. Leuthold, W. Freude, G. Boettger, J. Wang, A. Marculescu, P. Vorreau, and R. Bonk, "All-optical regeneration," in *8th International Conference on Transparent Optical Networks (ICTON)*, (IEEE, 2006).
5. J. Leuthold, W. Freude, J. Wang, P. Vorreau, and A. Marculescu, "A novel all-optical DPSK wavelength converter based on Semiconductor Optical Amplifier (SOA) nonlinearities," in *Workshop der ITG Fachgruppe 5.3.1*, (ITG, 2006).
6. Vorreau, A. Marculescu, J. Wang, G. Boettger, B. Sartorius, C. Bornholdt, J. Slovak, M. Schlak, C. Schmidt, S. Tsadka, W. Freude, and J. Leuthold, "Cascadability and regenerative properties of SOA all-optical DPSK wavelength converters," IEEE Photonics Technol. Lett. **18**(18), 1970-1972 (2006).
7. J. Leuthold, W. Freude, P. Vorreau, A. Marculescu, J. Wang, and G. Boettger, "All-optical signal processing for phase-sensitive modulation formats," in *SPIE Asia-Pacific Optical Communications (APOC)*, (SPIE, 2006), 635311.
8. W. Freude, J. Leuthold, P. Vorreau, A. Marculescu, J. Wang, and G. Boettger, "All-optical processing of novel modulation formats using semiconductor optical amplifiers," in *Frontiers in Optics* (Optical Society of America, 2006), FTuV1.

9. B. Sartorius, C. Bornholdt, J. Slovak, M. Schlak, C. Schmidt, A. Marculescu, P. Vorreau, S. Tsadka, W. Freude, and J. Leuthold, "All-optical DPSK wavelength converter based on MZI with integrated SOAs and phase shifters," in *Optical Fiber Communication Conference*, OSA Technical Digest Series (Optical Society of America, 2006), OWS6.
10. J. Leuthold, J. Wang, T. Vallaitis, C. Koos, R. Bonk, A. Marculescu, P. Vorreau, S. Sygletos, and W. Freude, "New approaches to perform all-optical signal regeneration," in *9th International Conference on Transparent Optical Networks (ICTON),* (IEEE, 2007), We.D2.1.
11. A. Marculescu, J. Wang, J. Li, P. Vorreau, S. Zadok, S. Ben-Ezra, S. Tsadka, W. Freude, and J. Leuthold, "Pattern effect removal technique for semiconductor optical amplifier-based wavelength conversion," in *33th European Conference on Optical Communications (ECOC)*, (IEEE, 2007), Tu.3.4.6.
12. J. Wang, A. Marculescu, J. Li, P. Vorreau, S. Tzadok, S. Ben-Ezra, S. Tsadka, W. Freude, and J. Leuthold, "Pattern effect removal technique for semiconductor-optical-amplifier-based wavelength conversion," IEEE Photonics Technol. Lett. **19**(24), 1955-1957 (2007).
13. J. Wang, A. Marculescu, J. Li, Z. Zhang, W. Freude, and J. Leuthold, "All-optical vestigial-sideband signal generation and pattern effect mitigation with an SOA based red-shift optical filter wavelength converter," in *34th European Conference on Optical Communication (ECOC)*, (IEEE, 2008), We.2C6.
14. J. Li, J. Wang, A. Marculescu, P. Vorreau, Z. Zhang, W. Freude, and J. Leuthold, "All-optical SOA-based wavelength converter assisted by optical filters with wide operation wavelength and large dynamic input power range," in *SPIE Asia Pacific Optical Communications* (SPIE, 2008), 713525-713528.
15. A. Marculescu, S. Sygletos, J. Li, D. Karki, D. Hillerkuss, S. Ben-Ezra, S. Tsadka, W. Freude, and J. Leuthold, "RZ to CSRZ format and wavelength conversion with regenerative properties," in *Optical Fiber Communication Conference*, OSA Technical Digest Series (Optical Society of America, 2009), OThS1.

16. S. Sygletos, R. Bonk, T. Vallaitis, A. Marculescu, P. Vorreau, J. Li, R. Brenot, F. Lelarge, G.-H. Duan, and W. Freude, "Optimum filtering schemes for performing wavelength conversion with QD-SOA," in *11th International Conference on Transparent Optical Networks (ICTON),* (IEEE, 2009), Mo.C1.3.
17. R. Bonk, S. Sygletos, R. Brenot, T. Vallaitis, A. Marculescu, P. Vorreau, J. Li, W. Freude, F. Lelarge, G.-H. Duan, and J. Leuthold, "Optimum filter for wavelength conversion with QD-SOA," in *Conference on Lasers and Electro-Optics / Quantum Electronics and Laser Science (CLEO/QELS),* (Optical Society of America, 2009), CMC6.
18. J. Leuthold, W. Freude, S. Sygletos, R. Bonk, T. Vallaitis, and A. Marculescu, "All-optical regeneration," in Asia Communications and Photonics Conference (ACP), (2009), TuK1.
19. W. Freude, D. Hillerkuss, T. Schellinger, R. Schmogrow, M. Winter, T. Vallaitis, R. Bonk, A. Marculescu, J. Li, and M. Dreschmann, "Orthogonal frequency division multiplexing (OFDM) in photonic communications," in *10th International Conference on Fiber Optics & Photonics (Photonics'10)*, (IIT Guwahati, 2010).
20. D. Hillerkuss, M. Winter, M. Teschke, A. Marculescu, J. Li, G. Sigurdsson, K. Worms, S. Ben-Ezra, N. Narkiss, and W. Freude, "Simple all-optical FFT scheme enabling Tbit/s real-time signal processing," Opt. Express **18**(9), 9324-9340 (2010).
21. J. Leuthold, R. Bonk, T. Vallaitis, A. Marculescu, W. Freude, C. Meuer, D. Bimberg, R. Brenot, F. Lelarge, and G.-H. Duan, "Linear and nonlinear semiconductor optical amplifiers," in *Optical Fiber Communication Conference*, OSA Technical Digest Series (Optical Society of America, 2010), OThI3.
22. J. Li, K. Worms, A. Marculescu, D. Hillerkuss, S. Ben-Ezra, W. Freude, and J. Leuthold, "Optical vector signal analyzer based on differential detection with inphase and quadrature phase control," in *Signal Processing in Photonic Communications* (Optical Society of America 2010), SPTuB3.
23. D. Hillerkuss, M. Winter, M. Teschke, A. Marculescu, J. Li, G. Sigurdsson, K. Worms, W. Freude, and J. Leuthold, "Low-complexity optical FFT

scheme enabling Tbit/s all-optical OFDM communication," in *11th ITG Symposium on Photonic Networks*, (VDE, 2010).

24. J. Leuthold, M. Winter, W. Freude, C. Koos, D. Hillerkuss, T. Schellinger, R. Schmogrow, T. Vallaitis, R. Bonk, and A. Marculescu, "All-optical FTT signal processing of a 10.8 Tb/s single channel OFDM signal," in *Photonics in Switching,* OSA Technical Digest Series, (Optical Society of America 2010), PWC1.
25. A. Tervonen, M. Mattila, W. Weiershausen, T. von Lerber, E. Parsons, H. Chaouch, A. Marculescu, J. Leuthold, and F. Kueppers, "Dual output SOA based amplifier for PON extenders," in *36th European Conference on Optical Communication (ECOC),* (IEEE, 2010), P6.18.
26. D. Hillerkuss, A. Marculescu, J. Li, M. Teschke, G. Sigurdsson, K. Worms, S. Ben-Ezra, N. Narkiss, W. Freude, and J. Leuthold, "Novel optical fast Fourier transform scheme enabling real-time OFDM processing at 392 Gbit/s and beyond," in *Optical Fiber Communication Conference*, OSA Technical Digest Series (Optical Society of America, 2010), OWW3.
27. W. Freude, R. Bonk, T. Vallaitis, A. Marculescu, A. Kapoor, E. K. Sharma, C. Meuer, D. Bimberg, R. Brenot, and F. Lelarge, "Linear and nonlinear semiconductor optical amplifiers," in *12th International Conference on Transparent Optical Networks (ICTON),* (IEEE, 2010), We.D4.1.
28. W. Freude, D. Hillerkuss, T. Schellinger, R. Schmogrow, M. Winter, T. Vallaitis, R. Bonk, A. Marculescu, J. Li, and M. Dreschmann, "All-optical real-time OFDM transmitter and receiver," in *Conference on Lasers and Electro-Optics / Quantum Electronics and Laser Science (CLEO/QELS),* (Optical Society of America, 2011), CTh01.
29. D. Hillerkuss, T. Schellinger, R. Schmogrow, M. Winter, T. Vallaitis, R. Bonk, A. Marculescu, J. Li, M. Dreschmann, and J. Meyer, "Single source optical OFDM transmitter and optical FFT receiver demonstrated at line rates of 5.4 and 10.8 Tbit/s," in *Optical Fiber Communication Conference*, OSA Technical Digest Series (Optical Society of America, 2010), PDPC1.
30. S. Sygletos, R. Bonk, T. Vallaitis, A. Marculescu, P. Vorreau, J. Li, R. Brenot, F. Lelarge, G.-H. Duan, and W. Freude, "Filter assisted

wavelength conversion with quantum-dot SOAs," J. Lightwave Technol. **28**(6), 882-897 (2010).

31. Hillerkuss, R. Schmogrow, T. Schellinger, M. Jordan, M. Winter, G. Huber, T. Vallaitis, R. Bonk, P. Kleinow, F. Frey, M. Roeger, S. Koenig, A. Ludwig, A. Marculescu, J. Li, M. Hoh, M. Dreschmann, J. Meyer, S. Ben-Ezra, N. Narkiss, B. Nebendahl, F. Parmigiani, P. Petropoulos, B. Resan, A. Oehler, K. Weingarten, T. Ellermeyer, J. Lutz, M. Moeller, M. Huebner, J. Becker, C. Koos, W. Freude and J. Leuthold "26 Tbit s-1 line-rate super-channel transmission utilizing all-optical fast Fourier transform processing," Nature Photonics **5**, 364-371 (2011).
32. A. Marculescu, S. Ó'Duill, C. Koos, W. Freude and J. Leuthold, "Spectral signature of nonlinear effects in semiconductor optical amplifiers," Opt. Express **25**(24), 29526-29559 (2017).

Acknowledgements

At this point, I would like to acknowledge the valuable support provided by others in in the last years and during the preparation of this thesis. I would like to thank all those persons, who contributed directly or indirectly to the success of this work.

First, I want to thank my supervisors Prof. Jürg Leuthold and Prof. Wolfgang Freude for providing vision, guidance and funding for my work. I thank Prof. Leuthold for his inexhaustible stock of ideas und challenges, which always spurred my interest and effort. I thank Prof. Freude for the fruitful discussions on SOA nonlinearities and the publicated analytical model. I am grateful for his endless support for the publications and for this thesis.

I would like to thank Dr. Stelios Sygletos and Dr. Séan O'Dúill for their many suggestions and constant support also after leaving the KIT. I would also thank Jingshi Li, René Bonk, Jan Brosi, Dr. Christian Koos, Dr. Gunnar Böttger, Thomas Vallaitis and Philipp Vorreau for the good support during my time at the Institute for Photonics and Quantum Electronics (IPQ) of the Karlsruhe Institute of Technology.

Further, I would like to thank the personnel and technical staff at the IPQ, especially, Mrs. Lehmann and Mr. Bürger for a pleasant and effective working environment.

Last but not least, I want to thank my wife and my parents for their love and help, but also for their patience regarding the thesis. Their support made me believe in the success of this thesis.

ETH Zürich Series in Electromagnetic Fields, Vol. 7
Edited by Prof. J. Leuthold

ETH Zürich
Institute of Electromagnetic Fields (IEF)
Switzerland

Semiconductor optical amplifiers (SOAs) have found widespread use in optical communications covering the important telecommunications window with optical carrier wavelengths from 1.1 µm up to 1.6 µm. While amplifiers are usually operated in their linear region, the inherent nonlinearities of SOAs can be exploited for all-optical signal processing like signal regeneration, wavelength conversion, and modulation format conversion. For both, linear and nonlinear applications, the onset and the amount of the nonlinear response is important for choosing the proper operating point.

In this book a nonlinear SOA model is developed. Measuring the spectra resulting from a pump-probe experiment, the strength of the various nonlinear contributions can be assigned to inter- and intraband carrier dynamics in the semiconductor. The experiments reveal for the first time the importance and the role of two-photon induced free carrier absorption $\mathrm{FCA}_{\mathrm{TPA}}$ – an effect that so far was not properly taken care of. The resulting blue-shifted sideband makes it possible to design a patterning-free all-optical wavelength converter. More generally, this model helps in finding optimal optical filter schemes for wavelength converters, resulting in patterning-free output signals at high bit rates.

About the Author

Andrej Titus Marculescu was born 1978 in Bucharest, Romania. He received the diploma degree (Dipl.-Ing.) at the department of Electrical Engineering and Information Technology, University of Karlsruhe, in 2004. In 2018 he was awarded the Dr. sc. degree (Ph.D.) from ETH Zurich, Switzerland. His research interests include wavelength and modulation format conversion based on semiconductor optical amplifier nonlinearities.

ISBN: 978-3-906916-27-9

ISBN 978-3-906916-27-9
9 783906 916279 >